NON-CLASSICAL GROWTH MECHANISMS OF FUNCTIONAL INORGANIC CRYSTALS

Katherine Self

A Thesis Submitted for the Degree of PhD
at the
University of St Andrews

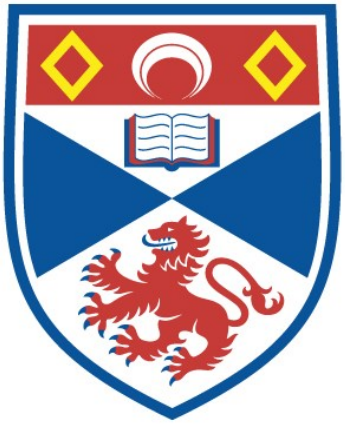

2016

Non-Classical Growth Mechanisms of Functional Inorganic Crystals

Katherine Self

University of St Andrews

This thesis is submitted in partial fulfilment for the degree of

PhD

at the

University of St Andrews

Declarations

I, Katherine Self, hereby certify that this thesis, which is approximately 41,000 words in length, has been written by me, and that it is the record of work carried out by me, or principally by myself in collaboration with others as acknowledged, and that it has not been submitted in any previous application for a higher degree.

I was admitted as a research student in September 2012 and as a candidate for the degree of PhD in July, 2013; the higher study for which this is a record was carried out in the University of St Andrews between 2012 and 2016.

Date: Signature of candidate:

I hereby certify that the candidate has fulfilled the conditions of the Resolution and Regulations appropriate for the degree of PhD in the University of St Andrews and that the candidate is qualified to submit this thesis in application for that degree.

Date: Signature of supervisor:

In submitting this thesis to the University of St Andrews I understand that I am giving permission for it to be made available for use in accordance with the regulations of the University Library for the time being in force, subject to any copyright vested in the work not being affected thereby. I also understand that the title and the abstract will be published, and that a copy of the work may be made and supplied to any bona fide library or research worker, that my thesis will be electronically accessible for personal or research use unless exempt by award of an embargo as requested below, and that the library has the right to migrate my thesis into new electronic forms as required to ensure continued access to the thesis. I have obtained any third-party copyright permissions that may be required in order to allow such access and migration, or have requested the appropriate embargo below.

The following is an agreed request by candidate and supervisor regarding the publication of this thesis:

Embargo on all of printed and electronic copy for a period of two years on the following ground(s): Publication would preclude future publication

Date: Signature of candidate:

Signature of supervisor:

Acknowledgements

There are many people I would like to thank for their help and support through the course of my PhD. First and foremost I would like to thank my supervisor, Professor Wuzong Zhou, whose knowledge and guidance have been invaluable throughout my research work. His support and encouragement have been particularly helpful during his insightful discussions and during the preparation of manuscripts for publication. I would also like to thank Professor Heyong He who was very supportive when acting as my supervisor during the year I spent working at Fudan University in Shanghai, China.

Secondly, my thanks and appreciation go to Dr Heather Greer, from the Zhou group, who has been a constant source of help and direction throughout both my MChem and PhD research. My thanks also go to Mr Chang-Yang Chiang for his help with studying the electronic configuration of crystal surfaces, and to the other members of the Zhou group as well as the many other members of the School of Chemistry who have been happy to assist me in any way. I would also like to add thanks to Dr Xueying Chen and to the PhD students at Fudan University who assisted me with using the facilities in the Department of Chemistry during my time there.

Further to this, I am very thankful to Mr Ross Blackley for his assistance and training on the use of the SEM and TEM microscopes, to Mr Derek Waddell and Dr Yuri Andreev for performing the PXRD experiments and to Mrs Sylvia Williamson for performing the TGA and gas adsorption experiments.

Importantly, I also wish to express my immense gratitude to my parents and sisters who have been an essential and unfailing source of support and understanding during the course of my PhD research. To my friends, as well, I owe a great deal of thanks for providing support and encouragement during the difficult periods and for celebrating with me even the smallest of accomplishments.

Finally, I would like to thank the University of St Andrews for the studentship and the British Council for the financial support, which gave me the great opportunity to spend a year of my PhD in Shanghai.

Abstract

This project relates to the non-classical growth of inorganic crystals with interesting morphologies that are highly desirable in industry. All crystals were synthesized via hydrothermal or solvothermal methods and their growth was studied by stopping each reaction at a range of different times, extracting the particles and analysing them using a variety of characterisation techniques. The main techniques used were scanning electron microscopy and transmission electron microscopy but other techniques, such as powder X-ray diffraction and thermal gravimetric analysis, were also employed.

Decorated ZnO microstadiums were studied where ZnO nanocones coat the inner and outer columnar walls of ZnO microstadiums. It was revealed that the polymer in the synthetic solution enhanced the aggregation of nanocrystallites of precursor ions on the microstadium surfaces, which then underwent recrystallization, forming ZnO nanocones. The presence of organic agents was also found to be crucial in the non-classical growth mechanisms of $CaCO_3$ and RHO-ZIF crystals as the presence of charged groups on the organic molecules led to the aggregation of precursor molecules/ions, preventing classical growth. The disordered aggregates underwent surface recrystallization, forming 'core-shell' structures where a thin layer of single crystal encased a disordered core. Over time the crystallisation extended from the surface inwards, towards the core, until true single crystals were formed.

Organic molecules were also shown to play a role in the non-classical growth of 8-branched Cu_2O structures. In this case, however, studies of the electronic configuration of the main terminating facets of Cu_2O crystals revealed another key factor in their non-classical growth. Terminating hydroxyl groups on the Cu_2O surfaces could have different charges depending on the number of Cu^+ ions they were coordinated to. The terminating {111} faces were the only ones to be coated with negatively charged hydroxyl groups, which explained the rapid growth on these surfaces as they were able to attract the positively charged metal/polymer precursor clusters. This new phenomenon was also found to be the main driving force in the rapid growth of branches in snowflake-like Fe_2O_3 crystals despite no organic agent being used. In this case, the $\{11\bar{2}0\}$ faces of the seed crystals had positively charged hydroxyl groups that were able to rapidly attract the negatively charged $[Fe(CN)_6]^{3-}$ ions in the aqueous solution.

Publications

1. K. Self, H. Zhou, H. F. Greer, Z. R. Tian, W. Z. Zhou,
   Reversed crystal growth of ZnO microdisks,
   Chem. Commun., 2013, 49, 5411. DOI: 10.1039/c3cc41208c.
   Information presented in this thesis has been published and has been adapted with permission from the above authors. Copyright 2013, Royal Society of Chemistry.

2. A. W. Ritchie, M. I. T. Watson, R. Turnbull, Z. Z. Lu, M. Telfer, J. E. Gano, K. Self, H. F. Greer, W. Z. Zhou,
   Reversed crystal growth of rhombohedral calcite in the presence of chitosan and gum arabic,
   CrystEngComm, 2013, 15, 10266. DOI: 10.1039/c3ce41543k.
   Information presented in this thesis has been published and has been adapted with permission from the above authors. Copyright 2013, Royal Society of Chemistry.

3. K. Self, M. Telfer, H. F. Greer, W. Z. Zhou,
   Reversed crystal growth of RHO Zeolitic Imidazolate Framework (ZIF),
   Chem. Eur. J., 2015, 21, 19090. DOI: 10.1002/chem.201503437.
   Information presented in this thesis has been published and has been adapted with permission from the above authors. Copyright 2015, Wiley.

Contents

Chapter 1. Introduction

The ability to finely control the shapes and structures of crystals grown via facile hydrothermal and solvothermal routes is of great practical importance for many materials which are highly desired for industrial applications. In this way, it is essential to develop an understanding of the crystal growth mechanisms by which these materials have formed as only by truly understanding how they grow can we manipulate their morphology and, therefore, exhibit control over their properties for their various applications (1).

It is often reported that knowledge of the fundamentals of crystal growth has arisen from the morphological studies of naturally occurring crystals (2), which, in turn, slowly led to the understanding of the classical crystal growth mechanisms that will be explained in detail through this chapter. As a result, materials are often assumed to follow these classical routes but in recent years it has become more and more apparent that the classical theories are often insufficient to explain crystal growth in a huge variety of systems.

Xia *et al.* have described this situation very appropriately, stating that "at the current stage of development, it is not an exaggeration to say that the chemical synthesis of metal nanocrystals (as well as for other solid materials) remains an art rather than a science" (3).

1.1 Classical Crystal Growth

1.1.1 Classical Nucleation Theory

The first step in classical crystal growth theory is nucleation, i.e. the formation of a cluster or "seed" crystal from which further growth can occur. Nucleation can be described as a thermodynamic model that expresses the appearance of a new phase (the nucleus, sometimes referred to as the β-phase) within the metastable primary phase (or α-phase) (4). The classical nucleation theory, CNT, which was developed by Becker and Döring in the 1930s (5), is still generally seen as the basic model for this first step towards crystal growth. This theory was then extended to the synthesis of nanoparticles in the 1950s as described by LaMer *et al.* (6) who based their research on sulphur hydrosols and a range of oil aerosols.

CNT is founded on the macroscopic Gibbs-Thomson or capillary effect, i.e. the curvature driven increase in the interfacial free energy between particles of a particular "β phase" forming in a matrix of an existing, different, "α phase" and, therefore, an increase in the overall free energy of the system (7). This means that macroscopic properties (for example, surface energy) have to be taken into account when developing thermodynamic equations for the rate of nucleation (5). For this reason, nucleation expressions have to distinguish between heterogeneous and homogeneous systems. Heterogeneous nucleation is that which occurs at preferential sites (such as impurities or phase boundaries) on solid surfaces in contact with a liquid or gaseous phase.

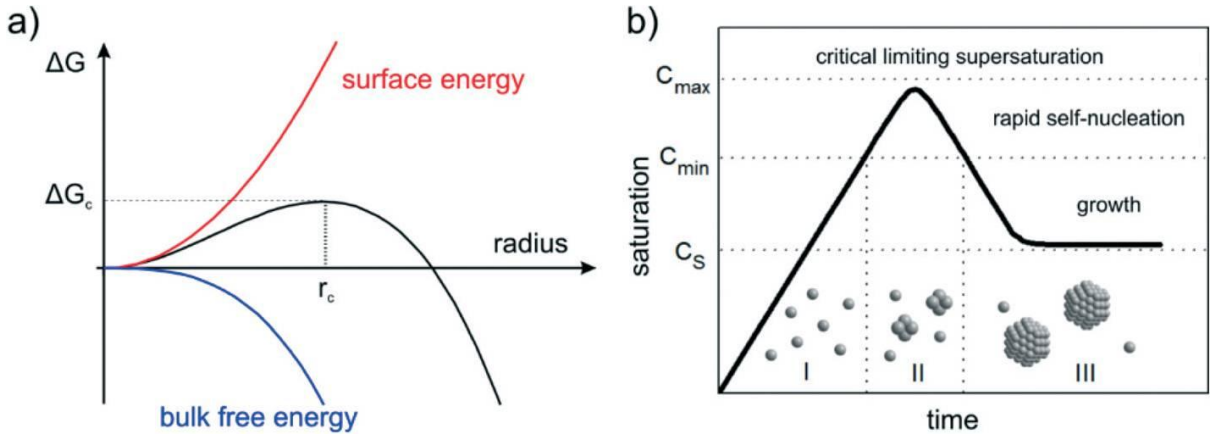

Figure 1.1. a) Plot of the Gibbs free energy, ΔG, of a cluster (nucleus) as a function of cluster radius, demonstrating the fundamental principle of CNT. ΔG_c is the activation energy at the critical cluster radius, r_c. b) Plot of saturation (concentration of building units) over time, illustrating the generation of building units (I), nucleation (II) and subsequent crystal growth (III). Reproduced from Ref. 4 with permission from The Royal Society of Chemistry.

Homogeneous nucleation, in contrast, occurs spontaneously and arbitrarily, and can be used to describe nucleation within a solution but requires a supercritical state such as supersaturation. This is illustrated in Figure 1.1b, where the saturation (the concentration of building units in the solution) is shown as a function of time across a process of the generation of building units (I), followed by self-nucleation (II) and subsequent crystal growth (III). In a typical homogeneous system, precursor materials are first heated, which causes them to decompose. This process can be described as the generation of building units, which can be atoms, molecules or ions. The concentration (saturation) of these units increases

steadily with time until a point of supersaturation, C_{max}, is reached at which the units start to aggregate into small clusters (nuclei) followed by further rapid growth.

As more precursor units aggregate into the clusters, the concentration of free units in the solution steadily decreases. If the concentration drops rapidly to a value below the minimum supersaturation, $C_{min,}$ level then any further nucleation is prevented. If, however, the supply of precursor building units is continuous, the nuclei can continue to grow into larger and larger nanocrystals until an equilibrium state is reached between the building units free in the solution and those on the surfaces of the nanocrystals.

In the present work, crystal growth is studied through hydrothermal or solvothermal methods and so it is the homogenous form of nucleation theory that will be the most relevant. Several sources have been drawn upon to derive a thermodynamic expression for nucleation in a homogenous system according to CNT (4, 5, 8).

First, an expression for the Gibbs free energy of a nucleus is needed, which can generally be expressed as the sum of two terms, one negative and one positive. The negative term signifies the energy of the bonding between two monomers, which is favourable since it leads to a lowering of the bulk energy. The positive term, on the other hand, signifies the unfavourable side of such bonding due to the resultant increase in the free surface energy. Combining these terms gives an expression for the free energy of a cluster (ΔG) as shown in Equation 1.1, under the assumption that the cluster is spherical. The combination of these negative and positive terms results in a plot of ΔG that has a maximum at a critical radius, r_c, as shown in Figure 1.1a.

$$\Delta G = -\frac{4}{3}\pi r^3 |\Delta G_v| + 4\pi r^2 \gamma \qquad (1.1)$$

In this equation, r is the radius, $|\Delta G_v|$ represents the difference in bulk free energy per unit volume and γ is the surface free energy per unit area.

As shown in Figure 1.1a, since the corresponding energy to the critical radius, r_c, is the activation energy, ΔG_c, for nucleation, growth is only favoured for clusters with a radius greater than or equal to r_c. Clusters with a radius smaller than r_c would most likely be simply

dissolved back into the solution to reduce the overall free energy. The critical radius can be determined by solving Equation 1.1 for $\frac{d(\Delta G)}{dr} = 0$, resulting in Equation 1.2 (4).

$$r_c = \frac{2\gamma}{|\Delta G_v|} \tag{1.2}$$

By simply replacing *r* in Equation 1.1 with r_c from Equation 1.2, an expression for the critical free energy, ΔG_c, of a cluster can be determined:

$$\Delta G_c = \frac{16\pi\gamma^3}{|\Delta G_v|^2} - \frac{32\pi\gamma^3}{3|\Delta G_v|^3} \tag{1.3}$$

Finally, the rate of nucleation, B, in a homogeneous system can be expressed using the Arrhenius equation, as shown in Equation 1.4, where k_B is the nucleation constant and T is the temperature.

$$B = Aexp\left(\frac{-\Delta G_c}{k_B T}\right) \tag{1.4}$$

While this theory is still generally accepted to describe the initial steps of crystal growth, there have been several studies that have shown CNT can often fail to fully explain nanoparticle growth (9).

1.1.2 Classical Crystal Growth Theory

The classical, or so-called 'bottom-up', crystal growth mechanism is a very well-established crystal growth route that was first reported more than a century ago. This crystal

growth route is described by the Bravais-Friedel-Donnay-Harker (BFDH) law (10) and Hartman-Perdok theory (11) and describes how highly symmetric polyhedra can be formed from free crystals. In this mechanism, crystal growth begins with a single nucleation from which layer by layer deposition of atoms occurs. According to this mechanism, the crystal must be single crystalline at all growth stages with the crystal size increasing over time.

It has been well established that the crystal growth rate, R_{hkl}, is different along each of the different faces of a crystal and that R_{hkl} is inversely proportional to the inter-planar distance, d_{hkl}, of each given crystal face (12). Therefore, a large d-spacing along a particular crystallographic orientation would be associated with a low surface energy of the relevant {hkl} planes and, consequently, growth along this direction would be slow. Due to this relationship between R_{hkl} and d_{hkl}, the final morphology of the crystal forms with faces corresponding to those with the largest inter-planar distance (i.e. slowest growth rate) as the faces with the faster growth rates will be the first to 'grow out'. Figure 1.2 illustrates this.

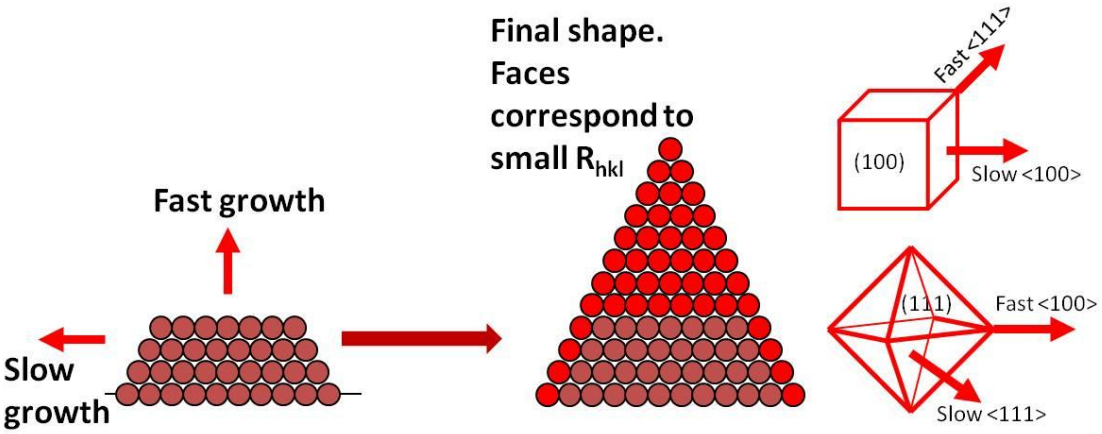

Figure 1.2. Illustration of the classical crystal growth theory whereby highly symmetric polyhedra form from a single nucleus as a result of the different growth rates (R_{hkl}) of different crystal faces. For example, a cubic morphology with six equivalent {100} faces will form when growth is slow along the <100> directions but fast along the <111>. Conversely, when growth is rapid along the <100> but slow along the <111> axes, an octahedral morphology will form with eight equivalent {111} faces.

Ostwald ripening is another phenomenon, originally reported in 1896, included in classical crystal growth theory (13). This thermodynamically driven approach explains that the average crystal size in an inhomogeneous system should increase over time since larger

crystals are more energetically favourable than smaller ones. This is a result of the fact that atoms on a crystal surface are less energetically stable than those in the interior and so larger crystals (with a smaller surface area to volume ratio) minimise the surface energy. This means that, although the formation of smaller crystals is kinetically favoured (i.e. it is easier to nucleate many small crystals rather than fewer large ones), over time the smaller particles in a system should dissolve and be deposited onto the surface of larger ones to achieve a more thermodynamically stable state as illustrated in Figure 1.3.

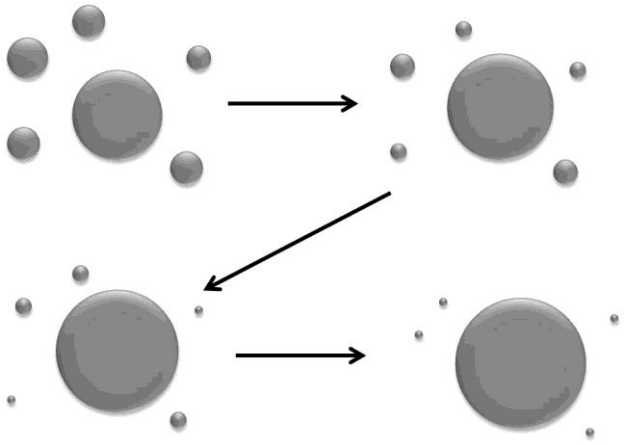

Figure 1.3. An illustration of the Ostwald ripening process in which smaller particles shrink and larger particles grow larger in order to reduce the overall surface area to volume ratio of the system.

Another well established crystal growth theory that takes thermodynamic factors into account (rather than the kinetic factors accounted for in the BFDH law and Hartman-Perdok theory) was first reported by Curie and Wulff, also over a century ago (14). In their approach, the equilibrium shape of a free crystal is said to be the shape which minimizes its surface free energy, regardless of the growth rates of the different faces.

1.2 Non-Classical Crystal Growth

In recent years, the need for a deeper understanding of the route by which crystals grow has become increasingly apparent as many investigations have shown that the classical crystal growth mechanisms described above are often not applicable.

Some crystals that appear to go against the classical growth theories are those with highly faceted appearances that exhibit properties attributed to single crystalline materials but that are in fact composed of many highly oriented nanoparticles. Between 1998 and 2000, Penn and Banfield and their co-workers published a series of studies proposing a so-called "irreversible oriented attachment" mechanism for the formation of mono-crystalline particles composed of many highly oriented primary nanocrystallites (15). They explain that the driving force for such a mechanism is that the surface free energy would be minimised by eliminating the faces with higher energies (16). Magnetic (17) and electric (18) fields have also been reported to be the driving force behind such orientation of nanocrystallites.

Kniep *et al.* (19) use a "dipole field directed" mechanism to describe the high levels of branching of single crystal fibrils in a hexagonal prism fluorapatite-gelatin seed through the unusual evolution of crystals with dumbbell shaped morphologies towards eventual spherulite-type morphologies. The dipole field was explained to have originated from the gelatin molecules, which transitioned from a triple helix arrangement to lining up parallel to each other (20). These mechanisms are still highly debated, however, since there are more recent reports of such a high orientation of nanocrystallites in systems where no organic, polymer or other surfactant was added into the synthesis, demonstrating that such structure directing agents are not always necessary for oriented attachment to take place (21).

As another example of problems left unaddressed in the classical growth theories, it is also clear that crystal structures with highly branched or dendritic morphologies must form via alternative growth mechanisms as their massive surface areas do not follow the thermodynamic drive to minimize the surface energy. For systems with complex synthetic conditions, researchers have been able to tailor the formation of various arrays of nano- or microcrystals through a range of complex methods such as laser assisted oxidation (22) or using template techniques (23).

However, the ability to control the shape and size of crystals that grow freely in solution using simple hydrothermal or solvothermal techniques is something that is still relatively poorly understood and which is attracting a great deal of attention in recent years as these facile, low cost methods to produce finely tuned crystals could be very beneficial for their various industrial applications.

1.2.1 Reversed Crystal Growth

One non-classical growth mechanism of particular interest is the 'reversed crystal growth' route that was first reported by Zhou and co-workers as a result of work performed on the zeolite analcime at the University of St Andrews and Fudan University, published in 2007 (24).

This zeolite has a cubic unit cell and naturally conforms to a symmetric, polyhedral morphology with 24 dominating trapezohedral {211} faces (25) as can be seen in Figure 1.4a and 1.4b. Through the addition of ethylamine as a structure directing agent into the typical synthetic conditions, Zhou *et al.* were able to synthesise analcime crystals with a perfect icositetrahedron morphology and smooth crystal faces over 8 days, each with a diameter of approximately 50 μm (Figure 1.4a). As a result of this regular, smooth outer morphology, these analcime crystals had been believed for many years to be completely single crystalline since their shape can be very well explained by BFDH law, i.e. if the {211} crystal faces simply had the slowest growth rate under these conditions then the final shape would indeed be expected to be an icositetahedron with 24 {211} faces. It had also been assumed, therefore, that these analcime crystals grew following the classical growth mechanism.

When the researchers investigated this structure, however, and produced a single crystal XRD pattern of the crystals grown over 8 days, they observed a series of polycrystalline diffraction rings that overlapped with the expected single crystal diffraction spots (Figure 1.4c). If the analcime crystals had been true single crystals, the polycrystalline rings would not have been produced and so to investigate the origin of these rings the crystals were crushed open and analysed via SEM (Figure 1.4d). The images produced showed very clearly that the analcime particles were not single crystals at all but actually consisted of an interesting microstructure in which a very thin layer of single crystal encased a disordered, polycrystalline core, i.e. a "core-shell" structure was uncovered. The core was determined to be composed of many randomly oriented nanorods.

After this discovery, Zhou *et al.* continued to investigate the growth of the analcime crystals over a range of hydrothermal treatment times to determine exactly how this interesting morphology had developed. The large particle size and slow growth rate of these crystals made them an ideal system to enable the researchers to stop the growth process at

various reaction times, extract the crystals and perform detailed studies of them using SEM and TEM as the main characterisation techniques.

It was discovered that the earliest detectable morphology (after 16 h of reaction time) was polygonal shaped nanoplatelets, observed via TEM analysis to have an average diameter of around 20 nm. As the growth time was increased, rather than the nanoplatelets growing via layer by layer atomic deposition (i.e. following classical theory), they underwent oriented aggregation into discus shaped clusters. Suppression of the growth of the nanoplatelets along the <111> directions was explained to be due to the adsorption of ethylene molecules on the principal {111} analcime facets.

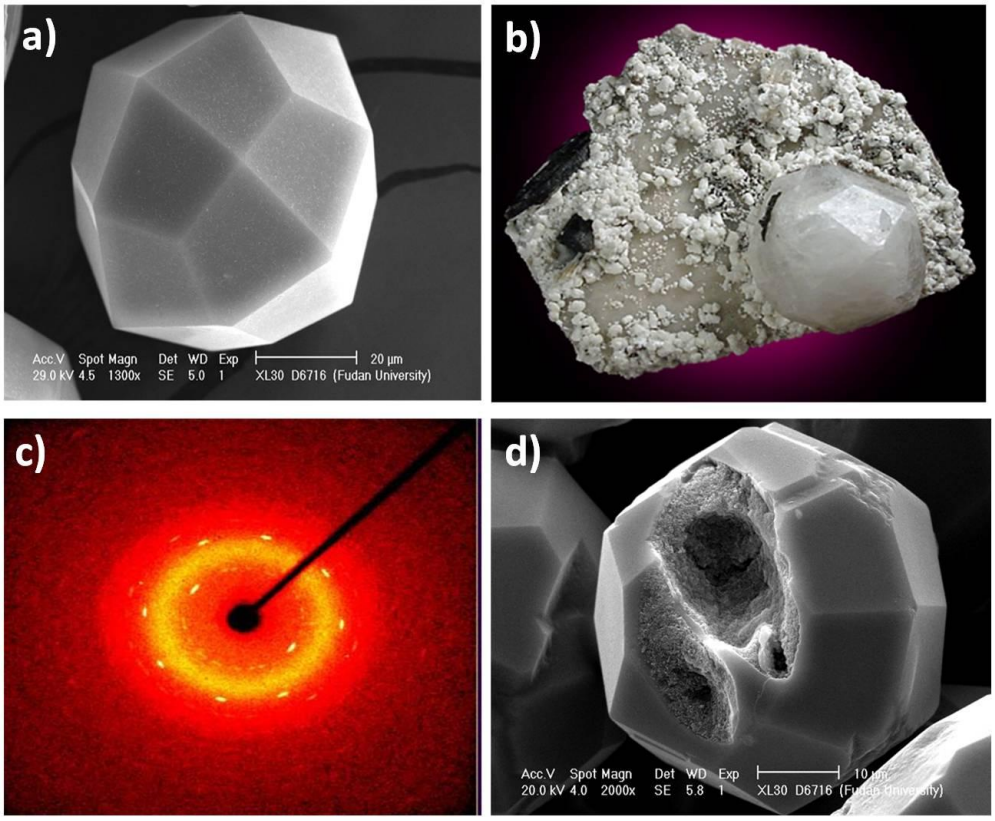

Figure 1.4. The discovery of the 'core-shell' structure of the zeolite analcime. a) A typical SEM image of an analcime crystal grown synthetically with a reaction time of 8 days. b) A photograph of how an analcime crystal appears naturally. c) Single crystal x-ray diffraction pattern of the synthetic 8 day sample where polycrystalline rings can be observed overlapping with the expected single crystal spots. d) A typical SEM image of an analcime particle grown over 3 days which has been crushed open, revealing the true core-shell structure where a thin crystalline shell encases a disordered core. Adapted from Ref. 24 with permission from The American Chemical Society.

At a slightly longer growth time of 20 h, SEM analysis revealed that further aggregation had occurred resulting in large, polycrystalline microspheres which had tiny, nano-sized “islands” of single crystal on their outer surfaces. After 3 days, these islands had grown larger and joined together, encasing the entire microsphere in a very thin (approximately 200 nm thick) layer of single crystal. A typical SEM image taken from an analcime particle grown over 3 days that had been crushed open is exhibited in Figure 1.4d, clearly displaying the true, core shell nature of the particles. Despite the core of the particle remaining disordered, the outer appearance was now that of a perfect icositetrahedron with 24 identical {211} facets. These facets became much smoother as the growth time was extended to the original 8 day synthesis as further surface recrystallization took place.

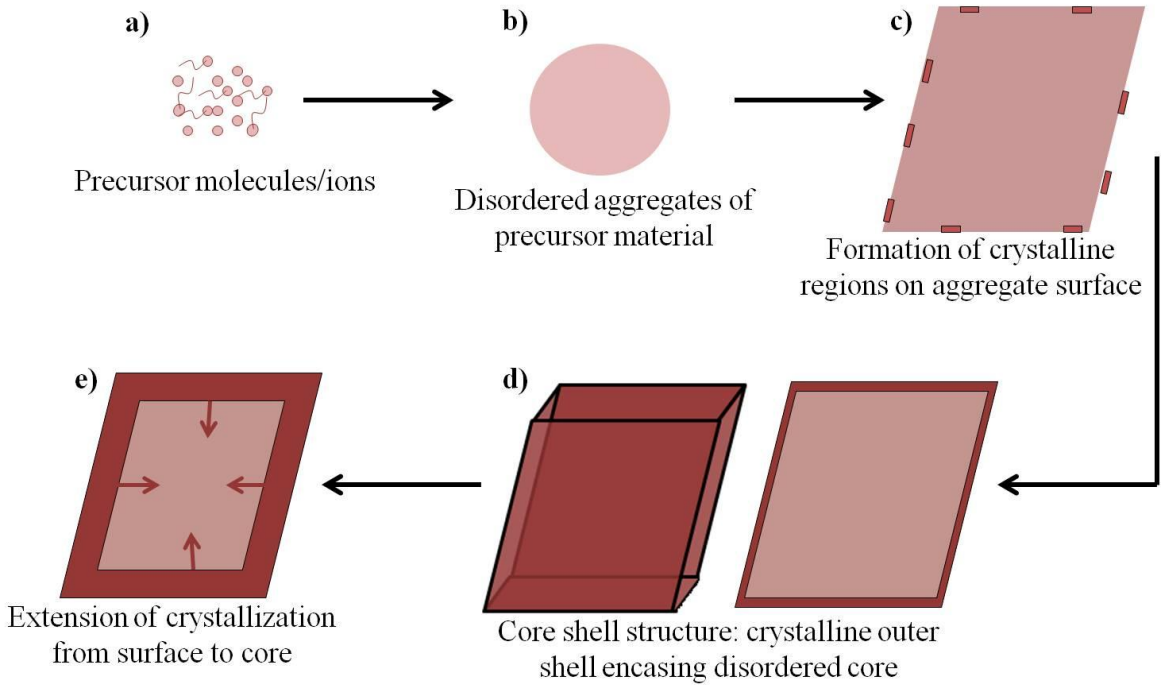

Figure 1.5. Schematic displaying the reversed crystal growth route which involves a process of a) formation of nanocrystallites from precursor molecules and ions, b) aggregation of these precursor nanocrystallites into disordered, typically spherical, particles. c) Recrystallization then begins to occur on the aggregate surfaces, first in small islands that grow larger and join together resulting in d) the core shell structure where a thin layer of single crystal encases the disordered core. e) Over time the crystallization extends from the surface towards the core and so the crystalline shell grows thicker and thicker until, eventually, true single crystals are formed.

After discovering the true growth route of the analcime particles to this point, even longer growth times were tested of up to 22 days and it is interesting to note that the icositetrahedral particles did not grow any larger over this time, i.e. they remained around 50 μm in diameter. However, when the particles were crushed open and viewed via SEM, a distinct increase in the thickness of the crystalline shell could be observed from around 200 nm at 3 days to approximately 600 nm at 8 days and so it was apparent that the shell was actually growing inwards rather than outwards as classical growth would have predicted. In fact, at the longest growth time of 22 days, the randomly oriented nanorods that had been encased by the crystalline shell had been consumed entirely via Ostwald ripening, leaving hollow analcime particles that were fully single crystalline.

This process of aggregation followed by surface re-crystallization and an extension of the crystallization from the surface inwards towards the core is now known as the 'reversed crystal growth' mechanism or the NARS route (which stands for Nanoparticles – Aggregation – surface Recrystallization – Single crystals). This process is illustrated in the schematic in Figure 1.5.

Since this pioneering work, reversed crystal growth has been found to be the true growth route for many polyhedral particles that had previously been assumed to be single crystals grown via the classical route. Examples include other zeolites (26) and mesoporous silicates (27) amongst many others (28). An example of the reversed crystal growth route in a metal oxide system for the formation of hexagonal zinc oxide microdisks (29) will be discussed in more detail in the introduction of Chapter 3 and another example of this mechanism for the formation of cubic crystals of a metal organic framework, MOF-5 (30), will be discussed in Chapter 5.

1.2.2 Crystal Growth Driven by Surface Adsorption

Even more recently, work from the University of St Andrews and the Chinese Academy of Sciences that was published in 2015 has shown evidence of another new form of non-classical crystal growth that follows a different route to that of the reversed crystal growth theory (31). The researchers studied the growth of highly dendritic, snowflake-like hematite, α-Fe_2O_3, crystals with six-fold symmetry and observed rapid growth of branches along the $<11\bar{2}0>$ zone axes. Through examining the electronic structure of the principal

terminating facets of α-Fe_2O_3, it was demonstrated that hydroxyl, OH, groups coating the terminal metal oxide surfaces would have different charges depending on how many metal cations the OH group was coordinated to. The overall charge of the terminating facet was, therefore, dependent on the charges of these hydroxyl groups. The researchers demonstrate that the $\{11\bar{2}0\}$ surfaces were unique in that they were the only terminating facets to be coated with positively charged hydroxyl groups that could attract the negatively charged principal precursor ions, $[Fe(CN)_6]^{3-}$, causing the rapid growth to occur solely along the $<11\bar{2}0>$ zone axes.

This new theory of crystal growth enhanced by surface adsorption will be discussed in detail in Chapter 4, where evidence of a similar mechanism occurring in the rapid branch growth along the <111> zone axes of 8-branched Cu_2O structures is presented, and also towards the end of Chapter 5, where further work on the snowflake-like hematite crystals is presented and discussed to complement and further verify the previous publication.

1.3 SEM and TEM Investigations of Crystal Growth

The major characterisation techniques used in this project are scanning electron microscopy (SEM) and transmission electron microscopy (TEM) as they provide a few key advantages over other analytical methods when attempting to elucidate the true nature of how a crystal forms.

The foremost advantage of electron microscopy is that it provides the opportunity to directly observe the crystal morphology which is, of course, particularly important for demonstrating the existence of a non-classical growth mechanism (32). SEM, in particular, is very useful for obtaining images that clearly show features such as a core-shell structure or a change in morphology from a misshapen aggregate to a perfect polyhedral crystal. TEM can also be used to this end but as samples for TEM analysis must be “electron transparent”, i.e. less than approximately 200 nm thick, they often need to be crushed before being placed on the sample grid and so the complete morphology can be lost. However, TEM has the advantage over SEM when it comes to observing the crystallinity of a sample. This is again very important in the study of crystal growth mechanisms over time as high resolution TEM (HRTEM) images can be used in conjunction with selected area electron diffraction (SAED) patterns to show transitions from areas of amorphous or polycrystalline material to single

crystal regions, or to observe any changes in the size and alignment of nanocrystallites within a disordered matrix.

Both SEM and TEM are also commonly used to provide information on the average particle size of a powdered sample as the particles observed through these techniques can be measured directly (in real space). The major disadvantage of using SEM and TEM for this purpose, however, is that the number of particles that can be analysed at a time is always limited and so a very large number of particles (more than 300, for example) must be studied before an "average" particle size can be determined for the whole sample. This inherent disadvantage of electron microscopy is also true when studying the crystal morphology, i.e. many images must be recorded to ensure that the morphology observed is truly typical for the sample. Other methods also exist for determining the average particle size of nanoparticles that analyse the bulk sample rather than only looking at individual particles. For example, the average crystallite size can be calculated from powder X-ray diffraction, PXRD, peaks of a sample by using the Scherrer equation (33), which is discussed in more detail in Chapter 2. These methods are typically used in conjunction with TEM or SEM to ensure the most accurate result possible as the crystallite size obtained via bulk analysis can often be confused by nanoparticles that exhibit unusual morphologies. For example, if the crystals display a morphology that is elongated in one dimension (nanorods, nanobelts, nanowires etc), the value calculated from PXRD will typically provide a good estimate for their thickness but not for their length (34). Additionally, since the synthetic methods for generating nanoparticles are only getting more sophisticated and more accurate over time, leading to nanoparticles that can be as small as a few atoms in diameter, the necessity for obtaining accurate particle size information becomes more and more apparent (35) and so TEM remains a key technique to employ as it is one of the very few existing methods that can provide real space visualisation of nanoparticles.

Another aspect of crystal growth that is best analysed using electron microscopy is the study of crystal facets and growth direction. SEM again gives the clearest evidence of the outer morphology of the crystals and so can be used to identify the major facets of a polyhedral crystal (particularly for crystals with a simple, such as a cubic, morphology where the facets are easily identifiable). TEM images and SAED patterns must be used alongside SEM images when the structure is more complicated, or when the particles are too small to be easily observed via SEM. HRTEM images can directly display crystal lattice fringes, which can then be measured to obtain d-spacings. The d-spacings are compared to known

values for the sample material to identify which facet is being imaged. If the sample is particularly beam sensitive, however, obtaining HRTEM images can be very difficult as the high energy electron beam can rapidly destroy the crystal structure. This is often the case for materials with a high amount of organic material embedded in the crystal structure, for example in MOFs or zeolites (36). In these instances, SEM analysis is more heavily relied upon to elucidate the crystal structure and morphology.

1.4 Aims and Objectives

The principal aims of this work are to study the non-classical crystal growth of a range of different materials using many analytical techniques such as TEM, HRTEM, SEM and PXRD amongst others. Through these studies, the overall aim is to establish how and why these materials form their unique and interesting structures and to use the evidence gathered to propose new, non-classical growth mechanisms to better explain their growth.

A further aim in doing this work is to demonstrate the importance of truly understanding the non-classical growth of functional materials as only by having a thorough understanding of their formation can we then tailor their morphologies and enhance their properties for their various applications. The objectives are as follows:

1. To investigate the formation mechanism of ZnO decorated microstadiums prepared via a three-step hydrothermal method where hexagonal ZnO disks are synthesized followed by a selective dissolution of their core resulting in ZnO microstadiums. The microstadiums are then treated with 1,3-propandiamine and zinc nitrate hexahydrate, leading to the growth of ZnO nanocones on the columnar surfaces of the microstadiums. To elucidate the mechanism by which these nanocones have grown.

2. To investigate the origin of a hydrothermally prepared 8-branched Cu_2O structure that undergoes a transition to a cubic morphology before finally undergoing a phase transition to form Cu metal nanoparticles with no uniform morphology that are coated in a layer of graphite or graphite oxide. A particular aim is to study the electronic surface structure of the main Cu_2O facets and determine the role they play in the rapid branch growth along the <111> zone axes.

3. To determine the role of organic chitosan molecules in the morphology evolution of rhombohedral calcite, $CaCO_3$, crystals. To propose a new, non-classical formation mechanism for the $CaCO_3$ particles based on a step-by-step investigation of their crystal growth over time.

4. To study the crystal growth of the zeolitic imidazolate framework, RHO-ZIF, particles that exhibit rhombic dodecahedral morphology and that had previously been assumed by researchers to be single crystalline. To demonstrate the benefits of fully understanding the growth mechanism of such a complex material, with many potential industrial applications, by examining its surface area and N_2 uptake over time.

5. To investigate the growth of highly dendritic hematite, α-Fe_2O_3, "snowflakes" with six-fold symmetry. To propose a mechanism for the rapid growth of the α-Fe_2O_3 branches in such a simple hydrothermal system despite no organic agents having been added into the synthetic solution.

References

1. Burda, C.; Chen, X.; Narayanan, R.; El-Sayed, M. A. *Chem. Rev.*, **2005**, *105*, 1025.
2. (a) Byrappa, K.; Ohachi, T. *Crystal growth technology*. William Andrew Publishing, New York, **2002**. (b) Sunagawa, I. *Crystals: growth, morphology and perfection*, Cambridge University Press, Cambridge, **2005**. (c) Mann, S.; Ozin, G. A. *Nature*, **1996**, *382*, 313. (d) Cölfen, H.; Antonietti, M. *Angew. Chem. Int. Ed.*, **2005**, *44*, 5576. (e) Tian, Z. R.; Liu, J.; Voigt, J. A.; Mckenzie, B.; Xu, H. *Angew. Chem. Int. Ed.*, **2003**, *42*, 414.
3. Xia, Y.; Xiong, Y.; Lim, B.; Skrabalak, S. E. *Angew. Chem. Int. Ed.*, **2008**, *48*, 60.
4. Polte, J. *Cryst. Eng. Comm.*, **2015**, *17*, 6809.
5. Becker, R.; Döring, W. *Ann. Phys.*, **1935**, *24*, 719.
6. (a) LaMer, V. K. *Ind. Eng. Chem.*, **1952**, *44*, 1270. (b) LaMer, V. K.; Dinegar, R. H. *J. Am. Chem. Soc.*, **1950**, *72*, 4847.
7. (a) Thomson, J. J. *Application of Dynamics to Physics and Chemistry*, Macmillan Co., New York, **1888**. (b) Jirgensons, B.; Straumanis, M. E. *A Short Textbook of Colloid Chemistry, Second Edition*, Elsevier, **2013**.
8. Pamplin, B. R. *Crystal Growth Second Edition*, Pergamon Press Ltd., Oxford, **1980**.

9. Finney, E. E.; Finke, R. G. *J. Colloid Interface Sci.*, **2008**, *317*, 351.
10. (a) Bravais, A. *Études Crystallographiques. Paris: Gauthier-Villars*, **1866**. (b) Friedel, M. G. *Bull. Soc. Fr. Mineral Cristallogr.*, **1907**, *30*, 326. (c) Donnay, J. D. H.; Harker, D. *Am. Mineral*, **1937**, *22*, 446.
11. Hartman, P.; Perdok, W. G. *Acta Cryst*., **1955**, *8*, 521.
12. Docherty, R.; Clydesdale, G.; Roberts, K. J.; Bennema, P. *J. Phys. D. Appl. Phys.*, **1991**, *24*, 89.
13. (a) Ostwald, W. *Lehrbruck der Allgemeinen Chemie*, **1896**, 2. (b) Boistelle, R.; Astier, J. P. *J. Cryst. Growth*, **1988**, *90*, 14.
14. (a) Curie, P. *Bull. Soc. Fr. Mineral Cristallogr.*, **1907**, *30*, 326. (b) Wulff, G. *Z. Kristallogr. Mineral*, **1885**, *8*, 145.
15. (a) Penn, R. L.; Banfield, J. F. *Am. Mineral*, **1998**, *83*, 1077. (b) Penn, R. L.; Banfield, J. F. *Science*, **1998**, *281*, 969. (c) Penn, R. L.; Banfield, J. F. *Geochim. Cosmochim. Acta.*, **1999**, *63*, 1549. (d) Banfield, J. F.; Welch, S. A.; Zhang, H.; Ebert, T. T.; Penn, R. L. *Science*, **2000**, *289*, 751. (e) Penn, R. L.; Oskam, G.; Strathmann, T. J.; Searson, P. C.; Stone, A. T.; Veblen, D. R. *J. Phys. Chem. B*, **2001**, *105*, 2177.
16. Alivisatos, A. P. *Science*, **2000**, *289*, 736.
17. Ahniyaz, A.; Sakamoto, Y.; Bergström, L. *Proc. Natl. Acad. Sci.*, **2007**, *104*, 17570.
18. Ryan, K. M.; Mastroianni, A.; Standi, K. A.; Uu, H. T.; Alivisatos, A. P. *Nano. Lett.*, **2006**, *6*, 1479
19. (a) Simon, P.; Zahn, D.; Lichte, H.; Kniep, R. *Angew. Chem. Int. Ed.*, **2006**, *45*, 1911. (b) Busch, S.; Dolhaine, H.; DuChesne, A.; Heinz, S.; Hochrein, O.; Laeri, F.; Podebrad, O.; Vietze, U.; Weiland, T.; Kniep, R. *Eur. J. Inorg. Chem.*, **1999**, 1643.
20. Kawska, A.; Hochrein, O.; Brickmann, J.; Kniep, R.; Zahn, D. *Angew. Chem. Int. Ed.*, **2008**, *47*, 4982.
21. Zhang, Q.; Liu, S.-J.; Yu, S.-H. *J. Mater. Chem.*, **2009**, *19*, 191.
22. Nanai, L.; George, T. F. *J. Mater. Res.*, **1997**, *12*, 283.
23. (a) Hoyer, P. *Langmuir*, **1996**, *12*, 1411. (b) Cepak, V. M.; Hulteen, J. C.; Che, G.; Jirage, K. B.; Lakshmi, B. B.; Fisher, E. R.; Martin, C. R. *Chem. Mater*. **1997**, *9*, 1065.
24. Chen, X. Y.; Qiao, M. H.; Xie, S. H.; Fan, K. N.; Zhou, W. Z; He, H. Y. *J. Am. Chem. Soc.*, **2007**, *129*, 13305.
25. Ueda, S.; Koizumi, M. *Amer. Mineral*, **1979**, *64*, 172.

26. Greer, H.; Wheatley, P. S.; Ashbrook, S. E.; Morris, R. E.; Zhou, W. Z. *J. Am. Chem. Soc.*, **2009**, *131*, 17986.
27. Greer, H. F.; Zhou, W. Z.; Alam, N.; Mokaya, R. *J. Mater. Chem.*, **2012**, *22*, 23141.
28. (a) Zhou, W. Z. *Adv. Mater.*, **2010**, *22*, 3086. (b) Yao, J. F.; Li, D.; Zhang, X. Y.; Kong, C. H.; Yue, W. B.; Zhou, W. Z.; Wang, H. T. *Angew. Chem. Int. Ed.*, **2008**, *47*, 8397. (c) Ritchie, A. W.; Watson, M. I. T.; Turnbull, R.; Lu, Z. Z.; Telfer, M.; Gano, J. E.; Self, K.; Greer, H. F.; Zhou, W. Z. *CrystEngComm*, **2013**, *15*, 10266. (d) Self, K.; Telfer, M.; Greer, H. F.; Zhou, W. Z. *Chem. Eur. J.*, **2015**, *21*, 19090.
29. Self, K.; Zhou, H.; Greer, H. F.; Tian, Z. R.; Zhou, W. *Chem. Commun.*, **2013**, *49*, 5411.
30. Zheng, C. M.; Greer, H. F.; Chiang, C. Y.; Zhou, W. Z. *CrystEngComm*, **2014**, *16*, 1064.
31. Liu, Z.; Chiang, C.-Y.; Li, W.; Zhou, W. Z. *Chem. Commun.*, **2015**, *51*, 9350.
32. Zhou, W. Z.; Greer, H. F. *Eur. J. Inorg. Chem.*, **2016**, DOI: 10.1002/ejic.201501342.
33. Scherrer, P. *Göttinger Nachrichten Gesell.*, **1918**, *2*, 98.
34. Uvarov, V.; Popov, I. *Mater. Charact.*, **2013**, *85*, 111.
35. Pyrz, W. D.; Buttrey, D. J. *Langmuir*, **2008**, *24*, 11350.
36. Greer, H. F.; Zhou, W. Z. *Crystallogr. Rev.*, **2011**, *17*, 163.

Chapter 2. Experimental

This chapter will describe the methods used to synthesise, analyse and characterise each of the materials that were studied during the course of this research. Details will also be given of how and why these methods were employed and the background of how each of the characterisation techniques operates.

2.1 Synthetic Methods

All of the materials synthesized during this work were produced using either hydrothermal or solvothermal methods. These techniques have a long history of being used to produce both crystalline and non-crystalline inorganic materials under elevated temperatures and, generally, under elevated pressure via the use of a sealed autoclave. In a hydrothermal system the synthesis is carried out in an aqueous solution whereas in a solvothermal system the solution is non-aqueous. In the current work these techniques are favourable over other synthetic methods for studying the crystal growth of the products due to their typically low temperatures, uniformity through the solution and precise control over crystal size and morphology (1).

In a typical synthesis the metal salts, organic agents or other reactants are dissolved into the chosen solution, which is then stirred thoroughly to ensure homogeneity before being transferred into a Teflon-lined autoclave, sealed and heated in an oven to the required temperature for a specific number of hours or days. The products from the reaction are then collected (via centrifugation for powder samples), washed and dried before further analysis and characterisation is carried out.

The specific details of the experiments, in particular the synthetic conditions, for individual specimens are described in the relevant chapters.

2.2 Characterisation Techniques

In order to determine the crystallinity, particle-size distributions and ultimately the non-classical growth mechanism of the materials which have been synthesized during the

course of this research, several different characterisation techniques have been used: scanning electron microscopy (SEM), transmission electron microscopy (TEM), high resolution TEM (HRTEM), selected area electron diffraction (SAED), energy dispersive X-ray spectroscopy (EDX), powder x-ray diffraction (PXRD), thermal gravimetric analysis (TGA) and gas adsorption studies.

2.2.1 Scanning Electron Microscopy (SEM)

Scanning electron microscopy has been used extensively in this research as it is such a useful technique for analysing the morphology and surface structure of solid state materials. SEM has been used in this work to examine and provide direct images of the different morphologies of the crystals across a range of growth times in order to establish the exact mechanism by which they grow. It was also used to provide information on the external morphologies and particle size distribution.

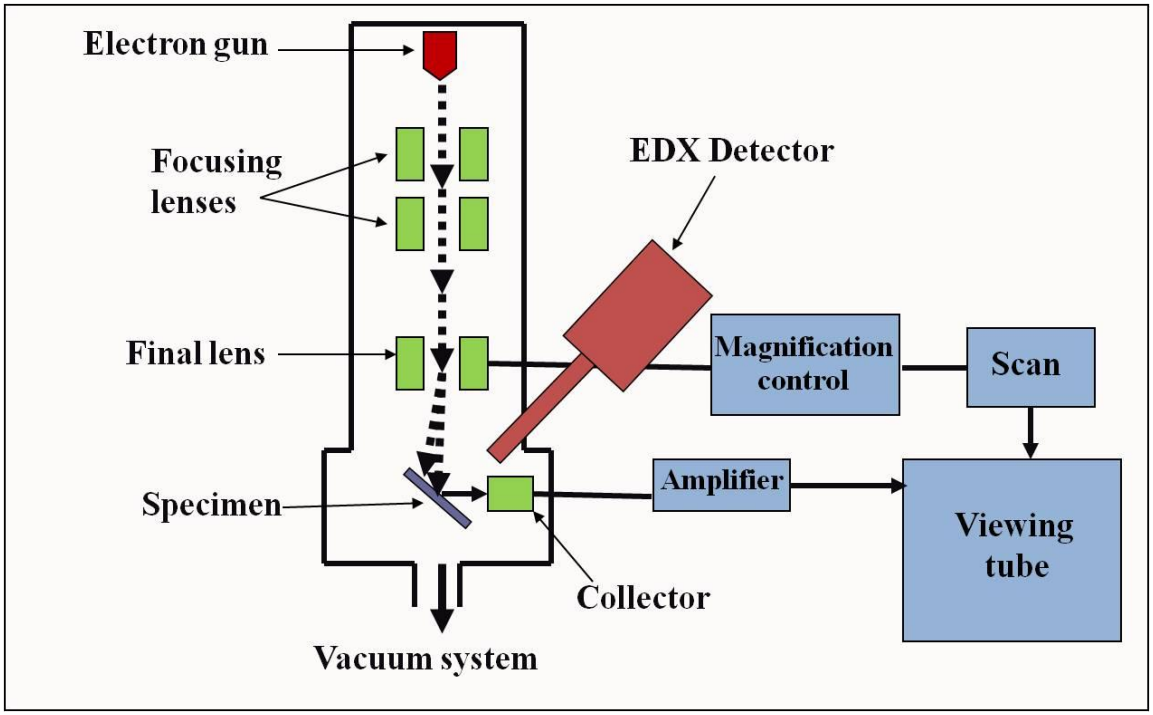

Figure 2.1. Diagram of the major components in a SEM (2).

SEM images were obtained by using a Jeol-JSM-6700F field-emission gun microscope, which is capable of magnifying a specimen up to 300,000 times and which also has the capability of determining the elemental configuration of a specimen via its EDX analysis system (Figure 2.1). The SEM was operated at 1 to 5 kV with Gentle Beam (GB) mode, which decelerates incident electrons just before they reach the sample, slightly reducing the depth to which the electrons penetrate and therefore decreasing any charging of the sample.

In any SEM, the specimen is bombarded with a beam of high energy electrons which are emitted from the 'electron gun' (Figure 2.1), which is situated at the top of the microscope column. In a standard SEM the gun is fitted with a tungsten filament that, upon heating to a temperature in excess of 2700 °C, emits a beam of electrons with an accelerating voltage of 1-30 kV that travel vertically down the microscope column towards the specimen. In a field emission gun (FEG) SEM such as the one used in the current work, however, the beam of electrons are released from the surface of a cold-cathode single crystal tungsten tip (with a radius of only ~ 100 nm) when a strong electric field is applied between this tungsten cathode and a metal anode. The electron beam produced in this case is much narrower and more coherent and has a current density one thousand times greater than that of a standard SEM. The image resolution is, therefore, much improved resulting in higher quality images being obtained at lower accelerating voltages (3).

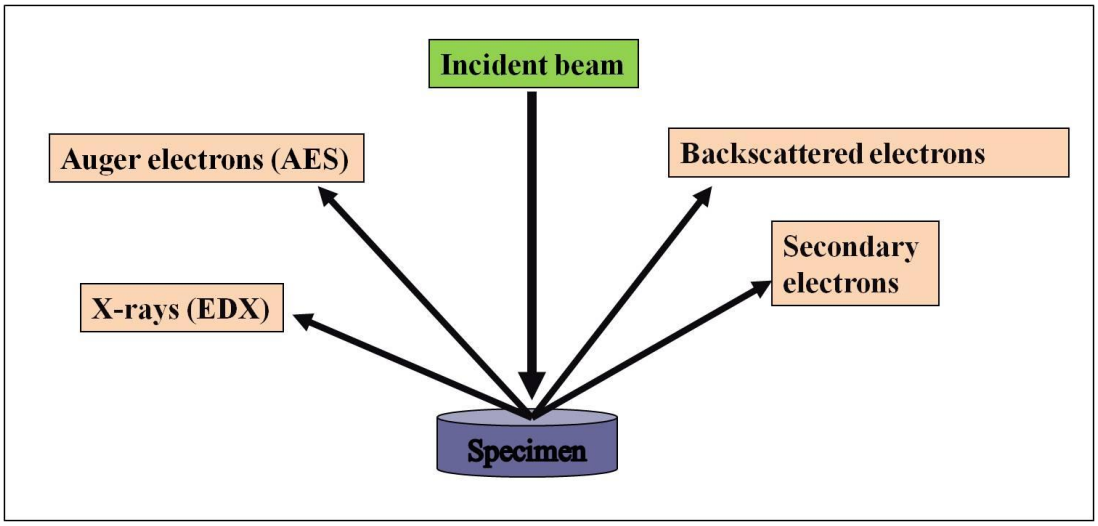

Figure 2.2. An illustration of the electrons and energy generated when the incident electron beam collides with a solid specimen in a SEM (2).

A series of electromagnetic lenses throughout the length of the microscope column are used to focus and direct the beam towards the specimen (Figure 2.1). First, a set of magnetic condenser lenses and condenser apertures focus the beam onto a small area of the sample and also remove the high angled electrons. A second set of condenser lenses then ensure that the beam is narrow and coherent before it passes through the final lens where pairs of scanning coils deflect it in the x and y axes to create a grid of parallel lines over a rectangular area of the sample (4). Upon collision of the incident electron beam with the specimen, a combination of elastic and inelastic scattering events causes further electrons and x-rays to be emitted from the specimen (Figure 2.2). The incident beam is scanned across the specimen, giving multiple signals which are amplified and then displayed as different levels of brightness on the viewing screen (a cathode ray tube, CRT), i.e. an image is generated (5).

In order to create an image in SEM, both the backscattered electrons and secondary electrons can be collected by detectors and then converted into a signal. Backscattered electrons have a very similar energy to that of the incident beam as they are the result of elastic collisions of the incident beam with atoms in the specimen and so there is no significant energy loss. The higher the atomic number of the elements within the sample, the more backscattered electrons they will produce and therefore the brighter the signal detected by the SEM. Backscattered electron analysis is, therefore, most often used to obtain compositional data by observing the differences in contrast across a sample surface. Conversely, secondary electrons are the result of the incident electrons colliding inelastically with the specimen and so have much lower energy than the incident electron beam (i.e. typically around 50 eV). Secondary electrons are emitted when the energy from the incident beam causes the specimen atoms to ionise and so are collected in the SEM from the top few nanometres of the specimen surface (6).

In this research, samples were prepared in a variety of ways to be analysed for SEM analysis. For all samples, a spin-coater was used to coat the sample with a thin layer of gold before insertion into the SEM. This was done to avoid any beam charging effects (7) which can be a problem when studying non-conductive samples via SEM as shown in Figure 2.3. When a high energy electron beam is incident on a poorly conductive material, there can be a build up of electrostatic charge on the surface. This creates an electric field, deflecting the electron beam and causing image distortion. The charge can be either negative or positive depending on whether the number of electrons striking the sample is lesser or greater than the total number of backscattered and secondary electrons the sample produces. The application

of a thin layer of conducting material (i.e. gold in the current work) on the specimen surface provides a conduction path from the specimen surface to ground. The coating must be of the correct thickness to ensure the charging effects are overcome but must also not be so thick that the original topology of the sample is lost.

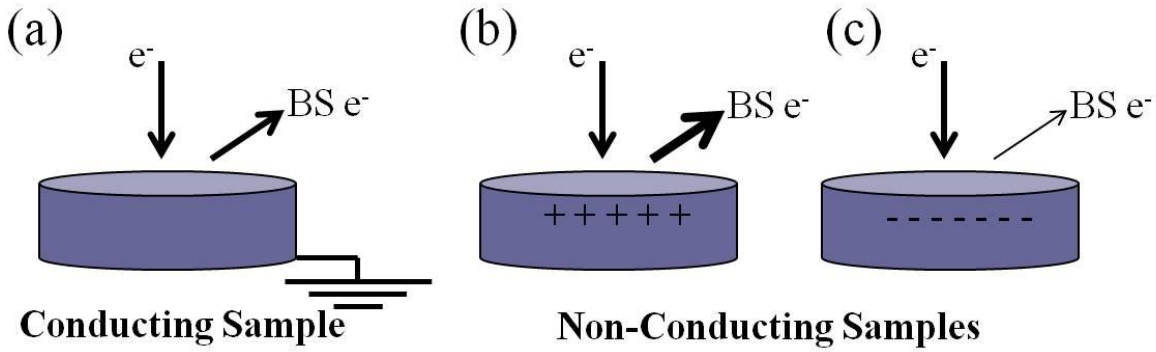

Figure 2.3. Illustration to show the beam charging effect on samples in a SEM. In a conductive sample no charging occurs (a). In non-conductive samples, an electrostatic charge builds up on the surface that is either positive (b) or negative (c) depending on the relative amount of backscattered electrons (BS e^-) produced compared to the amount of incident electrons.

For most of the samples, a very small amount of the powder was placed onto some conductive, double-sided carbon tape. This tape was then stuck onto a metal sample stub and placed in a SEM sample holder. The ZnO samples, however, were often analysed directly on the glass slide on which they had grown. The glass slides were, therefore, cut to an appropriate size and placed directly in the sample holder (fastened down by again using double-sided carbon tape).

2.2.2 Transmission Electron Microscopy (TEM)

This is another very useful characterization technique that uses a high energy electron beam to probe a sample. The difference between this technique and SEM is that in TEM only the electrons which pass through the sample to reach a detector underneath are analysed (as opposed to SEM where the electrons that are reflected/emitted by the sample are detected). This is illustrated in Figure 2.4.

TEM has been used throughout this research to analyse the internal structure, crystallinity and composition of the various materials which have been synthesized (8). Samples were analysed using a JEOL JEM-2011 transmission electron microscope, which is fitted with a LaB_6 filament in the electron gun and operates at an accelerating voltage of 200 kV. The vacuum pressure in this kind of electron gun must be constantly maintained as the LaB_6 filament could easily become contaminated if it comes into contact with oxygen, limiting the life time of the filament. The electron beam is generated by heating the LaB_6 filament to 1400-2000 K under a vacuum of a minimum 1.33×10^{-2} Pa.

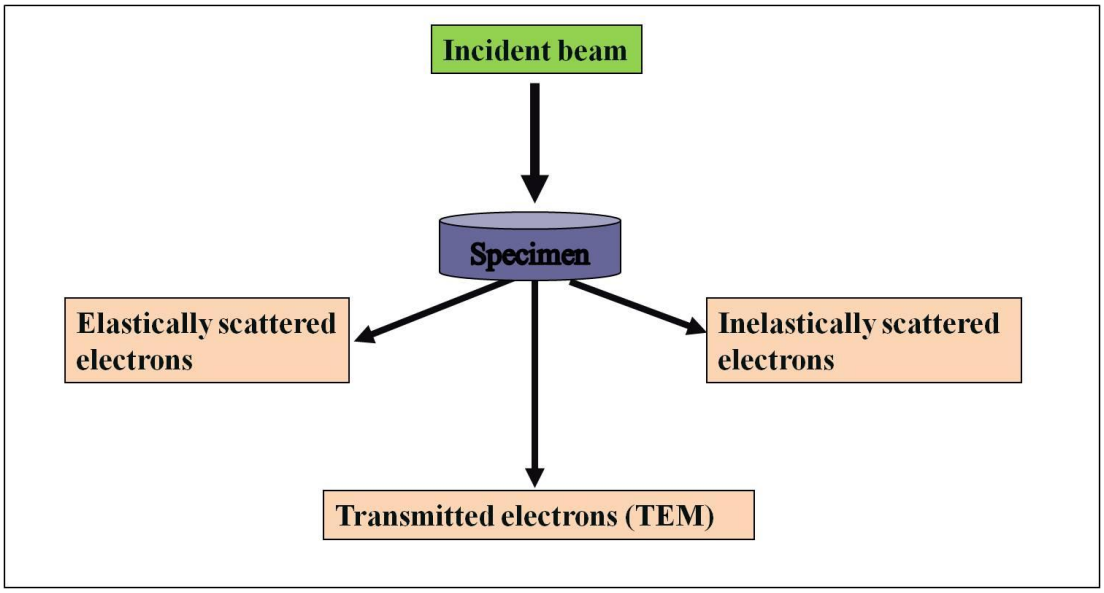

Figure 2.4. TEM detects only the electrons which pass through the specimen (2).

Through the use of several different electromagnetic lenses inside the microscope column, a much higher resolution image is able to be taken on this microscope than that used for SEM. The maximum magnification achievable is 1,200,000 times with a resolution of up to 0.18 nm (2). High resolution TEM (HRTEM) was performed to give the highest resolution images possible, providing important information on the crystallinity of the particles. Two-dimensional HRTEM images and SAED patterns were achieved via the use of a double tilt holder, which is capable of tilting the sample ±20° in both the x and y directions. A Gatan 794 CCD camera was used to record both the TEM and the HRTEM images obtained during the course of this research (9).

Figure 2.5 below displays the inner workings of a TEM where an electron beam is generated under vacuum and focused and directed down the microscope column by an anode with a potential difference of about 200 kV before being directed towards the sample by the electromagnetic condenser lens, which ensures the beam is coherent. The electrons that pass through the sample are further focused by the electromagnetic objective lens, forming the first intermediate image (with a magnification of around 50 to 100 times) and diffraction pattern. A series of projector lenses then increases the magnification before the electrons eventually hit the fluorescent viewing screen at the base of the column.

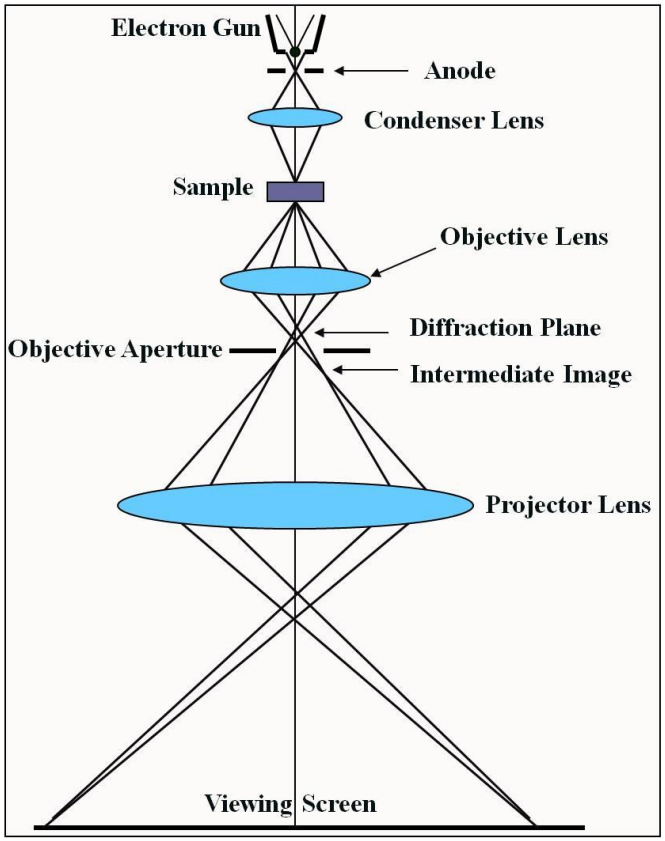

Figure 2.5. Illustration of the major components inside the microscope column of a TEM (2).

The resolution of HRTEM images is highly dependent on the optics of these lenses but issues such as spherical aberration and astigmatism often arise due to imperfect construction of the lenses and so these must be overcome whilst operating the microscope. Spherical aberration results in electrons passing through the outer edge of the lens to be more strongly refracted than those passing through its centre and so they are focused at different

points along the optical axis. This effect is overcome by recording TEM images using underfocus conditions, which can cancel out the distortion. Transmission Electron Aberration-Corrected Microscopes (TEAM) have been designed that can have a resolution of up to 0.05 nm but these are rare and highly expensive (10). Astigmatism can generally be completely corrected via the use of stigmators fitted to the objective lens.

In this research project, specimens were prepared for characterization by TEM by being crushed with a pestle and mortar and then suspended in acetone (the ZnO samples that had been grown on glass slides were simply scraped off their slide into the mortar). A single drop of this suspension was then dropped onto a copper grid with a diameter of 3 mm which has a thin, holey, carbon film coating. In TEM it is essential that only a very small amount of sample (less than about 200 nm thick) is placed onto the holder as only the electrons that can pass through the specimen to reach the detector are analysed (i.e. the sample must be 'electron transparent'). Hence, only a very small amount of the solution should be added at a time and so the first drop was left to dry in air at room temperature before any more of the suspension was added. Once the grid was completely dry, it was carefully placed onto the double tilt sample holder and inserted into the TEM.

2.2.3 Selected Area Electron Diffraction (SAED)

SAED is a crystallographic technique which is used alongside TEM to give a diffraction pattern of a sample which can, in turn, be used to give information about the crystal structure (2). In this technique a 'selected area aperture' is used (which is located just below the specimen holder in the microscope column) that allows the user to select just the desired very small area of the specimen to analyse (hence the name 'selected area' electron diffraction). The aperture is simply a very thin strip of metal with differently sized holes, which is inserted directly into the path of the electron beam, blocking all but a very small fraction of the transmitted electrons. Only the selected area will, therefore, contribute to the electron diffraction pattern. In this research SAED was used in particular to determine the crystallinity of the core of the ZnO nanocones and the Cu_2O crystals.

During this research, SAED patterns were obtained using the Jeol JEM-2011 transmission electron microscope (described in section 2.2.2 above). As previously mentioned, a specimen must be very thin (less than 200 nm thick) to be analysed in a TEM

and the incident electron beam passes through the specimen to the objective lens below (Figure 2.5). Since the spacing between sample atoms is approximately one hundred times greater than the wavelength of the high-energy electrons (which is a few thousandths of a nanometre), the atoms act as a diffraction grating to the electrons. A certain fraction of the incident electrons will, therefore, be reflected or scattered at different angles. The angle of diffraction is dependent on the unique crystal structure of the specimen (11). The diffracted electrons reach the objective aperture electromagnetic lens, which focuses them to form a series of diffraction spots (i.e. a selected area electron diffraction pattern).

There are three basic types of SAED pattern that can be obtained from powder samples. The first appears as solid, diffuse, circular bands with no clear spots and indicates that the material is amorphous. Patterns with rings made up of individual spots imply a polycrystalline material and, finally, patterns with clear, individual spots in a two dimensional arrangement show a single crystalline material.

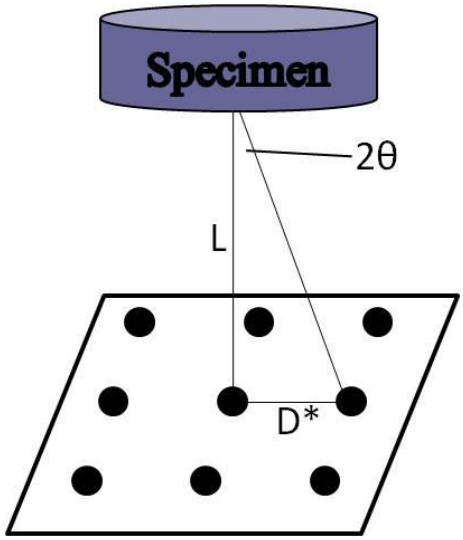

Figure 2.6. Illustration to show how the reciprocal d-spacing can be measured from the SAED pattern through the use of the distance between the camera and the sample (L), the distance between diffraction spots (D*) and the diffraction angle (2θ).

These single crystal patterns can be used to determine what material is present through calculating the reciprocal d-spacing (d^*_{hkl}) by measuring the distance between diffraction spots (D*) as shown in Figure 2.6. Equation 2.1 can then be used where L is the

camera length, d_{hkl} is the d-spacing, and λ is the wavelength of the electron beam (which is 2.51 x 10^{-3} nm at an accelerating voltage of 200 kV) (12).

$$d_{hkl} = \frac{1}{d^*_{hkl}} = \frac{\lambda}{2sin\theta} = \frac{L\lambda}{D^*} \quad (2.1)$$

In the case that the unit cell of the material is already known, the diffraction pattern can then simply be indexed. If the unit cell is not known, however, the d-spacings from two or more diffraction patterns should be calculated to first determine the unit cell. The indexing can then be checked by comparing the angle measured between two diffraction spots to the theoretical angle that should exist between the two crystal planes.

2.2.4 Energy Dispersive X-ray Spectroscopy (EDX)

EDX is a technique used to provide elemental analysis of individual particles in a sample and can detect any element with an atomic number larger than 11 with a reasonably high degree of accuracy (although lighter elements can also be detected) (13). In this research EDX was used to determine the elements present in early stage samples in a range of materials, generally in polycrystalline aggregates but also in other samples such as the polymer film which formed on the surface of the glass slides in the ZnO experiments.

In EDX, the specimen is bombarded by a beam of high-energy electrons, leading to the formation of x-rays which can be detected and turned into a signal. The x-rays are emitted because as an incident electron collides with a sample it causes a secondary electron to be ejected from the sample atom as shown in Figure 2.7. The electrons with the lowest energy will be the first to be ejected. These are the electrons from the innermost (K-) shell (the shells are labelled K, L, M etc from the innermost shell, closest to the nucleus, outwards). In order to stabilise the ion, the vacancy in the K-shell will be filled by a higher energy electron 'falling' to the lower energy shell, producing an x-ray with energy equal to the difference between the two shells (Figure 2.7b). As the energies of the shells are unique to each element, so are the x-rays produced and so by analysing the energy and intensity of these x-rays, the elemental composition of the sample can be determined.

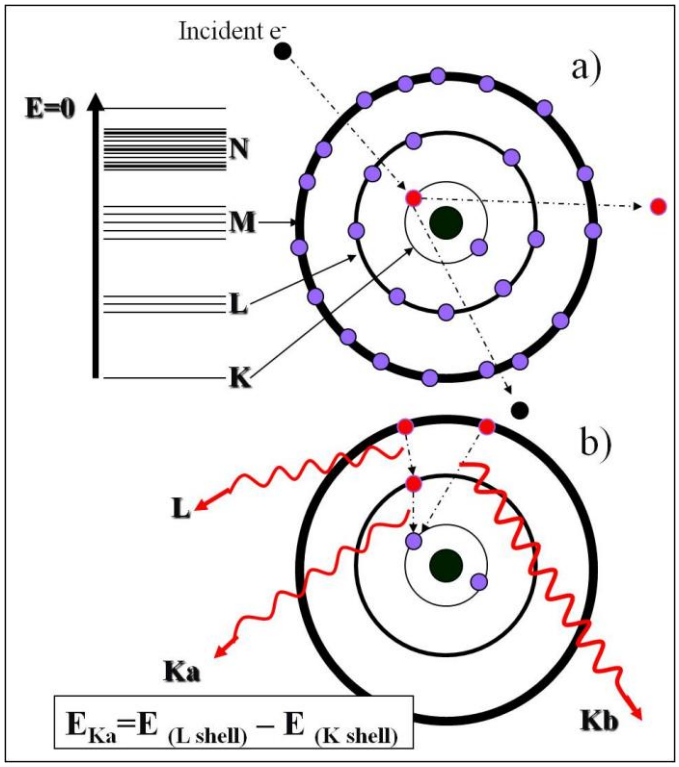

Figure 2.7. (a) Schematic of an electron from the K-shell being emitted from an atom. (b) Schematic of an electron dropping from the higher-energy L-shell to fill the vacancy in the K-shell the energy of the corresponding x-ray (2).

In the present work, an Oxford Instruments X-ray Analysis ISIS 300 system with a silicon detector and beryllium window attached to a JEOL JSM-5600 scanning electron microscope was used to perform EDX with the working distance set at 20 mm. This system permits both EDX and SEM analysis to be carried out successively. The accelerating voltage in the EDX needs to be chosen carefully. It must be a minimum of double the highest excitation energy (in kV) of any elements which may be present in the sample. Additionally, a high voltage is used in order to increase the intensity of the X-rays whilst not raising it so high that it could damage the sample.

2.2.5 Powder X-Ray Diffraction (PXRD)

PXRD is a technique frequently used for phase identification of a sample and to give information on crystal structure. Although SEM, TEM, SAED and EDX can give important information on the local microstructure of materials, PXRD is helpful when it is necessary to

study the bulk powder (for example, to determine if the material is made up of multiple phases). In this research, PXRD patterns were obtained by using a PANalytical Empyrean diffractometer, where the Cu K_α x-ray source (with a wavelength of 0.15418 nm) was produced by bombarding copper metal with high-energy electrons. The patterns produced were analysed using the Highscore Plus software. PXRD has been used in this research to identify the phases present in each of the materials studied and to support crystallinity data that had been obtained through SAED (14).

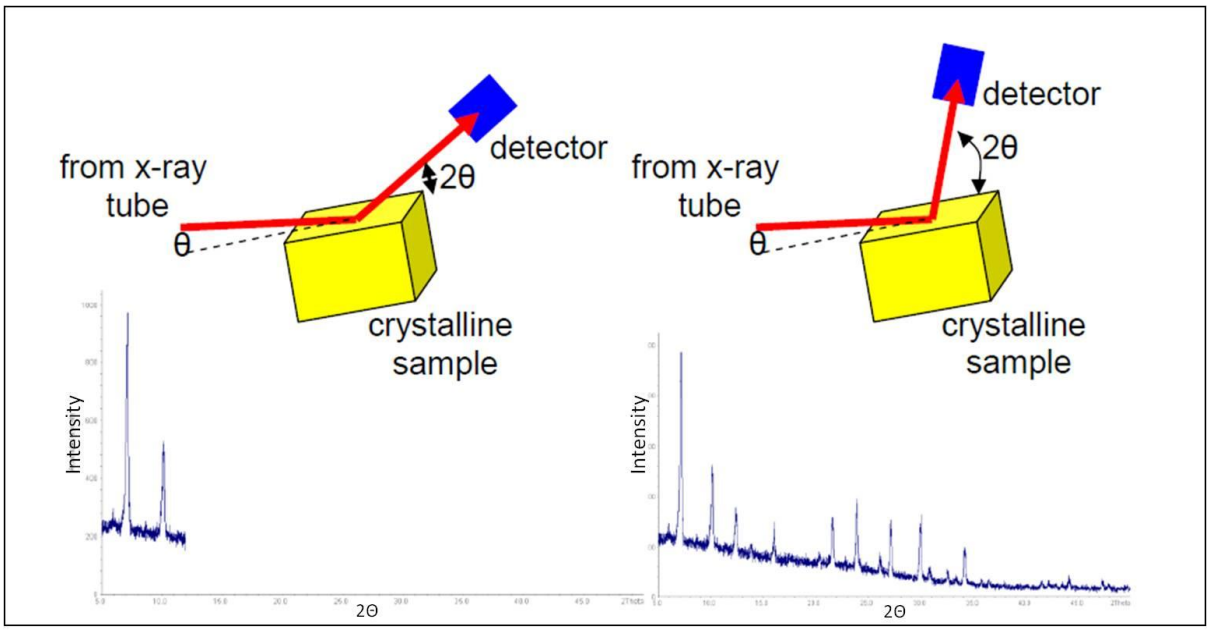

Figure 2.8. Illustration of the formation of PXRD patterns in reflection mode. The patterns were obtained by rotating the angle between the sample and detector across a range of 2θ values (15).

In order to prepare specimens for PXRD analysis, the powder samples were finely ground to ensure homogeneity and then carefully deposited onto a low background silicon wafer, which had been coasted with a thin layer of petroleum jelly. This wafer was then placed inside a specialised PXRD holder. Data was collected in reflective mode where the incident high energy X-rays penetrate the sample a number of microns beneath the surface before being deflected towards a detector (Figure 2.8). The alternative method to this is to collect the data in transmission mode where the high energy X-rays travel through the sample and are collected by the detector on the other side. Due to the randomly oriented nature of the crystalline domains in a powdered sample, either mode should produce the same data. In both

cases, a monochromator (an optical device that only transmits a selective wavelength of light) is used to allow only Cu K_α radiation to reach the detector and to filter out any unwanted X-rays such as Cu K_β radiation. In reflection mode, the monochromator is positioned over the detector, whereas in transmission mode the X-rays pass through the monochromator before reaching the sample.

To enable us to observe all possible peaks, the detector will be rotated through a range of 2θ values (see Figure 2.8) and the number of counts at each angle will be recorded, allowing the computer to generate the XRD pattern. The range of angles should be selected based on where peaks should appear for the phases present in the sample. For example, in this project the range of 2θ values used was 5° to 80° for the ZnO samples and 10° to 80° for the $CaCO_3$ samples as there were no expected peaks below 10° for $CaCO_3$. The scanning speed can also be altered by the user in order to regulate the time it takes to acquire the spectrum and to adjust the signal-to-noise ratio for the diffraction peaks. As every peak in the PXRD pattern corresponds to a different d-spacing, and as every crystalline material has unique d-spacings, the PXRD patterns can be compared to standard reference diffraction patterns from databases such as the Inorganic Crystal Structure Database (ICSD) in order to determine which materials/phases are present (16).

In PXRD the 3D arrangement of atoms within a crystalline sample acts as a diffraction grating to the incident X-ray beam. The atoms are arranged into planes of various orientations with an interplanar distance, d. When the X-rays reach these planes they interact with the electrons in the atoms and are diffracted at a range of angles. The mix of constructive and destructive interference of the diffracted beams then generates the diffraction pattern. Sharp, crystalline peaks are observed in the patterns when Bragg's Law, Equation 2.2, is obeyed where n is an integer number, λ is the wavelength of the incident X-rays, d is the distance between planes in the atomic lattice and θ is the angle between the incident X-ray and the atomic plane (known as the Bragg angle).

$$n\lambda = 2d\sin\theta \qquad (2.2)$$

The parameters for Bragg's Law are illustrated in Figure 2.9 where it can be seen that an incident X-ray interacting with an inner plane of atoms (labelled b) must travel further

than an X-ray which interacts with an outer plane (labelled a). The extra length travelled by beam b is equal to 2dsinθ. Bragg's Law is satisfied, and therefore constructive interference occurs, only when this distance is equal to an integer number of multiples of the wavelength of the incident radiation.

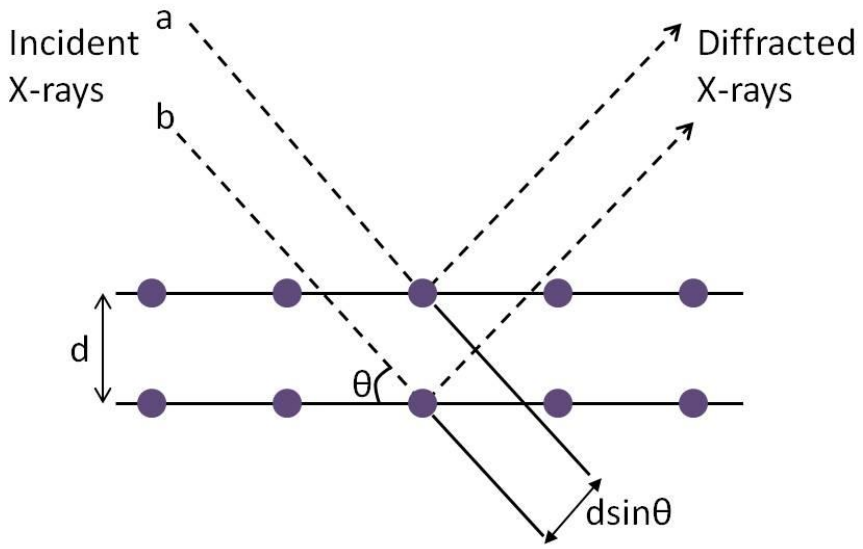

Figure 2.9. Illustration of the parameters used to derive Bragg's Law.

The broadening of the peaks in PXRD patterns can be used to determine the average size of ordered, crystalline domains, τ, using the Scherrer equation (Equation 2.3) where K is the shape factor, λ is the wavelength of the incident X-rays, β is the line broadening of a peak at half the maximum intensity in radians (also referred to as the full width at half maximum, FWHM) and θ is the Bragg angle. The shape factor, K, is dimensionless with a value close to unity, it varies with the actual shape of the crystallite so in the current work when the Scherrer equation is used, calculations are based on K = 0.92 as this is the typical value for a spherical crystallite (17).

$$\tau = \frac{K\lambda}{\beta cos\theta} \qquad (2.3)$$

2.2.6 Thermal Gravimetric Analysis (TGA)

TGA is a highly accurate thermal analysis technique used to observe alterations in the weight of a sample upon increasing the temperature whilst maintaining a constant heating rate. This technique is generally used to study materials which undergo phase transitions, such as sublimation or desorption, and therefore display mass loss or gain as a function of temperature. The basic set up for TGA is composed of a programmable, high accuracy furnace equipped with a thermocouple which contains a precision balance (usually a quartz microbalance). The sample (typically around 15 mg) is simply loaded into a crucible made of alumina or platinum and placed onto the balance. The furnace is programmed to a constant heating rate under a specific gas and then the mass of the sample is continuously monitored before being plotted as a function of temperature once the process is complete (18). Sometimes, if necessary, a reference sample may be inserted into another chamber on a different balance.

In this work, TGA was carried out to determine the amount of organic present in Cu_2O samples and also to observe the phase transition from Cu_2O to CuO. TGA was performed using a Stanton Redcroft STA-780 series instrument at a heating rate of 5 °C per minute in a constant flow of air.

2.2.7 Gas Adsorption

Inert gas adsorption is a very useful characterisation technique often employed in the study of mesoporous materials to determine pore-related information such as pore size distribution, specific surface area and pore volume. Gas adsorption isotherms can be acquired by recording the gas uptake of a material as a function of increasing or decreasing relative pressure whilst maintaining a constant temperature. Adsorption can be described as a process of adhesion in which a layer of the adsorbate (gas molecules) is formed on the surface of an absorbent (i.e. a porous material). The quantity of molecules adsorbed can be determined either volumetrically or gravimetrically. The resulting isotherms can be classified into six different types as shown in Figure 2.10 (19).

Hysteresis loops, such as those observed in isotherms type 4 and 5, are indicative of mesoporous materials, which typically have high surface areas and uniform, large pore sizes.

The hysteresis loops in gas adsorption-desorption isotherms can be classified into four different types, each describing different pore structures within a material. For example, hysteresis loop Type H_1 displays parallel, almost vertical branches (such as that shown in Type 4 in Figure 2.10) and represents materials that have very uniformly sized pores. Hysteresis loop Type H_4, on the other hand, displays parallel, almost horizontal branches and is characteristic of materials with narrow, slit-like pores or materials with a high degree of structural defects (20).

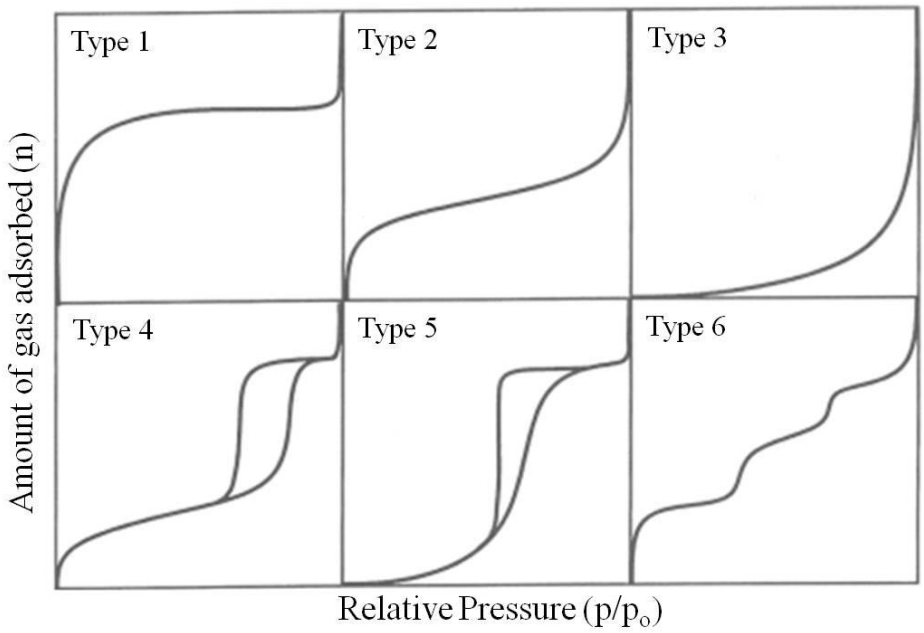

Figure 2.10. The six different classifications of gas adsorption isotherms: Type 1 shows a Langmuir isotherm indicative of a microporous structure. Type 2 depicts the typical gas adsorption by non-porous solids. Type 3 shows weak interactions between the adsorbant and adsorbate, which is related to both microporous and non-porous adsorbents. Type 4 is similar to Type 2 but the presence of a hysteresis loop indicates the presence of mesopores alongside the micropores. Type 5 is similar to Type 3 in that it shows weak adsorbate-adsorbent interactions but, again, the hysteresis loop is associated with the presence of mesopores. Finally, Type 6 is a more hypothetical isotherm depicting layer by layer adsorption on a uniform surface where a full monolayer of the gas is adsorbed before each subsequent layer is deposited, resulting in the step-like isotherm where the step height corresponds to the monolayer capacity (21).

There are many different methods that can be employed to calculate the surface area from adsorption isotherms. One method which is advantageous as it accounts for multi-layer adsorption is the Brunauer-Emmett-Teller (BET) model (22). As with all models, however,

some assumptions are made when using the BET method (for example, that the material has smooth surfaces and that the pores are cylindrical). The BET equation is

$$\frac{x}{N_s(1-x)} = \frac{1}{N_m C} + \frac{C-1}{N_m C}x \qquad (2.4)$$

where N_s is the quatity of adsorbed gas at relative pressure x, N_m is the quantity of adsorbed molecules in a monolayer and C is the BET constant (which is related to the adsorption heat and condensation heat of the first layer of adsorbate).

In the present work, gas adsorption studies were used to analyse the pore structure of the RHO-ZIF samples at different growth times. The as-prepared samples were first dehydrated by being heated under vacuum at 120 °C overnight and then low pressure gas adsorption (< 0.1 bar) studies were carried out using a Micromeritics Tristar II instrument under N_2. The gas uptake was measured volumetrically to produce the adsorption-desorption isotherms in this case as it allows constant contact between the sample and the liquid N_2 (at 77 K) through the glass sample wall.

2.2.8 Summary

In summary, a range of characterisation techniques have been described that have been used throughout the course of this research. The exact nature of the synthetic experiments carried out to produce each sample will be detailed in the relevant results chapter.

It is important to use multiple characterisation methods, not only to gather as much information about the sample as possible, but also to increase the reliability of that information. For example, while HRTEM can be used to index a material, it is only possible to view a very small number of particles through this method and so it is often necessary to use a bulk analysis technique, such as PXRD, alongside the HRTEM images to further validate the information attained.

References

1. Feng, S.; Guanghua, L. in *Modern Inorganic Synthetic Chemistry*, eds. Xu, R.; Pang, W.; Huo, Q. Elsevier, Amsterdam, **2011**, pp.63-95.
2. Zhou, W. Z. University of St. Andrews. Lecture notes for CH5515: Introduction to Electron Microscopy.
3. Goldstein, J. I.; Newbury, D. E.; Joy, D. C.; Lyman, C. E. Echlin, P.; Lifshin, E.; Sawyer, L.; Michael, J. R. *Scanning Electron Microscopy and X-Ray Microanalysis*, Kluwer Academic/ Plenum Publishers, New York, **2003**.
4. Egerton, R. F. *Physical Principles of Electron Microscopy: An Introduction to TEM, SEM and AEM*, Springer, Alberta, **2005**.
5. Lyman, C.E. *Scanning Electron Microscopy, X-Ray Microanalysis, and Analytical Electron Microscopy*, Springer, New York, **1990**.
6. Postek, M. T.; Howard, K. S.; Johnson, A. H.; McMichael, K. L. *Scanning Electron Microscopy A Student's Handbook*, Ladd Research Industries, **1980**. pp. 51-54.
7. Agger, J. R.; Pervaiz, N.; Cheetham, A. K.; Anderson, M. W. *J. Am. Chem. Soc.*, **1998**, *120*, 10754.
8. Tennakone, K.; Kumara, G. R. R. A.; Kottegoda, I. R. M.; Perera, V. P. S. *Chem. Commun*. **1999**, 1, 15.
9. (a) Williams, D. B.; Carter, C. B. *Transmission Electron Microscopy*, Springer, US, **1996**. (b) Reimer, L.; Kohl, H. *Transmission Electron Microscopy*, Springer, New York, **2008**. (c) Wan, D.; Komvopoulos, K. *J. Mater. Res*., **2004**, *19*, 2131. (d) Zhang, Z. *Progress in Transmission Electron Microscopy 1*, Springer, Tsinghua University Press, **2001**.
10. De Graef, M. *Introduction to Conventional Electron Transmission Electron Microscopy*, Cambridge University Press, Cambridge, **2003**.
11. Viti, C.; Frezzotti, M. *Lithos*., **2001**, *55*, 125.
12. Goodhew, P. J.; Humphreys, F. J.; Beanland, R. *Electron Microscopy and Analysis*, Taylor & Francis, London, **2001**.
13. Dykstra, M. J., Reuss, L. E. *Biological Electron Microscopy: Theory, Techniques, and Troubleshooting*, Springer, US, **2003**.
14. Huang, Y. N.; Havenga, E. A. *Chem. Phys. Lett.*, **2001**, *345*, 65.
15. Greer, H. F. Undergraduate Thesis, University of St Andrews, St Andrews, UK. **2009**, pp. 9.

16. Langford, J. I.; Louer, D. *Rep. Prog. Phys.* **1996**, *59*, 131.
17. Scherrer, P. *Göttinger Nachrichten Gesell.*, **1918**, *2*, 98.
18. Menczel, J. D.; Prime, R. B. *Thermal Analysis of Polymers: Fundamentals and Applications*, Wiley, New Jersey, **2009**.
19. Wright, P. A. *Microporous Framework Solids*, RSC Publishing, **2008**.
20. Zhao, D. Y.; Wan, Y.; Zhou, W. Z. *Ordered Mesoporous Materials*, Wiley-VCH, **2013**.
21. (a) Brunauer, S.; Deming, L. S.; Deming, W. S.; Teller, E. *J. Am. Chem. Soc.*, **1940**, *62*, 1723. (b) Alhamami, M.; Doan, H.; Cheng, C.-H. *Materials*, **2014**, *7*, 3198.
22. Brunauer, S.; Emmett, P. H.; Teller, E. *J. Am. Chem. Soc.*, **1938**, *60*, 309.

Chapter 3. Non-Classical Crystal Growth of Zinc Oxide Decorated Microstadiums

3.1 Introduction

Over recent years there have been many investigations into the shape, size and structure of different zinc oxide, ZnO, crystals (1) as they are widely used in industry and if their morphology can be carefully controlled it may be possible to have more careful control of their chemical and physical properties. ZnO is a material of particular interest in industry as, with a wide band gap of 3.37 eV (2), it is a low-cost semiconductor material with a range of possible applications due to its catalytic (3), electrical (4), optoelectronic (5) and photoelectrochemical (6) properties.

The hexagonal, wurtzite structure is the most common phase of zinc oxide under ambient conditions and is made up of alternating planes of tetrahedrally coordinated O^{2-} and Zn^{2+} ions stacked along the c-axis (Figure 3.1). This results in the wurtzite structure having no centre of inversion which, combined with large electromechanical coupling, gives rise to strong pyroelectric and piezoelectric properties and so ZnO is often used in mechanical actuators and piezoelectric sensors (7).

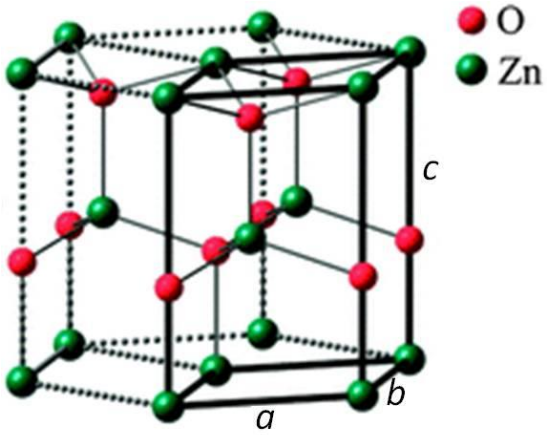

Figure 3.1. Illustration of the ZnO wurtzite structure. The unit cell is outlined with solid black lines. Adapted from Ref. 8 with permission from The Royal Society of Chemistry.

ZnO crystals have been known to grow into a large variety of different morphologies (9) and of these the highly oriented, three-dimensional arrays of hollow ZnO tube-like structures are one of the most significant as they can offer the very high porosity and surface area which are often desired to achieve high efficiencies and high activities in many industrial applications (10).

3.1.1 Reversed Crystal Growth: ZnO Microdisks

One of the most interesting forms of ZnO are highly oriented microrod arrays (11), which have been shown to grow on various substrates by aqueous thermal decomposition of the Zn^{2+} amino complex using zinc nitrate, $Zn(NO_3)_2.4H_2O$ and methenamine, $C_6H_{12}N_4$ (12). These microrods have a hexagonal morphology reflecting the hexagonal wurtzite unit cell, with a top (0001) polar surface and six $\{10\bar{1}0\}$ side surfaces. The central part of these microrods can be further dissolved to form hollow microtubes. Many other crystalline microtubes and nanotubes can also be fabricated by using various synthetic methods. For example, titanium oxide and niobium oxide based nanotubes can form via rolling up a single sheet of metal oxides (13), vanadium pentoxide microtubes have been produced via laser assisted oxidation (14) and other nanotubes have been fabricated by replication methods and template techniques (15). In comparison with these well established synthetic methods, the mechanism of selective dissolution for ZnO microtubes is not well understood and until very recently the reason for the selective dissolution was believed to be the metastability of the polar (0001) surface (10). If this was the case, however, and the microrods were true single crystals, dissolution would be expected to occur uniformly across the whole of the top (0001) surface leading to shorter microrods rather than hollow tubes.

In 2013, research was completed and published at the University of St Andrews whereby hexagonal ZnO microdisks were synthesized over a range of growth times and then were selectively dissolved by ethylenediamine, $C_2H_4(NH_2)_2$, to produce ZnO microstadiums (16). It was reported that the hexagonal microdisks were in fact not single crystals, but had a similar ‘core-shell’ structure to that observed of the zeolite analcime (17), which was discussed in Chapter 1. SEM images revealing the morphology and core-shell structure of the microdisks are displayed in Figure 3.2.

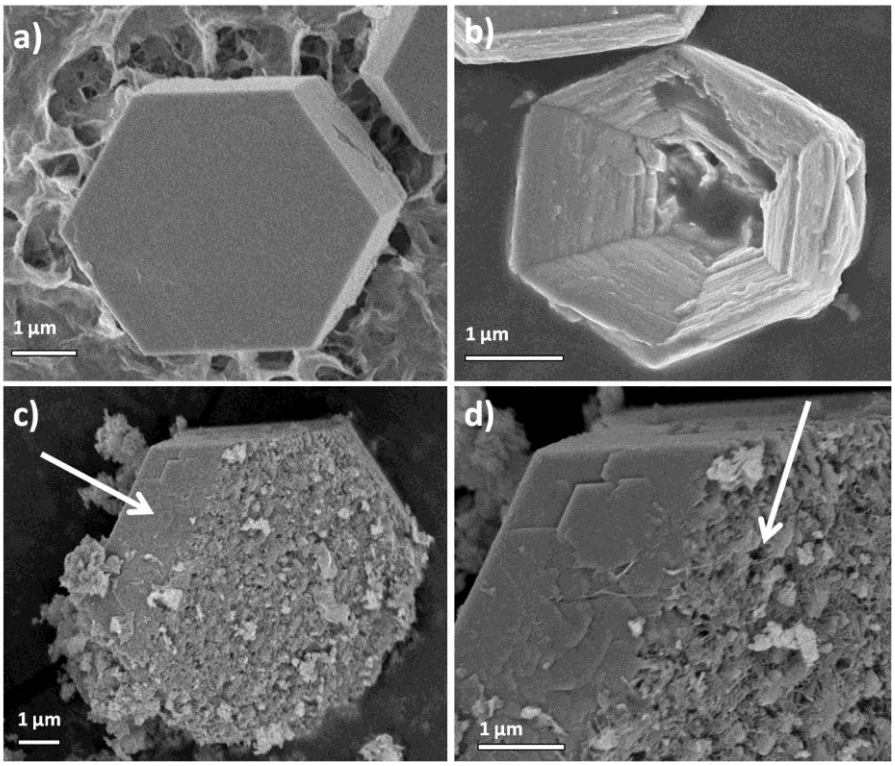

Figure 3.2. SEM images showing (a) the typical morphology of a ZnO microdisk, (b) the hexagonal microstadium that forms after selective dissolution by ethylenediamine, (c) and (d) crushed open ZnO microdisks, displaying their core-shell structure. The arrow in (c) indicates the crystalline outer layer of the microdisks and the arrow in (d) indicates the disordered, polycrystalline core.

By synthesizing hexagonal ZnO microdisks over a range of hydrothermal growth times, crushing them open and then analysing them via SEM, it could be seen very clearly that the disks were not single crystals but consisted of a disordered, polycrystalline core encased in a very thin layer of single crystal. TEM and PXRD analysis of the disks at early growth stages also revealed a zinc nitrate hydroxide, $Zn_5(NO_3)_2(OH)_8.2H_2O$, phase present in the cores which goes some way in explaining why the core would be preferentially dissolved as the hydroxide phase is a lot less stable than pure ZnO.

SEM analysis of the growth of the microdisks over time revealed that they also follow the reversed crystal growth route. Initially, aggregates of precursor material formed on a polymer film on the glass substrate. These aggregates became larger over time, gradually forming a quasi-spherical shape. Surface recrystallization then occurred with multiple nucleation sites across the surface of the aggregates, forming many small crystalline islands which grew larger over time and eventually joined together until the entire surface of the disk

was encased in a hexagonal, single crystal shell apart from the bottom surface (in contact with the polymer film on the glass substrate) which remained disordered. The observation that the base of the disks did not undergo recrystallization led to the conclusion that the preferential growth site of the disks was actually at their base, not at the top surface which would have been more conventional.

3.1.2 Zinc Oxide Decorated Microstadiums

Recently, research is also looking beyond the hollow tubular structures of semiconductor materials and focusing on well-ordered arrays of branched or dendritic structures as their unique morphologies with high surface areas and maximised spatial organization may enhance their desired optical and electronic properties (18).

After the selective dissolution of the ZnO microdisks to microstadiums, a further hydrothermal treatment with 1,3-propanediamine, $C_3H_6(NH_2)_2$, can be performed which leads to the growth of ZnO nanocones on the inner and outer surfaces of the microstadiums (Figure 3.3). It is unclear, however, why these nanocones grow as it would be far more energetically favourable for additional ZnO to grow as an extension of the existing crystal structure (i.e. via layer by layer atomic deposition on the crystal surface).

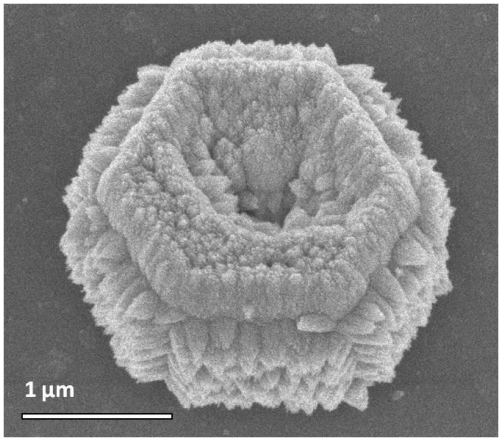

Figure 3.3. SEM image of a typical ZnO decorated microstadium formed via a three-step hydrothermal process. The final treatment with 1,3-propanediamine causes the growth of ZnO nanocones on the inner and outer walls of a ZnO microstadium.

Previous reports have shown that in an aqueous phase synthesis, the presence of an organic structure directing agent can alter the specific morphology and microstructure of a material if it is selectively adsorbed onto a crystal surface. This adsorption alters the surface chemistry of the crystal which can lead to site-specific nucleation and, therefore, secondary growth (19). The size and shape of ZnO nanocrystals have been successfully controlled by the addition of ammonia, citrate acid and poly(vinylalcohol) into the hydrothermal synthesis (20).

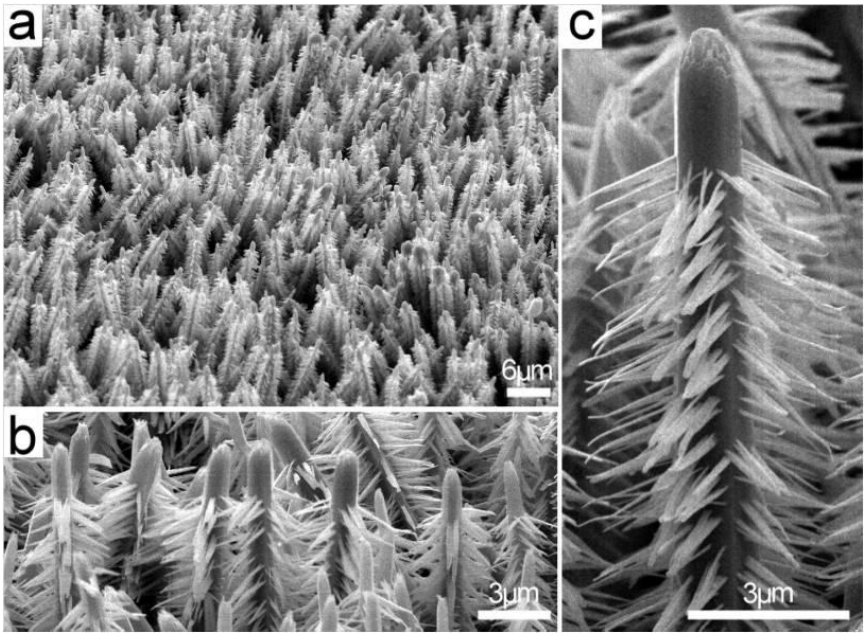

Figure 3.4. Highly oriented 'nanotree' branched ZnO structure reported by Zhao *et al.* Reproduced from Ref. 21 with permission from the American Chemical Society.

Similar morphologies of branched, well-ordered, ZnO structures have been produced by Zhao *et al.* (21). They reported the growth of ZnO 'nanotrees' (Figure 3.4) with six-fold symmetry comprised of microtrunks that are covered in ZnO nanobranches. These nanobranches grow at an oblique angle of approximately 108° to the trunk in contrast to the nanocones in the present work which grow perpendicularly to the walls of the microstadium. Zhao *et al*. Suggest that the reason for the epitaxial growth of nanobranches on the ZnO microtrunks is due to a less than 5 % lattice mismatch between the $(\bar{1}01\bar{1})$ crystal planes of the trunk and (0002) planes of the branches. There is limited evidence for this, however, and this growth route would still rely on the classical growth theory of layer by layer atomic

deposition and so the mechanism for the nucleation of secondary growth on ZnO microstructures is still poorly understood.

In the present work, a simple three step hydrothermal synthesis to form ZnO decorated microstadiums is presented. Whilst many previous reports have shown evidence of hollow or tubular ZnO microstructures (22) and of ZnO structures with secondary growth or 'branched' morphologies (21, 23), the decorated microstadiums in the present work are believed to be the first to display both these desired features. In this chapter, research has also been conducted into the orientation and growth of the nanocones to determine how this interesting, branched morphology originates and a new mechanism for their growth has been proposed.

3.2 Synthesis

A three-step hydrothermal method was used to synthesise the ZnO decorated microstadiums:

3.2.1. Synthesis of ZnO Microdisks

The first step in the experimental procedure to synthesize ZnO decorated microstadiums involved the growth of hexagonal ZnO microdisks on a glass slide:

Five glass slides were cleaned by being wiped twice on each side with a chem-wipe that had been soaked in distilled water. The slides were left to dry in air at room temperature. 1.49 g zinc nitrate, $Zn(NO_3)_2.6H_2O$ (98%, Fisher Scientific), and 0.97 g hexamethylenetetramine, $(CH_2)_6N_4$ (99%, Sigma-Aldrich), were stirred into 250 ml distilled water until fully dissolved. The resulting solution was then left to stir on a magnetic stir plate as 7.75 mg monosodium citrate, $NaC_6H_7O_7$ (Sigma Aldrich), was gradually added. This mixture was left to stir for a further 1 h, ensuring the solution was homogeneous and the citrate was fully dissolved.

One of the clean, dry glass slides was submerged at an angle of approximately 60° in 20 ml of this solution, which had been transferred to a separate vial. The vial was then sealed and heated in an oven at 60 °C for 3 days. This was repeated with each of the other glass slides in separate vials.

Once the vials were taken out of the oven, each of the glass slides were removed from their reaction vessel and their top surfaces were wiped clean with another damp chem-wipe while the bottom surfaces were left untouched. The glass slides were then submerged in a beaker of distilled water for 10 min for further cleaning before being allowed to dry in air at room temperature.

3.2.2. Selective Dissolution to form ZnO Microstadiums

In the next stage of the synthesis, the selective dissolution of the centre of the ZnO microdisks was performed to obtain so-called ZnO 'microstadiums':

In this step, 1.49 g zinc nitrate, $Zn(NO_3)_2.6H_2O$, was first dissolved in 250 ml distilled water with 3.59 g ethylenediamine, $C_2H_4(NH_2)_2$ (99.5%, Fluka), and the resulting solution was allowed to stir over 1 h on a magnetic stir plate to ensure homogeneity. Four of the glass slides that had been used as substrates for the growth of (and were now coated in) ZnO microdisks (from step 3.2.1 above), were now placed in separate reaction vessels each containing 20 ml of the aqueous nitrate/amine solution. Each vessel was then sealed and placed in an oven at 60 °C for 4 h. Once this period of incubation was complete, the slides were taken out of their reaction vessels and washed by being placed in a beaker filled with distilled water. They were left there for 10 min before being allowed to dry in air at room temperature.

3.2.3. Formation of ZnO Decorated Microstadiums

In the final stage of the synthesis, ZnO "decorated microstadiums" were formed by the growth of ZnO nanocones on the inner and outer surfaces of the ZnO microstadiums:

1.49 g zinc nitrate, $Zn(NO_3)_2.6H_2O$, was dissolved in 250 ml distilled water. Then 0.97 g 1,3-propanediamine, $C_3H_6(NH_2)_2$ (99%, Aldrich), was added and the solution was allowed to stir for 1 h on a magnetic stir plate to ensure full homogeneity. The four glass slides that were covered in ZnO microstadiums (from step 3.2.2 above) were placed in separate vessels each containing 20 ml of the aqueous solution. Each vessel was then sealed and incubated at 60 °C. One was removed after 10 min, one after 30 min, another after 40 min and the final vessel was removed after 60 min of incubation. The glass slides were then

removed from their reaction vessels and submerged in distilled water for 10 min before being allowed to dry at room temperature.

In addition to these three reactions, another glass slide that was coated in microdisks (from step 3.2.1 above) and also a plain, clean, glass slide were placed in vessels containing 20 ml of the nitrate/amine solution and incubated at 60 °C for 30 min to see whether the nanocones would grow differently (if at all) on different substrates.

3.3 Results and Discussion

In recent years, a particular challenge to heterogeneous catalysis is how to synthesize highly ordered, 3D branched nano- or micro-structured materials as their unique morphologies, with extremely high surface areas and maximised spatial organization, enhance their optical and electronic properties, which are often greatly desired for industrial applications (18).

In section 3.2.3 a hydrothermal method is described in which nanocones of ZnO can be selectively grown on the inner and outer columnar surfaces of ZnO microstadiums with the use of 1,3-propanediamine, $C_3H_6(NH_2)_2$. SEM images shown in Figures 3.2 and 3.3 display the changes in morphology during the three step method to grow these branched structures: first, hexagonal ZnO microdisks grow on a polymer film on a glass substrate (Figure 3.2a); ethylenediamine is then used to selectively dissolve the centre of these microdisks, forming hollow ZnO microstadiums (Figure 3.2b). In the third and final step, nanocones are grown on the columnar surfaces of the microstadiums in the presence of 1,3-propanediamine, forming so-called 'ZnO decorated microstadiums' (Figure 3.3).

Despite recent work revealing how the ZnO microdisks could be selectively dissolved to form the microstadiums (16), the mechanism by which the nanocones grow on the stadium surfaces still remains a mystery. Each decorated microstadium, after only 1 h of hydrothermal treatment, is densely populated with nanocones that are approximately 400 nm in length and 200 nm in diameter (at the widest part) and which grow perpendicularly to the vertical $(10\bar{1}0)$ and horizontal (0001) walls of the microstadium. It is unclear why the growth of additional ZnO onto the microstadium walls occurs in this way as it would be far more energetically

favourable to simply extend the existing crystal structure, i.e. via the layer by layer deposition of atoms (following classical crystal growth theory).

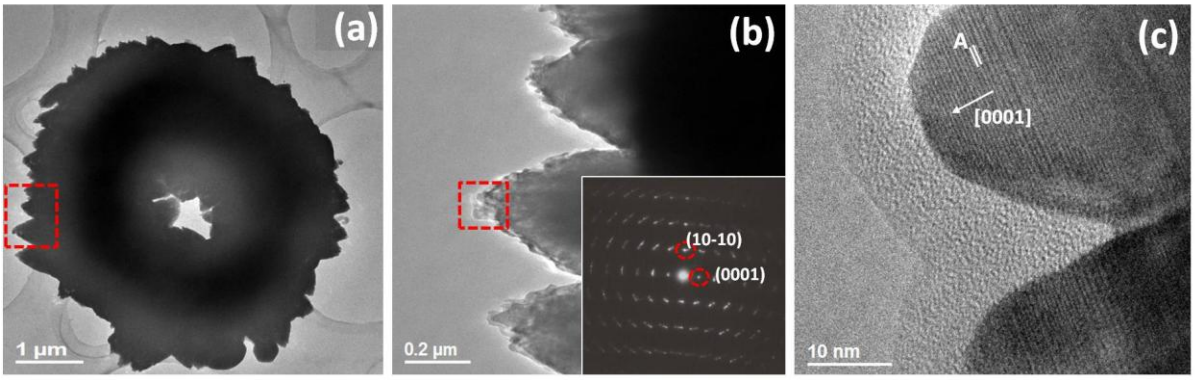

Figure 3.5. TEM and HRTEM analysis of nanocones grown over 40 min. a) Low magnification TEM image of the cross-section of a decorated microstadium. (b) TEM image of nanocones from the area labelled with a square in (a). The inset shows the corresponding SAED pattern viewed along the $[01\bar{1}0]$ direction. (c) HRTEM image of nanorods grown on the outer $(10\bar{1}0)$ wall of the microstadium, from the area marked by the square in image (b). The d-spacing marked A measures d = 5.02 Å which corresponds to the (0001) plane of hexagonal ZnO.

In order to study the microstructure of the nanocones, samples were analysed via TEM and HRTEM, as displayed in Figure 3.5. It was revealed that the nanocones grew perpendicularly to the outer and inner surfaces of the microstadium and were composed of many sharp-tipped nanorods with a diameter of about 20 nm. All of the nanocones analysed revealed that the nanorods were arranged in a single crystal like manner, with crystalline fringes detected which measured d = 5.02 Å (marked A in Figure 3.5c), corresponding to the (0001) plane of hexagonal ZnO with space group symmetry P63mc and unit cell parameters a = 3.249 Å and c = 5.207 Å.

It can be seen from Figure 3.5b and more clearly in Figure 3.5c that the crystal fringes of neighbouring nanorods within each cone overlap perfectly, and have identical orientations as they grow along the [0001] ZnO zone axis. This is further confirmed by the SAED pattern shown in the inset of Figure 3.5b, which was taken over an area containing multiple nanorods from the region indicated by the red square. The single crystal like nature of the SAED pattern, despite covering many nanorods, indicates that they are aligned vertically and are

well oriented. The diffraction spots are diffuse, where the degree of diffusion is dependent on the size of the inserted aperture.

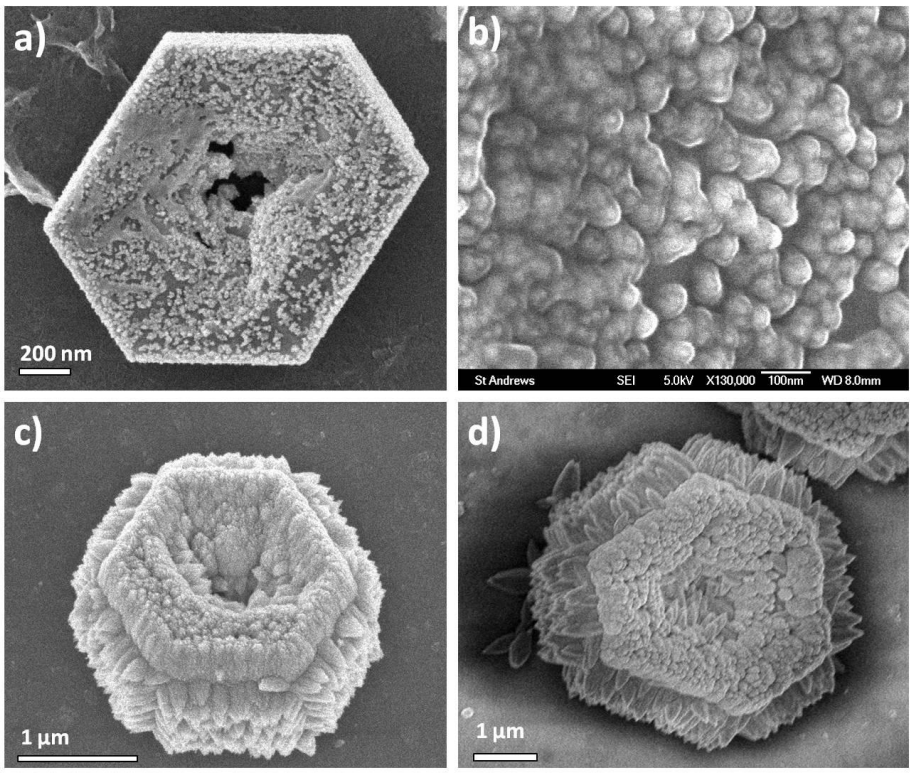

Figure 3.6. SEM analysis of the growth of nanocones on the surface of microstadiums with a reaction time of (a,b) 10 min, (c) 30 min and (d) 1 h.

The growth of the nanocones on the surface of ZnO microstadiums was analysed over time via SEM to determine how their morphology changed as the growth time was increased and whether they grew via the classical, bottom-up, route. Figure 3.6 shows the results of this analysis. It was revealed that the microstadiums are completely covered in nanocones on their outer and inner surfaces by as early as 30 min (Figure 3.6c) with an average length of approximately 300 to 500 nm and that there was no significant growth of the nanocones when the reaction time was increased beyond 30 min (Figure 3.6d).

Figure 3.6a shows a typical SEM image taken from a sample of decorated microstadiums that had been treated with $Zn(NO_3)_2$ and 1,3-propanediamine for only 10 min. At this early growth stage there were no apparent cones on the microstadium surfaces but small aggregates of precursor molecules had started to form, which were approximately 20 to

50 nm in diameter. These aggregates are shown in more detail in Figure 3.6b where evidence can be seen that they have formed within a polymer film across the surface of the ZnO microstadium. This polymer film, made of the 1,3-propanediamine used in the synthesis, alters the surface chemistry of the ZnO microstadium, enabling site-specific nucleation and possibly enhancing the aggregation of precursor material.

TEM and HRTEM analysis of the aggregates at the earliest growth stage of 10 min revealed a polycrystalline microstructure (Figure 3.7). Figure 3.7a shows a typical low magnification TEM image of the aggregates. The arrows in Figure 3.7c and 3.7d indicate the organic polymer film which is coating the particles, enhancing the aggregation as more Zn^{2+} ions are able to chelate with the lone electron pairs of the N atoms in the amino groups of the 1,3-propanediamine. In this way, the polymer can be described as acting as a catalyst for the growth of the nanocones as it speeds up the aggregation process but can constantly be renewed as the Zn^{2+} ions can be exchanged for H^{+} ions from the surrounding aqueous solution.

The HRTEM image displayed in Figure 3.7b contains crystal fringes with a d-spacing measuring 2.75 Å which may correspond to either the $(10\bar{1}0)$ ZnO plane or the (002) plane of the monoclinic zinc nitrate hydroxide hydrate, $Zn_5(NO_3)_2(OH)_8.2H_2O$, phase with space group symmetry C2/m and unit cell parameters a = 19.480 Å, b = 6.238 Å, c = 5.517 Å and β = 93.28°. The latter phase was also observed to have been present at the earliest growth stage of the ZnO microdisks (16) which grew via a non-classical route through the formation of $Zn_5(NO_3)_2(OH)_8.2H_2O$ precursor aggregates which then underwent recrystallization to form a single crystal hexagonal shell encasing a disordered, polycrystalline core (i.e. following the "reversed crystal growth" route) (24). It is, therefore, probable that a similar process is occurring in the present case. Unfortunately, since the microstadiums are grown on a glass substrate and the yield is so low, there was insufficient sample to be able to scrape them off the substrate and perform PXRD analysis to provide further evidence of the $Zn_5(NO_3)_2(OH)_8.2H_2O$ phase.

The polycrystalline nature of the particles observed at the early stage of 10 min is in stark contrast to that observed at a growth time of 40 min (Figure 3.5), where the cones had become completely single crystalline. A phase transformation must, therefore, occur during which the many nanocrystallites of ZnO or $Zn_5(NO_3)_2(OH)_8.2H_2O$ in the precursor

polycrystalline aggregates (at the 10 min stage) join together to form the single crystal ZnO cones.

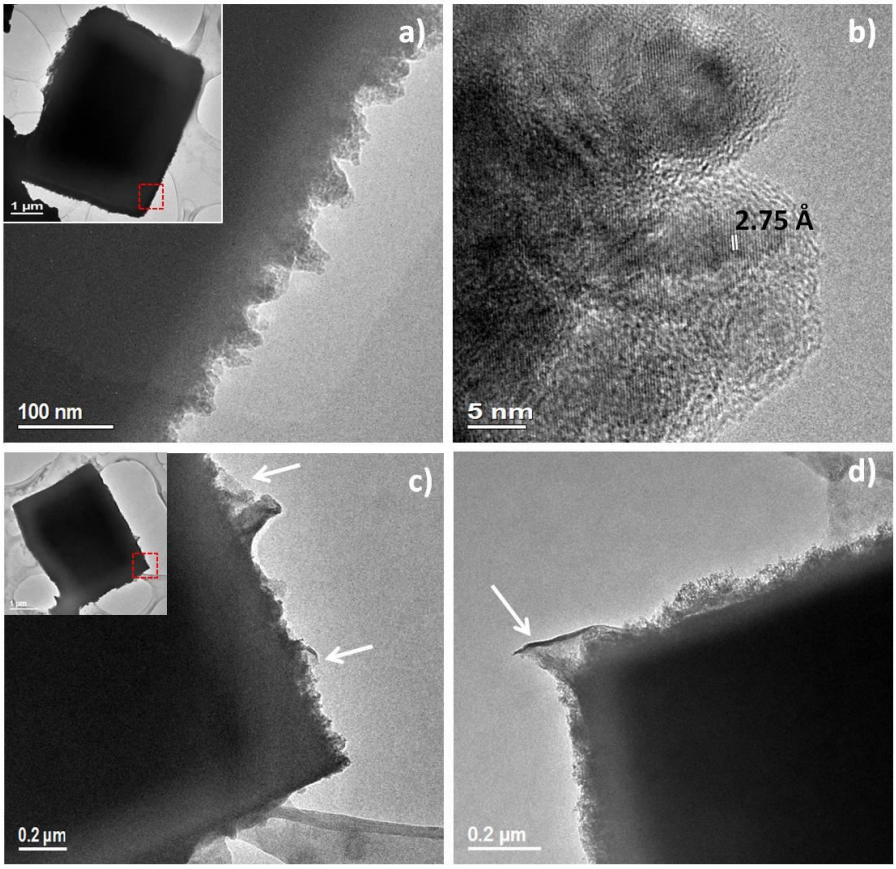

Figure 3.7. TEM and HRTEM images of early stage nanocones on the surface of a microstadium particle which were generated after a reaction time of 10 min. (a) TEM image of aggregates which form on the surface of the ZnO microstadiums as a precursor to the growth of ZnO nanocones. Low magnification TEM image of the microstadium is shown inset. (b) HRTEM image taken from the area shown by the square in image (a), revealing a polycrystalline microstructure. The d-spacing labelled in the image measures 2.75 Å which corresponds to either the $(10\bar{1}0)$ plane of ZnO or the (002) plane of $Zn_5(NO_3)_2(OH)_8.2H_2O$. (c) and (d) TEM images of other 10 min nanocone samples showing evidence of the polymer film coating the sample surface (indicated by the white arrows).

This evidence supports the theory of a non-classical growth mechanism as it is apparent that, initially, there are polycrystalline aggregates made up of many nanocrystallites which join together and undergo recrystallization to form many well-aligned single crystalline ZnO nanorods. This is completely opposed to the classical theory where precursor ions are deposited layer by layer onto a single crystal, starting from a single nucleation point.

The growth of both vertical and horizontal nanocones can be observed on the inner walls of the microstadiums (as can be seen in Figure 3.6c and 3.6d), implying that there are not only vertical $(10\bar{1}0)$ planes, but also horizontal (0001) planes inside the microstadiums, i.e. 'nanosteps'. High resolution SEM (HRSEM) analysis was performed on the inner walls of the microstadiums and revealed that these nanosteps are indeed present (Figure 3.8).

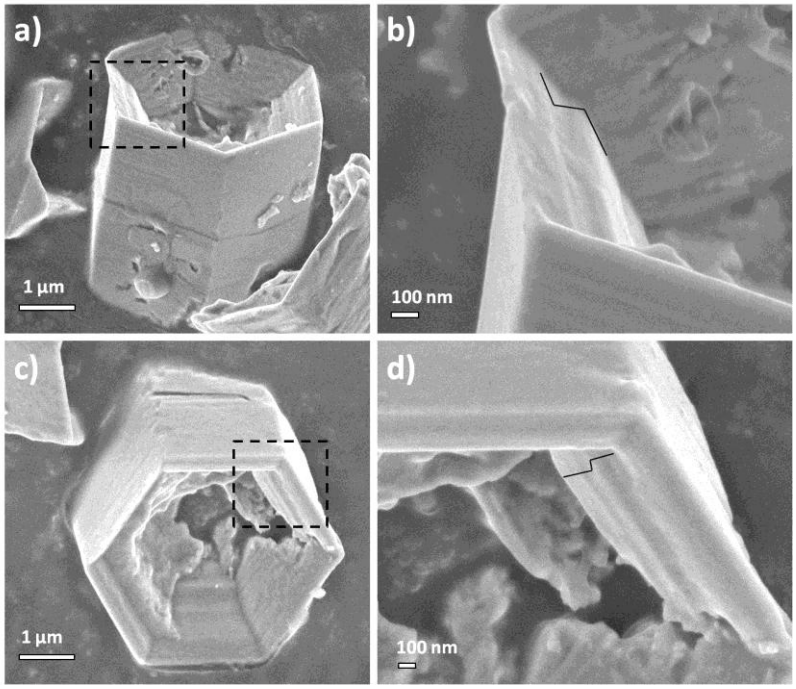

Figure 3.8. a) and c) SEM images of ZnO microstadiums. b) and d) the corresponding higher magnification SEM images of the inner walls of the microstadiums with black lines added to highlight the presence of nanosteps.

In order to determine whether the growth of the ZnO nanocones was unique to the microstadium surfaces (i.e. whether the microstadiums have a unique surface structure that can give rise to this ordered secondary growth), the 1 h hydrothermal treatment used to synthesize the cones was also performed on other substrates.

As shown in Figure 3.9, the nanocones grew abundantly on each substrate: a glass slide, ZnO microstadiums and ZnO microdisks, and so it seems their growth is not solely dependent on the particular surface chemistry of the microstadium walls. Figure 3.9a shows that although the nanocones grew on a glass slide when no ZnO microstadiums were present, they did not grow directly on the glass. Rather, they grew perpendicularly out from a centre

which was a small, cone-like ZnO aggregate. This can be seen more clearly in the inset. Figure 3.9c and 3.9d display the two typical morphologies observed when nanocones were grown on ZnO microdisks. It can be seen that, whilst the cones always grew abundantly on the columnar $(10\bar{1}0)$ surfaces, they either grew abundantly (Figure 3.9c) or did not grow at all (Figure 3.9d) on the top (0001) surface. From the examples imaged, these differently covered surfaces existed in a 1:1 ratio to each other. This is likely to be due to the polar nature of the (0001) and $(000\bar{1})$ surfaces of the ZnO wurtzite structure, which is made up of alternating planes of Zn^{2+} and O^{2-} ions along the c-axis.

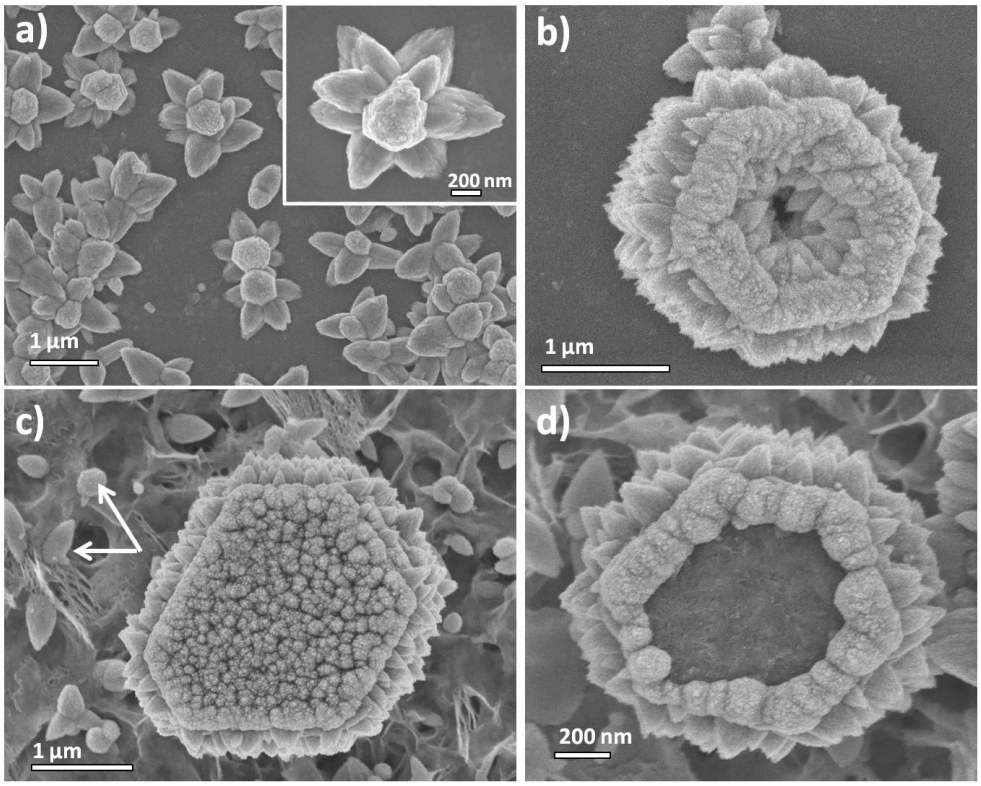

Figure 3.9. SEM images showing growth of ZnO nanocones after 1 h on a) a plain glass slide, b) ZnO microstadiums and c) and d) on ZnO microdisks. The arrows in c) indicate the singular nanocones which grew on the polymer layer covering the glass substrate.

As the wurtzite structure does not have a centre of inversion, the terminating surface normal to the c-axis can be one of two polar planes: the (0001)-Zn surface with the Zn^{2+} cations in the outermost plane, or the $(000\bar{1})$-O surface with the O^{2-} anions in the outermost plane (25). To maintain a stable structure, polar metal oxide surfaces generally must exhibit

massive surface reconstructions to stabilise them, but these (0001)-Zn and $(000\bar{1})$-O surfaces have been shown to be exceptions to this rule: they remain atomically flat and stable (26). The two different terminating surfaces have different physical and chemical properties and so studies have shown that they have different surface chemistry, with absorption being generally more favourable on the (0001)-Zn surface (27). It is clear that in the present work the growth of the nanocones occurs on only one of these terminating surfaces.

1,3-propanediame has been observed to form a polymer film on a variety of metal substrates (28) and also on fluorine-doped tin oxide (FTO) electrodes where the amino groups on the polymer film present good chelating properties towards Cu^{2+} (due to the lone electron pair on the N atoms) (29). This would explain why the nanocones grew on only one of the polar (0001) surfaces of the ZnO microdisks as the polymer film may form on only one of the possible terminating surfaces. Most likely, the film will form on the positively charged (0001)-Zn surface due to this ability to chelate with the Zn^{2+} ions. The presence of a polymer film which would chelate easily with Zn^{2+} ions would also enhance the aggregation of precursor ions, explaining the formation of the small aggregates observed on the microstadium surfaces at the earliest growth stage (Figure 3.6a and 3.6b).

Summary of the Growth Mechanism of ZnO Decorated Microstadiums

With the information gathered thus far it is now possible to propose a more accurate, non-classical crystal growth mechanism for the ZnO nanocones on the surfaces of the ZnO decorated microstadiums (Figure 3.10).

Initially, a polymeric layer of 1,3-propanediame coats the horizontal (0001) and vertical $(10\bar{1}0)$ faces of the ZnO microstadium (Figure 3.10a). This polymer layer then acts as a catalyst for the formation of precursor aggregates after just 10 min of incubation (Figure 3.10b) as Zn^{2+} ions are able to chelate with the polar amino groups in the polymer chain due to the lone electron pair on the N atom. These aggregates contain many nanocrystallites (indicated in dark grey in Figure 3.10b) of ZnO, $Zn_5(NO_3)_2(OH)_8.2H_2O$ or both as shown in the HRTEM image displayed in Figure 3.7. As the growth time is extended, the nanocrystallites in the outer surface of the aggregates grow larger, join together and recrystallize to form many well aligned ZnO nanorods (Figure 3.10c), giving rise to sharp tipped nanocones (Figure 3.10d).

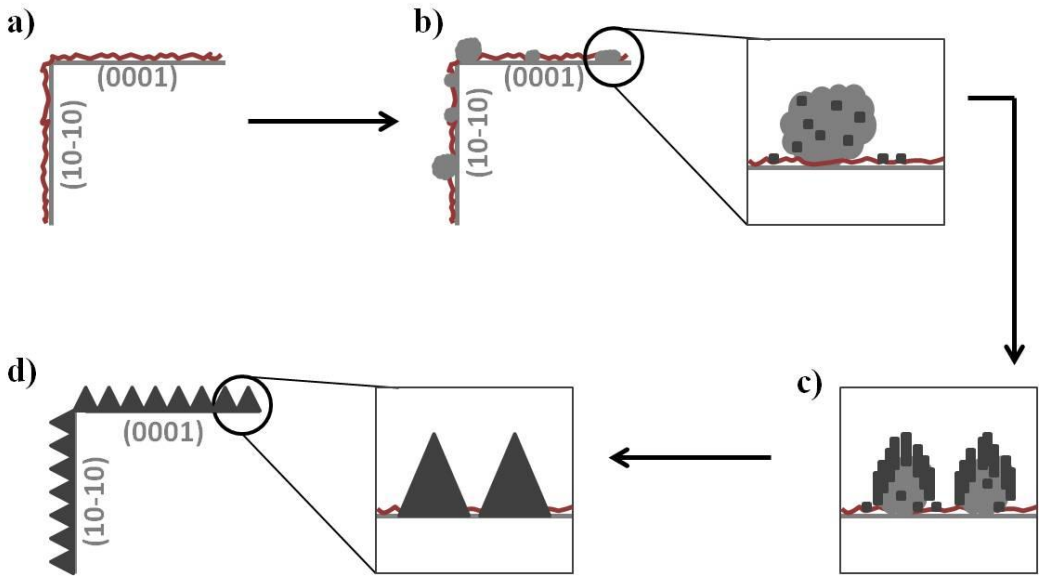

Figure 3.10. Illustration of the proposed growth mechanism for ZnO nanocones on the surfaces of ZnO microstadiums. a) First, a layer of polymer, 1,3-propanediamine (shown in red), coats the outer vertical $(10\bar{1}0)$ and horizontal (0001) surfaces of the microstadium. b) Precursor ions, attracted by the polar amine groups, gather in the polymer layer and join together forming many disordered aggregates containing many nanocrystallites of ZnO or $Zn_5(NO_3)_2(OH)_8.2H_2O$. c) The nanocrystallites at the top of the aggregates (not connected to the polymer) recrystallize into many well aligned ZnO nanorods as more precursor ions join the base of the growing aggregates. d) Finally, the crystallisation extends through the whole aggregate, resulting in many well aligned ZnO nanorods that appear as nanocones on the microstadium surfaces.

ZnO microdisks, which also had aggregation on a polymer film as the first step in the growth process, were proven to grow from the base (in contact with the polymer film) rather than the top (exposed to the reactant solution). This was a result of the polymer film continuing to act as a catalyst for growth as more precursor ions could join the growing crystals through the polymer layer (16). In the case of the nanocones in the present work, the same argument can be made. The lower portion of the aggregate, which is in contact with the polymer film, will be the last part to recrystallize (Figure 3.10c) as more precursor ions continue to join the growing aggregate through the polymer layer.

Eventually, the entire aggregate undergoes recrystallization, resulting in ZnO nanocones, composed of many well-aligned single crystal nanorods, coating the inner and outer surfaces of the microstadiums (Figure 3.10d).

3.4 Conclusions

In conclusion, this work has shown that the nanocones on the inner and outer walls of the microstadium surfaces in 'ZnO decorated microstadiums' grow via a non-classical route of aggregation of precursor ions into particles made up of many nanocrystallites which then join together and undergo recrystallization, forming single crystal like ZnO nanocones.

It was previously unclear why the nanocones grew at all, however, as secondary growth of a branched structure is unfavourable compared to simply extending the crystal structure of the ZnO substrate (microstadium or microdisk) via classical growth. HRSEM and HRTEM analysis has shown that the secondary growth of the cones on ZnO crystals is due to the presence of a 1,3-propanediamine polymer film which forms on the stadium/disk surfaces, enhancing the aggregation of precursor ions due to their attraction to the lone electron pairs on the amino groups. This process prevents growth via the classical route.

Previous reports have shown that in an aqueous-phase synthesis, the presence of an organic structure directing agent can alter the specific morphology and microstructure of a material if it is selectively adsorbed onto a crystal surface. This adsorption alters the surface chemistry of the crystal which can lead to site-specific nucleation and, therefore, secondary growth (19). The size and shape of ZnO nanocrystals have previously been successfully controlled by the addition of ammonia, citrate acid and poly(vinylalcohol) into the hydrothermal synthesis (20). As mentioned previously, both hollow and dendritic structures of ZnO are of high interest in industry as their high surface areas maximise the desired properties of ZnO for its many applications.

Achieving this clear understanding of how secondary growth can occur on hollow ZnO structures is a very important step as these structures combine the desired high surface areas of both hollow and of dendritic structures and so would be potentially very useful as oriented semiconducting nanomaterials (23, 30) and are currently being examined for their use as photocatalysts by the Tian group at the University of Arkansas and by other members of the Zhou group at the University of St Andrews. Knowledge of their exact growth mechanism will allow us to further fine-tune their morphology, thereby tailoring their properties for future applications.

References

1. (a) Lao, J. Y.; Huang, J. Y.; Wang, D. Z.; Ren, Z. F. *Nano Lett*. **2003**, *3*, 235. (b) Hu, P.; Liu, Y. Q.; Wang, X. B.; Fu, L.; Zhu, D. B. *Chem. Commun*. **2003**, 1304. (c) Park, W. I.; Yi, G.-C. *Adv. Mater*. **2004**, *16*, 87. (d) Kong, X. Y.; Ding, Y.; Yang, R.; Wang, Z. L. *Science*. **2004**, *303*, 1348. (e) Park, J.-H.; Choi, H.-J.; Choi, Y.-J.; Sohn, S.-H.; Park, J.-G. *J. Mater. Chem.* **2004**, *14*, 35.
2. a) Ding, Y.; Gao, P.; Xin, X.; Wang, Z. L. *Angew. Chem Inter. Edi.* **2004**, *116*, 5350. (b) Jeong, J. S.; Lee, J. Y.; Cho, J. H.; Suh, H. J.; Lee, C. *J. Chem. Mater.* **2005**, *17*, 2752
3. (a) King, D. S.; Nix, R. M. *J. Catal*. **1996**, *160*, 76. (b) Trivikrama, G. S. R.; Tarakarama, D. R. *Sensors Actuators B*. **1999**, *55*, 166.
4. (a) Minami, T. *Mater. Res. Soc. Bull.* **2000**, *25*, 38. (b) Agarwal, G.; Speyer, R. F. *J. Electrochem. Soc.* **1998**, *145*, 2920. (c) Sousa, V. C.; Segadaes, A. M.; Morelli, M. R.; Kiminami, R. H. G. A. *Int. J. Inorg. Chem.* **1999**, *1*, 235. (d) Quaranta, F.; Valentini, A.; Rizzi, F. R.; Casamassima, G. *J. Appl. Phys*. **1993**, *74*, 244.
5. (a) Schoenmakers, G. H.; Vanmaekelbergh, D.; Kelly, J. J. *J. Phys. Chem. B*. **1996**, *100*, 3215. (b) Bagnall, D. M.; Chen, Y. F.; Zhu, Z.; Yao, T.; Koyama, S.; Shen, M. Y.; Goto, T. *Appl. Phys. Lett.* **1997**, *70*, 2230. (c) Wada, T.; Kikuta, S.; Kiba, M.; Kiyozumi, K.; Shimojo, T.; Kakehi, M. *J. Cryst. Growth.* **1982**, *59*, 363. (d) Klingshirn, C.; Kalt, H.; Renner, R.; Fodorra, F. *J. Cryst. Growth*. **1985**, *72*, 304.
6. (a) Zhong, J.; Kitai, A. H.; Mascher, P.; Puff, W. *J. Electrochem Soc.* **1993**, *140*, 3644. (b) Keis, K.; Vayssieres, L.; Lindquist, S.-E.; Hagfeldt, A. *J. Electrochem. Soc*. **2001**, *148*, 155.
7. Wang, Z. L. *J. Phys. Condens. Matter*, **2004**, *16*, 829.
8. Niskanen, M.; Kuisma, M.; Cramariuc, O.; Golovanov, V.; Hukka, T. I.; Tkachenko, N.; Rantala, T. T. *Phys. Chem. Chem. Phys.*, **2013**, *15*, 17408
9. (a) Modeshia, D. R.; Dunnill, C. W.; Suzuki, Y.; Al-Ghamdi, A. A.; El-Mossalamy, E. H.; Obaid, A. Y.; Basahel, S. N.; Alyoubi, A. O.; Parkin, I. P. *Chem. Vap. Deposition*, **2012**, *18*, 282. (b) Agouram, S.; Bushiri, M. J.; Montenegro, D. N.; Reig, C.; Martinez-Tomas, M. C.; Munoz-Sanjose, V. *J. Nanosci. Nanotechnol.*, **2012**, *12*, 6792.
10. Vayssieres, L.; Keis, K.; Hagfeldt, A.; Lindquist, S.-E. *J. Chem.Mater.*, **2001**, *13*, 4395.

11. Zeng, H. B.; Xu, X. J.; Bando, Y.; Gautam, U. K.; Zhai, T. Y.; Fang, X. S.; Liu, B. D.; Golberg, D. *Adv. Funct. Mater.*, **2009**, *19*, 3165.
12. Vayssieres, L.; Keis, K.; Lindquist, S.-E.; Hagfeldt, A. *J. Phys. Chem. B.*, **2001**, *105*, 3350.
13. (a) Chen, Q.; Zhou, W. Z.; Du, G. H.; Peng, L. M. *Adv. Mater*. **2002**, *17*, 1208. (b) Zhang, S.; Peng, L. M.; Chen, Q.; Du, G. H.; Dawson, G.; Zhou, W. Z. *Phys. Rev. Lett*., **2003**, *91*, 256103. (c) Kobayashi, Y.; Hata, H.; Salama, M.; Mallouk, T. E. *Nano Lett*., **2007**, *7*, 2142. (d) Du, G. H.; Chen, Q.; Yu, Y.; Zhang, S.; Zhou, W. Z.; Peng, L. M. *J. Mater. Chem.*, **2004**, *14*, 1437.
14. Nanai, L.; George, T. F. *J. Mater. Res.*, **1997**, *12*, 283.
15. (a) Hoyer, P. *Langmuir*, **1996**, *12*, 1411. (b) Cepak, V. M.; Hulteen, J. C.; Che, G.; Jirage, K. B.; Lakshmi, B. B.; Fisher, E. R.; Martin, C. R. *Chem. Mater*. **1997**, *9*, 1065.
16. Self, K.; Zhou, H.; Greer, H. F.; Tian, Z. R.; Zhou, W. *Chem. Commun.*, **2013**, *49*, 5411.
17. Chen, X. Y.; Qiao, M. H.; Xie, S. H.; Fan, K. N.; Zhou, W. Z; He, H. Y. *J. Am. Chem. Soc.*, **2007**, *129*, 13305.
18. (a) Yan, H. Q.; He, R. R.; Johnson, J.; Law, M.; Saykally, R. J.; Yang, P. D. *J. Am. Chem. Soc*. **2003**, *125*, 4728. (b) Xu, C. X.; Sun, X. W.; Chen, B. J.; Dong, Z. L.; Yu, M. B.; Zhang, X. H.; Chua, S. *J. Nanotechnology*, **2005**, *16*, 70. (c) Dick, K. A.; Deppert, K.; Larsson, M. W.; Mårtensson, T.; Seifert, W.; Wallenberg, L. R.; Samuelson, L. *Nat. Mater*., **2004**, 3, 380. (d) Zhang, T. R.; Dong, W. J.; Keeter-Brewer, M.; Konar, S.; Njabon, R. N.; Tian, Z. R. *J. Am. Chem. Soc.* **2006**, *128*, 10960.
19. Kuo, C. L.; Kuo, T. J.; Huang, M. H. *J. Phys. Chem. B.*, **2005**, *109*, 20115.
20. Zhang, H.; Yang, D. R.; Li, D. S.; Ma, X. Y.; Li, S.Z.; Que, D. L. *Cryst. Growth Des.*, **2005**, *5*, 547.
21. Zhao, F. H.; Li, X. Y.; Zheng, J. G.; Yang, X. F.; Zhao, F. L.; Wong, K. S.; Wang, J.; Lin, W. J.; Wu, M. M.; Su, Q. *Chem. Mater.*, **2008**, *20*, 1197.
22. (a) Yu, Q.; Fu, W.; Yu, C.; Yang, H.; Wei, R.; Li, M.; Liu, S.; Sui, Y.; Liu, Z.; Yuan, M.; Zou, G. *J. Phys. Chem. C*, **2007**, *111*, 17521. (b) Zhao, F.; Lin, W.; Wu, M.; Xu, N.; Yang, X.; Tian, Z. R.; Su, Q. *Inorg. Chem.*, **2006**, *45*, 3256.

23. (a) Zhang, T.; Dong, W.; Keeter-Brewer, M.; Konar, S.; Njabon, R. N.; Tian, Z. R. *J. Am. Chem. Soc.*, **2006**, *128*, 10960. (b) Sounart, T. L.; Liu, J.; Voigt, J. A.; Hsu, J. W. P.; Spoerke, E. D.; Tian, Z. R.; Jiang, Y. *Adv. Funct. Mater*., **2006**, *16*, 335.
24. Chen, X. Y.; Qiao, M. H.; Xie, S. H.; Fan, K. N.; Zhou, W. Z; He, H. Y. *J. Am. Chem. Soc.*, **2007**, *129*, 13305.
25. Wander, A.; Schedin, F.; Steadman, P.; Norris, A.; McGrath, R.; Turner, T. S.; Thornton, G.; Harrison, N. M. *Phys. Rev. Lett.*, **2001**, *86*, 3811.
26. Meyer, B.; Marx, D. *Phys. Rev. B*, **2003**, *67*, 035403.
27. Dulub, O.; Boatner, L. A.; Diebold, U. *Surf. Sci.*, **2002**, *519*, 201.
28. (a) Gengenbach, T. R.; Griesser, H. J. J. *Polym. Sci., Part A: Polym. Chem.*, **1999**, *37*, 2191. (b) Lakard, B.; Herlem, G.; Lakard, S.; Guyetant, R.; Fahys, B. *Polymer*, **2005**, *46*, 12233.
29. Lakard, S. P.; Herlem, G.; Lakard, B.; Herlem, M.; Gharbi, T.; Fahys, B. *J. Electrochem. Soc.*, **2004**, *151*, 245.
30. (a) Gao, P. X.; Wang, Z. L. *Appl. Phys. Lett.*, **2004**, *84*, 2883. (b) Dick, K. A.; Deppert, K.; Larsson, M. W.; Mårtensson, T.; Seifert, W.; Wallenberg, L. R.; Samuelson, L. *Nat. Mater.*, **2004**, *3*, 380. (c) May, S. J.; Zheng, J. G.; Wessels, B. W.; Lauhon, L. J. *Adv. Mater.*, **2005**, *17*, 598.

Chapter 4. Non-Classical Crystal Growth of Cuprous Oxide Structures

4.1 Introduction

Cuprous oxide, Cu_2O, is a semiconductor material that has a cubic lattice structure, a direct band gap of 2.137 eV (1) and which typically exhibits p-type semiconductor characteristics due to the presence of Cu vacancies (2). Due to its unique and interesting magnetic and optical properties, cuprous oxide has been widely studied as a promising material with potential applications in a huge range of fields such as catalysis (3), gas sensing (4) and the conversion of solar energy into chemical or electrical energy (5) as well as having been at the centre of research into the Bose-Einstein condensation of excitons (6).

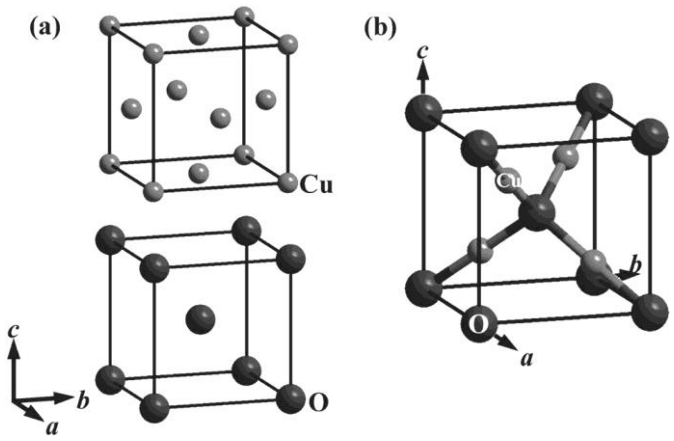

Figure 4.1. Crystal structure of cuprous oxide. The smaller, light grey spheres represent Cu and the larger, darker grey spheres represent O. a) The individual structural characteristics of Cu and O within the Cu_2O lattice. b) The Cu_2O unit cell. Adapted from Ref. 14 with permission from The Royal Society of Chemistry.

Cuprous oxide crystallises into the cuprite structure, with $Pn\bar{3}m$ space group symmetry. In this structure, each Cu is connected to two neighbouring O ions and each O ion is surrounded by a tetrahedral of Cu (Figure 4.1). The Cu_2O lattice is composed of the interpenetrating Cu lattice, which adopts face centered cubic (fcc) packing, and the O lattice, which adopts body centered cubic (bcc) packing (7) as displayed in Figure 4.1a.

Cu_2O has been reported in the literature to exhibit a wide variety of possible morphologies such as thin films (8, 9), nanorod arrays (10), nanospheres or nanocubes (11, 12) and even hollow crystals (13). Since the suitability of Cu_2O for its various applications has been shown to be so highly dependent on its morphology and microstructure (14), an array of different and often complicated techniques have been utilised to attempt to control the shapes and sizes of cuprous oxide crystals. These have included electrochemical deposition (15), high pressure sputtering (16), sonochemical methods (17) and many other techniques (18, 19) but the control of Cu_2O morphologies synthesized via more facile, hydrothermal routes has rarely been reported.

More recently, there has been interest in the highly symmetric, so-called "8-pod branching growth" (20-22) of Cu_2O crystals (Figure 4.2) as the high degree of branching in such structures results in a much higher surface area than that of the more typical cubic or octahedral Cu_2O crystals and may, therefore, increase the efficiencies of Cu_2O crystals for their various applications.

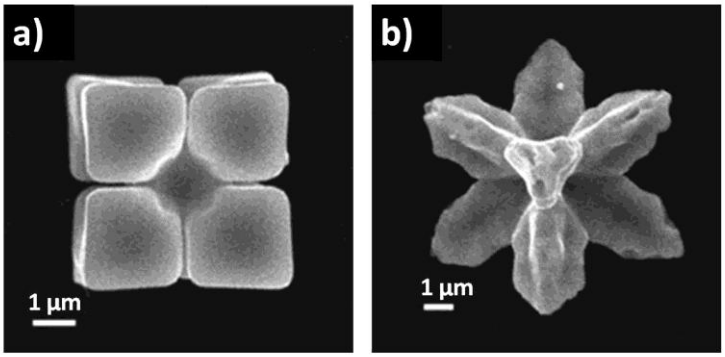

Figure 4.2. SEM images displaying the recently reported 8-pod branching growth of Cu_2O. Adapted from Ref. 20 with permission from Elsevier Ltd.

In the present work, a simple hydrothermal synthesis is presented to form Cu_2O crystals with the 8-branched morphology which then undergo a phase transformation to a cubic shape. The work will mainly focus on the early stage growth of the branches, studying the crystal formation, with some analysis into the later growth stages, and a new mechanism will be proposed for their formation. These studies uncover further evidence that the classical

crystal growth mechanisms, established over a century ago, can often not be applied to the formation of highly symmetric, branched structures.

4.2 Synthesis

The synthesis used in this project was adapted from a method reported by Guo *et al.* (11) to generate "Cu_2O crossed nanocubes". There were several steps required in order to synthesise the desired Cu_2O 8-branched structure. Firstly, 0.17 g copper (II) chloride, $CuCl_2.2H_2O$ (Fisher Scientific), was dissolved in 5 ml distilled water and, separately, 0.2 g polyvinylpyrrolidone, $(C_6H_9NO)_n$ (average molecular weight ~ 55,000, Sigma Aldrich), was dissolved into 5 ml distilled water. These two aqueous solutions were then added to 55 ml distilled water forming a pale blue solution that was then stirred for 30 min with a magnetic stir bar.

In the next step, 0.69 g potassium carbonate, K_2CO_3 (Fisher Scientific), and 0.64 g monosodium citrate, $NaC_6H_7O_7$ (Sigma Aldrich), were dissolved by stirring in 10 ml distilled water. This solution was then added to the light blue $CuCl_2$/PVP aqueous solution from the first stage, which instantly turned to a much darker blue colour. Next, 0.9 g D-glucose, $C_6H_{12}O_6$ (Fisher Scientific), was dissolved in 5 ml distilled water and then this was added to the dark blue solution.

The final solution was stirred magnetically for a further 10 min to ensure homogeneity and then 35 ml of it was transferred to a 50 ml Teflon-lined autoclave which was sealed and heated in an oven at 100 °C for 1.5 h. The resulting precipitate was retrieved via centrifugation and washed with ethanol and distilled water before being dried overnight in an oven at 40 °C.

This experiment was repeated with different incubation times of 2, 4, 13, 24 and 48 h as well as a much longer time of 20 days. Experiments were also performed with the glucose removed from the synthesis or with half the concentration of $CuCl_2.2H_2O$ to observe how these parameters would alter the crystal growth. To prepare samples for TGA analysis, approximately 20 mg of the dry powders was heated in air in a furnace at a ramp rate of 2 °C per min from room temperature to 600 °C. They were then held at 600 °C for 2 h before being cooled back room temperature at a ramp rate of -5 °C per min.

4.3 Results and Discussion

Cuprous oxide, Cu_2O, crystals synthesised over a range of growth times were first analysed via SEM (Figure 4.3). This revealed variations in the morphology of the crystals which started as 8-branched particles at the earliest growth time of 1.5 h (Figure 4.3a), with the branches appearing to grow along the <111> directions of the cubic Cu_2O unit cell. By 2 h, the dominant growth direction had become <100>, i.e. the branches had grown thicker, as the morphology appeared to move towards a more cubic shape (Figure 4.3b). The space between the branches became smaller and smaller over time until all eight branches were connected (Figure 4.3c) and then the space between them filled out, with increased growth on the {100} faces until finally, after 13 h, the Cu_2O crystals appeared as perfect cubes (Figure 4.3d). It should be noted that the crystals were never of uniform size at any growth stage and some reached the cubic morphology faster than others but the SEM images in Figure 4.3 represent the typical size and shape of crystals at each stage and by 13 h all crystals were cubic in appearance.

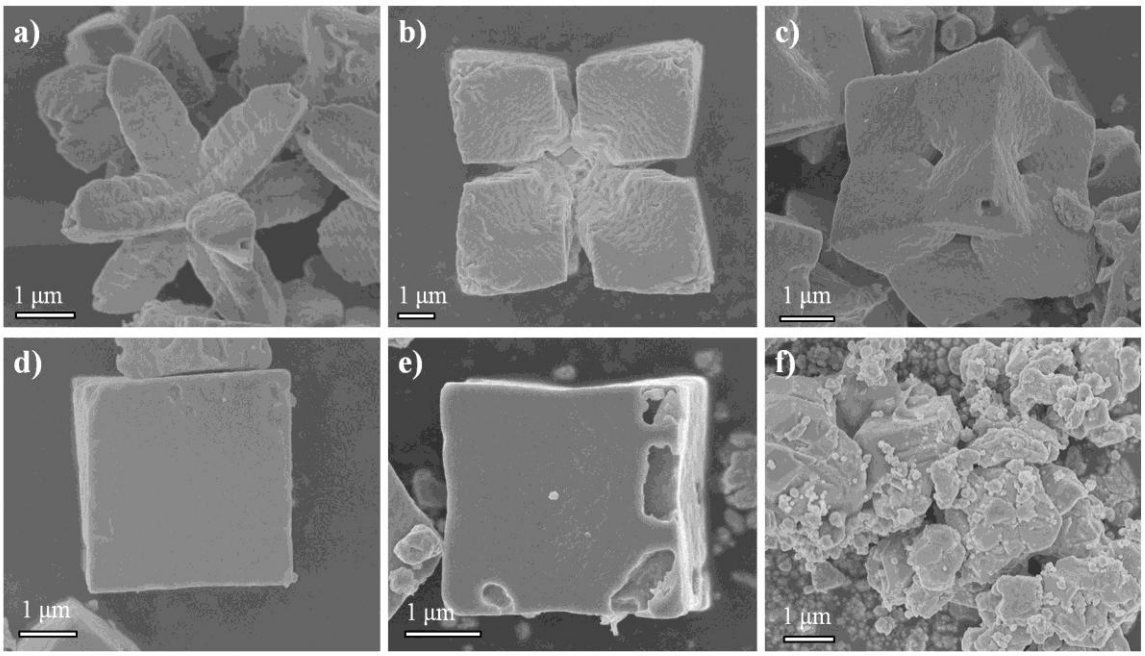

Figure 4.3. SEM images displaying the typical morphologies observed of specimens grown over different times of a) 1.5 h, b) 2 h, c) 4 h, d) 13 h, e) 24 h and f) 20 days.

As the growth time was extended to 24 h (Figure 4.3e) the start of another change in morphology could be observed. The cubic crystals began to break apart or disintegrate over time until, at the much longer growth time of 20 days, there were no crystals found with a uniform, distinguishable morphology, cubic or otherwise (Figure 4.3f).

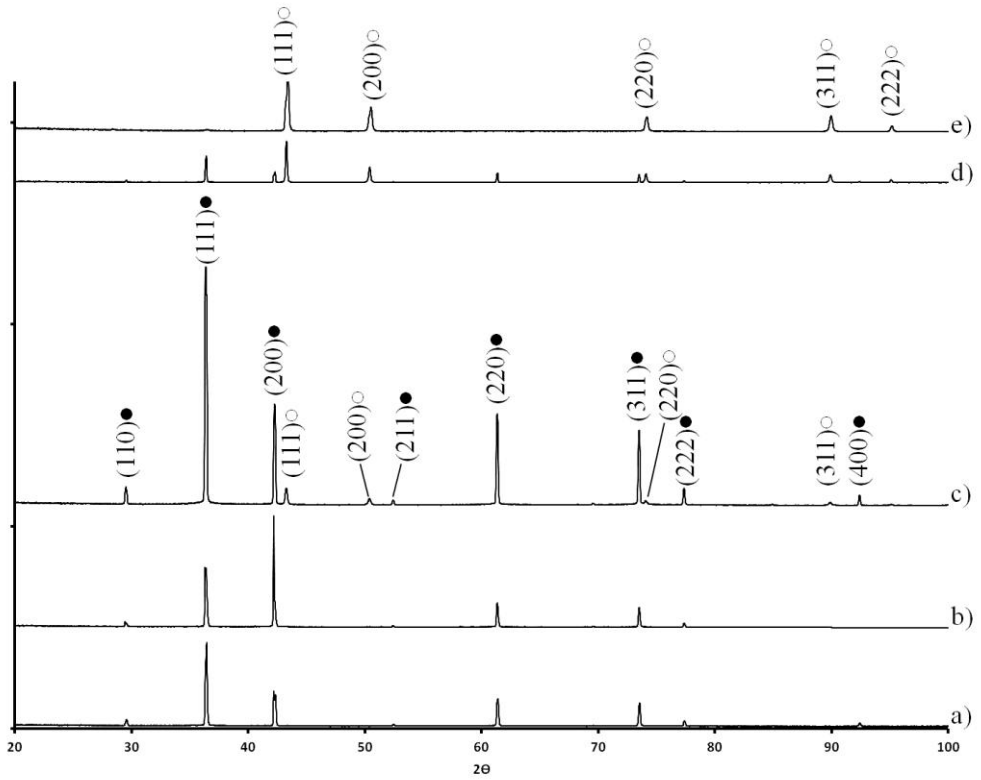

Figure 4.4. PXRD pattern of samples grown over a) 2 h, b) 4 h, c) 13 h, d) 48 h, and e) 20 days. The peaks marked ● have been indexed to cubic Cu_2O and those marked ○ are indexed to cubic Cu.

In order to study these interesting morphological changes in more detail, PXRD analysis was also carried out on the samples over a range of growth times. As shown in Figure 4.4, crystalline Cu_2O had formed very rapidly and so could be observed from the earliest growth time tested of 2 h onwards. The yield from the 1.5 h experiment was so low that there was insufficient sample for PXRD testing. The peaks in Figure 4.4 marked ● have been indexed to the cubic Cu_2O phase with unit cell parameter a = 4.2797 Å and space group $Pn\bar{3}m$. The PXRD pattern from the sample grown over 13 h (Figure 4.4c) was the earliest one to reveal low intensity peaks that could not be indexed to Cu_2O but which actually represent

the cubic Cu metal phase. These peaks have been marked ○ and are indexed to cubic Cu with unit cell parameter a = 3.6200 Å and space group $Fm\bar{3}m$. There is a clear phase transition from Cu_2O to Cu at long growth times as the Cu peaks gradually grow in intensity and the Cu_2O peaks decrease in intensity until they are no longer detected at all in the 20 day sample (Figure 4.4e).

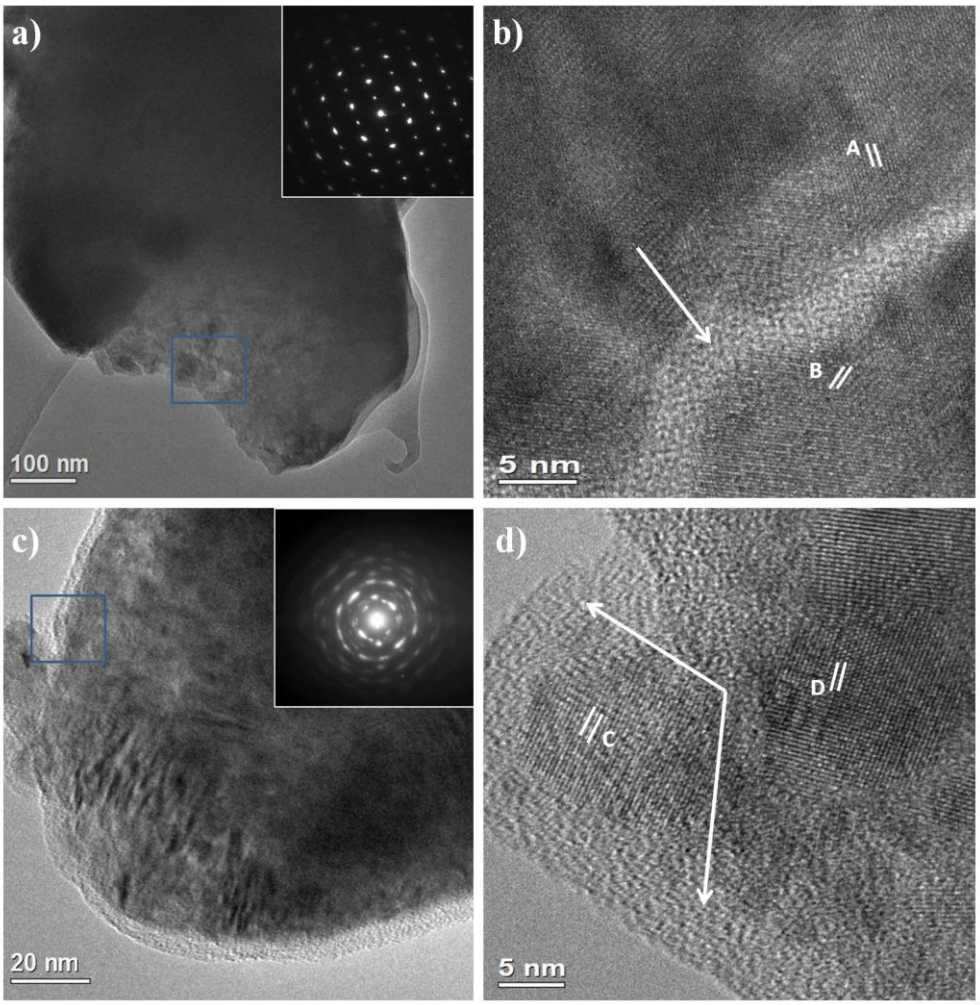

Figure 4.5. TEM analysis of 2 h sample. a) Low magnification TEM image with corresponding diffraction pattern inset, showing a single-crystal like region. b) HRTEM image from the area marked with a blue square in a). c) Low magnification TEM image with corresponding diffraction pattern inset, showing region of polycrystalline material. d) HRTEM image from the area marked with a blue square in c). The d-spacings marked A, B, C and D measure 2.44 Å, 2.12 Å, 1.73 Å and 1.14 Å respectively. All of the d-spacings could be indexed to cubic Cu_2O planes: A corresponds to the (111) plane, B to the (200) plane, C to the (211) plane and D to the (321) plane. The arrows in b) and d) indicate the amorphous, organic component present.

The morphological change from an 8-branched to a cubic shape and, therefore, a relative increase in growth rate along the <100> directions explains the relative increase in intensity of the (200) peak in comparison to the (111) peak in the PXRD pattern of the 4 h sample (Figure 4.4b) as this is the point at which the morphology starts to appear cubic when observed via SEM.

Initially, this report will focus on the early stage growth of the 8-branched Cu_2O structures as their high surface areas and interesting optical and magnetic properties make them of great interest in industry. The transition to Cu will be discussed later on in the chapter.

For a more detailed analysis of the microstructure of the early stage 2 h sample, TEM and HRTEM images were recorded along with the corresponding diffraction patterns. In Figure 4.5a, a low magnification TEM image of an area of the 2 h sample is displayed with the corresponding diffraction pattern inset. The clear, separate spots in the diffraction pattern reflect an area of ordered, single-crystal like material. The higher resolution image shown in Figure 4.5b (which corresponds to the area of the image in Figure 4.5a marked with the blue square) shows many regions of crystalline material that appear perfectly aligned (hence the single-crystal-like diffraction pattern) despite being separated by some amorphous organic matter (the regions of organic observed are indicated by the white arrows in Figure 4.5b and 4.5d). The d-spacing labelled A measures 2.44 Å and corresponds to the (111) plane of cubic Cu_2O. The d-spacing labelled B measures 2.12 Å and corresponds to the (200) Cu_2O plane.

In contrast, when a diffraction pattern was taken from another fragment of a particle from the same 2 h sample, polycrystalline rings were observed rather than the separate single crystal spots (as shown in the inset of Figure 4.5c). In the corresponding HRTEM image (Figure 4.5d, which was taken from the area marked with a blue square in Figure 4.5c) many nanocrystallite domains can still be observed that could be indexed to Cu_2O but in this region they are not aligned, resulting in a polycrystalline microstructure. The d-spacing labelled C measures 1.73 Å and corresponds to the (211) plane of cubic Cu_2O. The d-spacing labelled D measures 1.14 Å and corresponds to the (321) Cu_2O plane.

Unfortunately, HRTEM can only be performed on specimens that are less than 200 nm thick (i.e. that are "electron transparent") in order for the incident electrons to travel through the sample to reach the detector underneath. Due to the branched Cu_2O structures being much thicker than this, they had to be crushed in acetone with a pestle and mortar

before being analysed via TEM and it is, therefore, difficult to obtain an image that can distinguish exactly which part of the 8-branched crystals the ordered nanocrystallites (from Figure 4.5b) and the disordered nanocrystallites (from Figure 4.5d) originated from. However, it is possible to hypothesize that the ordered domains with the single crystalline diffraction pattern originated from a central seed crystal in the Cu_2O structure from which polycrystalline, disordered, branches have grown.

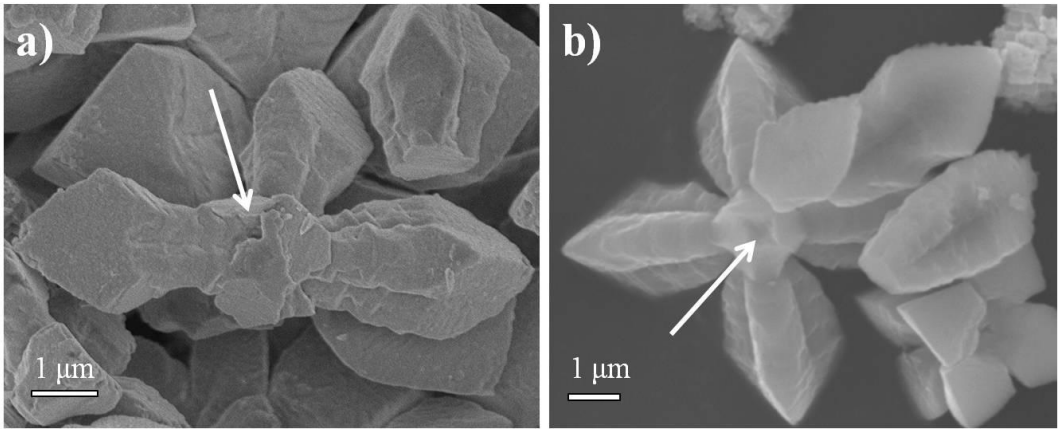

Figure 4.6. SEM images taken from the crushed 1.5 h sample. The white arrows indicate what appears to be the central seed crystal of the branched structure.

In order to find evidence of this seed crystal to support this hypothesis, the very earliest sample grown over 1.5 h was lightly crushed and analysed again via SEM. Some evidence was found of a central part of the structure from which the eight branches appear to grow as indicated by the white arrows in Figure 4.6. The combination of these SEM images and the single crystal domains identified via HRTEM go some way to support the proposition of a seed crystal from which the branches grow outwards. To prove this definitively, however, further HRTEM would be needed which could more clearly identify the microstructure of the centre of the particles vs. the branches. Alternatively, SEM images of an earlier stage, before the branches have formed, would be beneficial showing only the central seed crystal. Experiments were attempted at earlier growth times but no precipitate could be obtained prior to 1.5 h at which point the branches had already appeared. As there was no significant increase in the length of the branches as the reaction time was increased, (i.e. they appear to have reached their full length by 1.5 h), the deposition of precursor material on the {111} surfaces must be very rapid. This will be discussed in detail later in this

chapter. Other experiments were also carried out with half the concentration of the Cu precursor in an attempt to slow the growth process but unfortunately no precipitate could be obtained until 3 h at which point the crystals resembled the 2 h, 8-branched sample observed at the initial Cu-precursor concentration (Figure 4.3b).

It is clear from Figure 4.5 that there is an amorphous, organic component present in the 2 h sample in which the Cu_2O nanocrystallites are embedded. This suggests that the organic agents used in the synthetic solution are involved in the early stages of crystal growth. To fully understand the way in which these agents are involved, it is necessary to study the reaction, stage by stage, from first principles.

The first stage of the synthesis was the dissolution of the copper (II) salt into distilled water. In aqueous solution, Cu^{2+} ions will exist as complex ions, typically connected to six water molecules, $[Cu(H_2O)_6]^{2+}$, in an octahedral arrangement (23), resulting in a blue colour (as was observed in the present work). The next step was to add the organic polymer polyvinylpyrrolidone, PVP, which was stirred thoroughly into the copper solution. Shahmiri *et al.* reported the use of PVP to synthesise PVP-coated copper oxide, CuO, nanosheets via a quick precipitation method for use as antibacterial and antifungal agents (9). In their mechanism, one of the early reaction stages was the formation of a Cu^{2+}/PVP matrix according to Equation 4.1.

$$Cu(NO_3)_2.2H_2O + PVP \rightarrow [Cu/PVP]^{2+}_{(aq)} + 2NO_3^-{}_{(aq)} + 2H_2O \qquad (4.1)$$

PVP is composed of a polyvinyl skeleton with polar amide groups, which are able to donate and accept hydrogen bonds on both the O and N to form coordinative bonds with Cu^{2+} or other metal cations, giving rise to a complex compound. In this way, PVP has been used to act as a stabiliser for metal salts dissolved in aqueous solution through the electrostatic stabilisation of the amide groups of the pyrrolidone rings (24). Figure 4.7 illustrates the way Cu^{2+} ions are able to interact with a PVP molecule. In the present work, the Cu precursor ($CuCl_2.2H_2O$) should be able to form a Cu^{2+}/PVP matrix according to the same mechanism. Harada and Fujiwara have also reported the formation of a Cu^{2+}/PVP matrix (25) and go further; explaining that as the interaction between the metallic ions and the PVP molecules

allows the metallic ions to gather so closely together, PVP can in fact be used as an agent for the formation of rod-like metal particles that form along the linear PVP backbone.

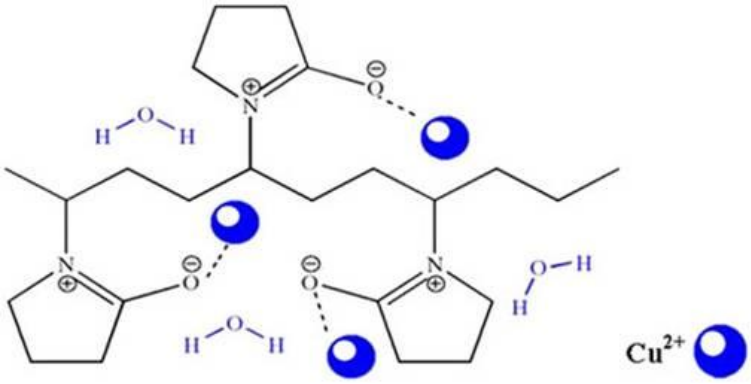

Figure 4.7. Illustration of the interaction between Cu^{2+} cations and a PVP molecule in aqueous media. Reproduced from Ref. 9 with permission from the Materials Research Society.

Once the PVP and Cu^{2+} aqueous solution had been stirred for 30 min, a buffer solution with a pH value of 7 containing potassium carbonate, K_2CO_3, and monosodium citrate, $NaC_6H_7O_7$, was added, resulting in the blue solution instantly turning a darker, more intense blue. This colour change indicates supersaturation due to hydroxylation as the citrate ions are able to pull protons from water molecules, causing the release of OH^- ions from the surrounding solution that rapidly combine with free Cu^{2+} ions in the solution to form $Cu(OH)_2$ (26). This supersaturation results in the formation of nuclei of the intermediate cupric hydroxide, $Cu(OH)_2$, phase (27). $Cu(OH)_2$ is comprised of $[Cu(OH)_6]^{4-}$ octahedra that are stabilised at low temperatures through hydrogen bonds (28). By simply raising the temperature, the hydrogen bonds between these octahedra can be broken, typically resulting in the rapid growth of copper (II) oxide nanostructures.

However, in order to form copper (I) oxide particles, the Cu^{2+} in this mechanism must be reduced to form Cu^+. In the present work, it is the glucose, which was added in the final stage of the synthesis before the reactive solution was heated, that acts as the reducing agent. Glucose is known to be a “reducing sugar” that can be oxidised in aqueous solutions because it exists in three forms: two cyclic and one linear. The linear form has an aldehyde group at end of the chain and it is this group that can be oxidised, forming a carboxylic acid group.

Although this aldehydic form of glucose is the least common of the three, it is present in small amounts and, moreover, as it is oxidised more of the linear form is produced according to Le Chatelier's principle (29). It has been reported many times that copper-citrate complexes (i.e. Benedict's solution) or copper-tartrate complexes (i.e. Fehling's solution) can be reduced by glucose to give rise to brick red Cu_2O precipitates, which are commonly applied in the analytical determination of saccharides (18, 30).

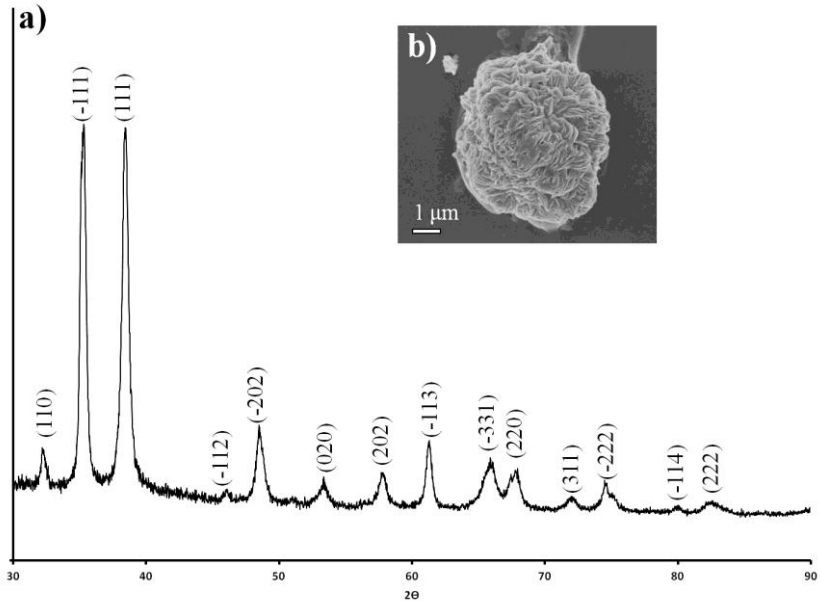

Figure 4.8. a) PXRD pattern of a sample synthesized without glucose over 4 h, all peaks are indexed to monoclinic CuO. b) SEM image from the same sample showing the typical morphology observed.

In order to support these literature findings with experimental evidence, a reaction was carried out with the glucose removed from the reactive solution over an incubation period of 4 h. The sample that resulted from this experiment was analysed using PXRD and SEM (Figure 4.8). As predicted, in the absence of glucose the Cu^{2+} precursor, $CuCl_2.2H_2O$, had not been reduced and so all of the peaks in the PXRD pattern (Figure 4.8a) could not be indexed to Cu_2O but instead corresponded to the monoclinic CuO phase with space group symmetry C2/c and unit cell parameters a = 4.6839 Å, b = 3.4734 Å, c = 5.1226 Å and β = 99.73°. SEM analysis of the samples revealed disordered CuO aggregates (Figure 4.8b).

The reduction from Cu^{2+} to Cu^{+} will not take place in the solution but actually on the surface of the growing crystal or the $Cu(OH)_2$ nuclei as Cu^{+} is actually unstable in water and rapidly undergoes a disproportionation reaction when added to aqueous media. This reaction is exothermic with a standard electrode potential, $E^{Ø}$, of + 0.37 V and so will occur spontaneously according to Equations 4.2, 4.3 and 4.4 (31).

$$Cu^{+}_{(aq)} + e^{-} \rightarrow Cu_{(s)} \qquad E^{Ø} = + 0.52 \text{ V} \qquad (4.2)$$

$$Cu^{+}_{(aq)} \rightarrow Cu^{2+}_{(aq)} + e^{-} \qquad E^{Ø} = - 0.15 \text{ V} \qquad (4.3)$$

$$2Cu^{+} \rightarrow Cu^{2+}_{(aq)} + Cu_{(s)} \qquad E^{Ø} = + 0.37 \text{ V} \qquad (4.4)$$

Furthermore, the solution remains an intense blue in colour, even after the Cu_2O precipitate has started to form, which is characteristic of Cu^{2+} complex ions. Cu^{+} complexes in solution are typically white or colourless due to the fundamental electronic configuration of the Cu^{+} ion, $[Ar]3d^{10}$, i.e. the 3d subshell is completely filled. Since no electrons can be promoted upon the formation of a complex ion, no specific absorption occurs and so the complex remains colourless. It can be concluded, therefore, that the copper/polymer matrix will exist as $[Cu/PVP]^{2+}$ in the solution, and the reduction of the cations occurs only on the octahedral $Cu(OH)_2$ nuclei, resulting in Cu_2O seed crystals. Any reduction of the Cu^{2+} in solution would result in further immediate precipitation of Cu_2O solid.

The precursor metal/organic matrix is, therefore, quite positively charged. In order for the branch growth to occur so rapidly, the clusters of this precursor matrix must have a strong attraction to the central Cu_2O seed crystal surface. This leads to the interesting possibility that one of the seed crystal surfaces may have an overall negative surface charge.

In aqueous solution, exposed metal ions on crystal surfaces are typically covered with hydroxyl (OH^{-}) groups, with the extent of the coverage dependent on the pH value of the solution. At low, acidic pH values these OH groups will not be stable and some will dissociate but in the present work the addition of the buffer solution meant the pH remained neutral and so the terminating OH groups should be quite stable. Studies of the terminating facets of metal oxide surfaces and models of their electronic structures have revealed that the charge on the terminating hydroxyl groups is highly dependent on the specific electronic

structure of the related crystal plane (32-34), i.e. it is dependent on the number of metal cations that the OH^- group is coordinated to. In the Cu_2O crystal lattice, each Cu^+ ion is doubly coordinated, i.e. it is connected to two neighbouring O^{2-} ions. This means that it donates a charge of +½ per bond, and so an exposed Cu^+ ion on a Cu_2O crystal surface will donate +½ charge to any OH^- group it is coordinated to. Therefore, if a hydroxyl group is doubly coordinated (connected to two Cu ions); the overall charge is neutral, or OH^0. If a hydroxyl group was singly coordinated, however, the overall charge would become negative ($OH^{0.5-}$) and, conversely, if the hydroxyl group was triply coordinated then the overall charge would become positive ($OH^{0.5+}$). This is illustrated in Figure 4.9.

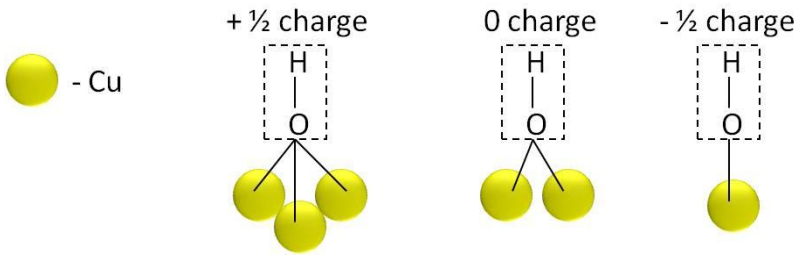

Figure 4.9. Schematic demonstrating the charges of terminating hydroxyl groups when they are triply, doubly or singly coordinated with Cu^+ ions from the Cu_2O crystal surface.

CrystalMaker software was used to model the surfaces of the terminal facets along the principal axes of cuprous oxide as displayed in Figures 4.10, 4.11 and 4.12 where the larger red spheres represent oxygen and the smaller yellow spheres represent copper. The highlighted oxygen atoms represent those in the surface layer of that facet. For each plane, the cross-section was observed in order to determine which oxygen atoms were the true surface ones. After this, to obtain images solely of the terminating plane, atomic layers were removed from the structure one by one until a final, single layer of each surface was left, revealing the coordination of the oxygen atoms in the terminating layer. The coordination of oxygen atoms represents the coordination of the sites at which terminating –OH groups would be found on the surface layer.

Figure 4.10a shows the cross section of the (100) surface and Figure 4.10b shows the structure as viewed looking down at the (100) plane. The images clearly show that this plane

consists only of doubly coordinated, terminating oxygen atoms and, therefore, all terminating hydroxyl groups on the (100) surface would be neutral, OH^0.

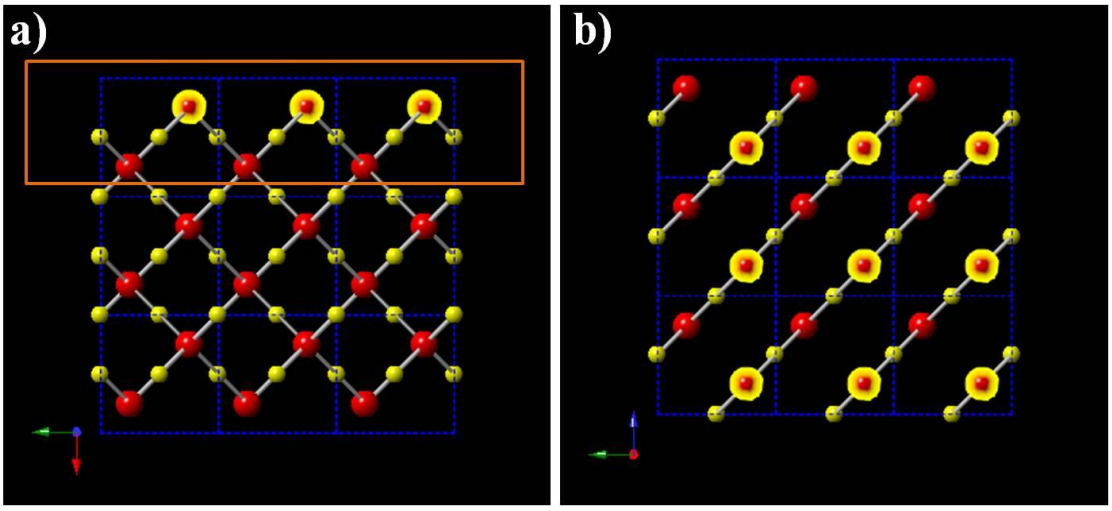

Figure 4.10. CrystalMaker images of the Cu_2O structure where red spheres represent O and yellow spheres represent Cu. a) Cross-section of the (100) facet with the surface O atoms highlighted. b) Image with the view direction down the (100) terminating plane, all atoms have been deleted from the greater structure apart from those within the orange rectangle marked in a) so only the surface layer remains. Each surface O is connected to two Cu, i.e. the surface O atoms are doubly coordinated.

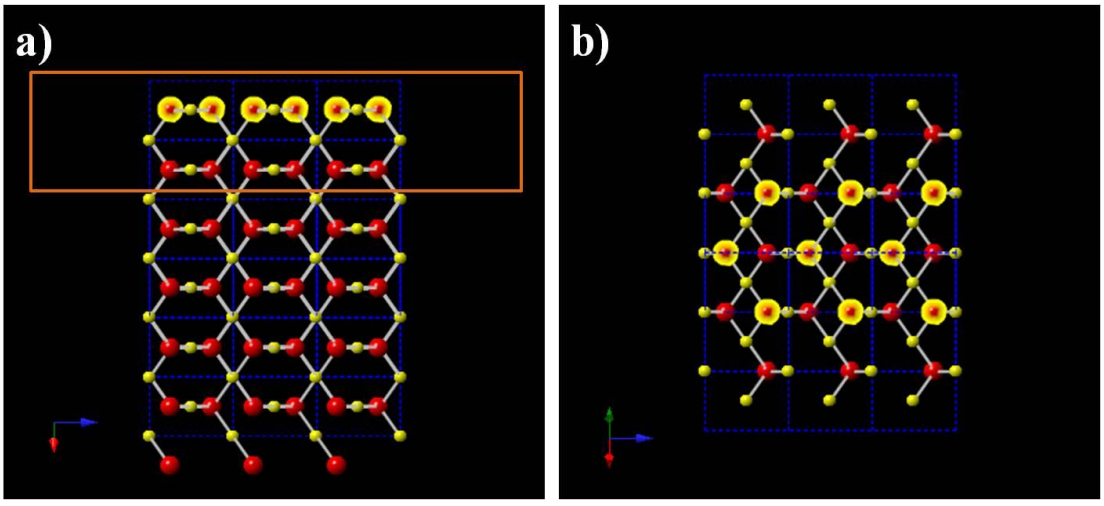

Figure 4.11. CrystalMaker images of the Cu_2O structure where red spheres represent O and yellow spheres represent Cu. a) Cross-section of the (110) facet with the surface O atoms highlighted. b) Image with the view direction down the (110) terminating plane, all atoms have been deleted from the greater structure apart from those within the orange rectangle marked in a) so only the surface layer remains. Each surface O is connected to three Cu, i.e. the surface O atoms are triply coordinated.

Figure 4.11a shows the cross section of the (110) surface, which is slightly more complicated as it can be seen that there are both Cu and O atoms in the terminating layer. Figure 4.11b shows the structure as viewed looking down at the (110) plane. It can be observed that, in this case, the surface oxygen atoms are in fact connected to three Cu ions (one in the surface layer and two in a lower layer). This means that the terminating hydroxyl groups on the (110) surface would all be triply coordinated and, therefore, positively charged $OH^{0.5+}$, and so the terminating (110) facet would have an overall positive charge.

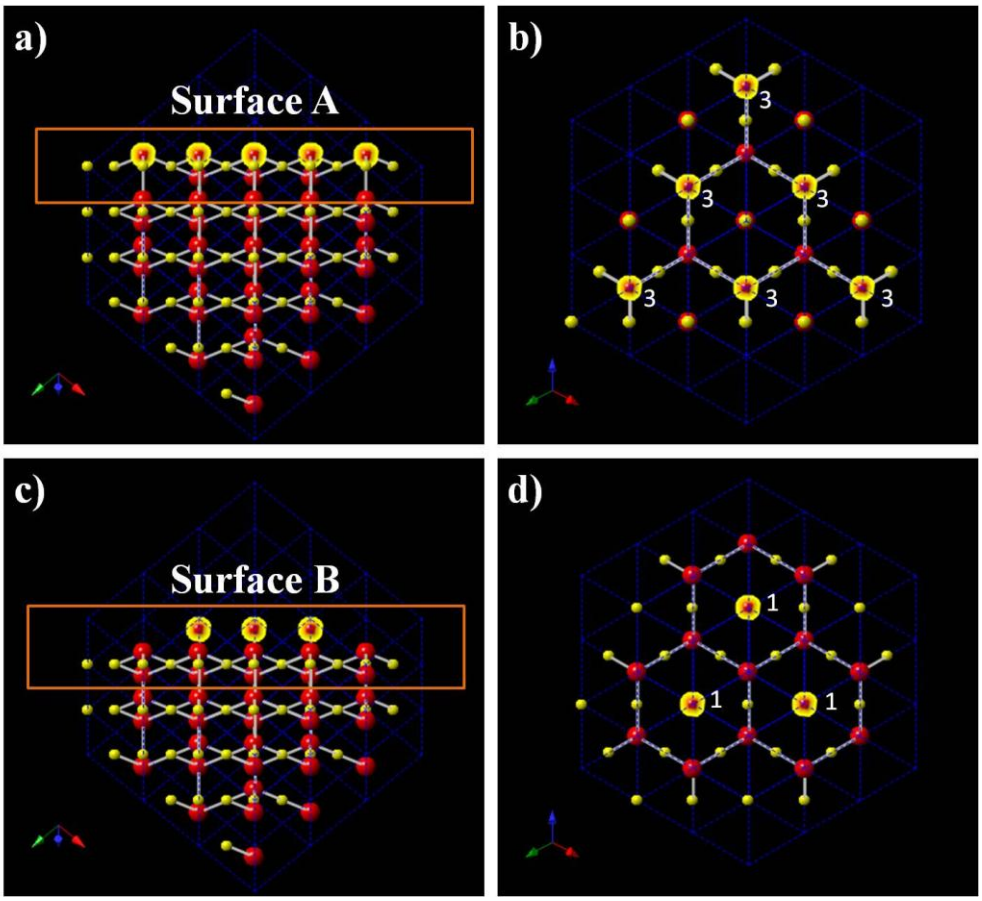

Figure 4.12. CrystalMaker images of the Cu_2O structure where red spheres represent O and yellow spheres represent Cu. a) Cross-section of the (111) facet showing one of the possible terminating surfaces, labelled Surface A. b) Image with the view direction down the (111) terminating plane, Surface A, showing only those atoms from within the orange rectangle marked in a). In Surface A, each surface O is connected to three Cu and so they have been labelled '3'. The highlighted Cu atoms exist on the surface and are not fully coordinated within the crystal structure. c) Cross-section of the (111) facet showing the other possible terminating surface, labelled Surface B. d) Image with the view direction down the (111) terminating plane, Surface B, showing only those atoms from within the orange rectangle marked in c). In Surface B, each surface O is connected to only one Cu and so they have been labelled '1'.

Since the $[Cu/PVP]^{+}$ matrix would be electrostatically attracted only to negative sites, it is clear that neither the neutral {100} nor the positive {110} surfaces would be suitable for this kind of interaction. Studies of the {111} surfaces, however, revealed a much more complicated and more interesting structure. The terminating (111) surface was found to be comprised of alternating triply and singly coordinated oxygen sites, and so the surface charge depends on which point the structure is stopped at. Figure 4.12 displays the two possible terminating faces, which have been labelled Surface A (triply coordinated surface oxygen atoms) and Surface B (singly coordinated surface oxygen atoms).

Figure 4.12a shows the cross section of Surface A, one of the possible terminating {111} surfaces. Figure 4.12b shows the structure as viewed looking down at Surface A, down the (111) plane. It can be observed that all of the highlighted, surface O atoms on this surface are coordinated to three Cu and so terminating hydroxyl groups on these sites would have a positive charge, $OH^{0.5+}$, in the same way that the triply coordinated groups on the terminating (110) plane did and so, once again, this surface would not be suitable to attract the positively charged precursor material.

Figure 4.12c shows the cross section of Surface B, which is the other possible terminating (111) surface in the Cu_2O crystal structure. Figure 4.12d shows the structure as viewed looking down at Surface B, down the (111) plane. In this case, all of the highlighted, surface O atoms are only coordinated to a single Cu (directly beneath them when viewed down the [111] direction) and so the terminating hydroxyl groups on these surface sites would actually have a negative charge, $OH^{0.5-}$.

While Surface B, with these negatively charged, singly coordinated $OH^{0.5-}$ groups, may provide an opportunity for the positive $[Cu/PVP]^{2+}$ precursor material to bond, it is clear that Surface A would cause the opposite effect and so it must be considered which of the possible terminating surfaces is most likely to be the true one. For this purpose, it is necessary to study the Cu atoms in the surface layers. In Surface B all of the Cu atoms are below the surface O atoms and they are fully coordinated within the structure, i.e. they are already connected to two O atoms. In Surface A, however, some of the Cu atoms are not fully coordinated and are only connected to one O atom. These singly coordinated Cu atoms are highlighted in Figure 4.12b. Surface A would, therefore, be highly unstable as an O atom would rapidly be added to the structure to ensure the exposed Cu was fully coordinated. As soon as all of the singly coordinated Cu atoms in Surface A have been coordinated to extra O

atoms from the solution, the terminating plane once again becomes the much more favourable Surface B. The most stable terminating (111) face will be, therefore, Surface B and will consist of singly coordinated, negatively charged, terminating hydroxyl groups.

Since these negative $OH^{0.5-}$ groups are unique to the {111} terminating facets, this goes some way to explain why growth could happen so rapidly only along the <111> directions, causing a deviation from classical crystal growth and resulting in the 8-branched Cu_2O structure. Since the PVP has allowed the Cu^+ ions to gather so closely together, it can act as an agent for the formation of the disordered Cu_2O nanocrystallites observed in the early stage HRTEM analysis (Figure 4.5d) which form along the linear PVP backbone as suggested by Harada and Fujiwara (25). This explains why the branch formation is so rapid.

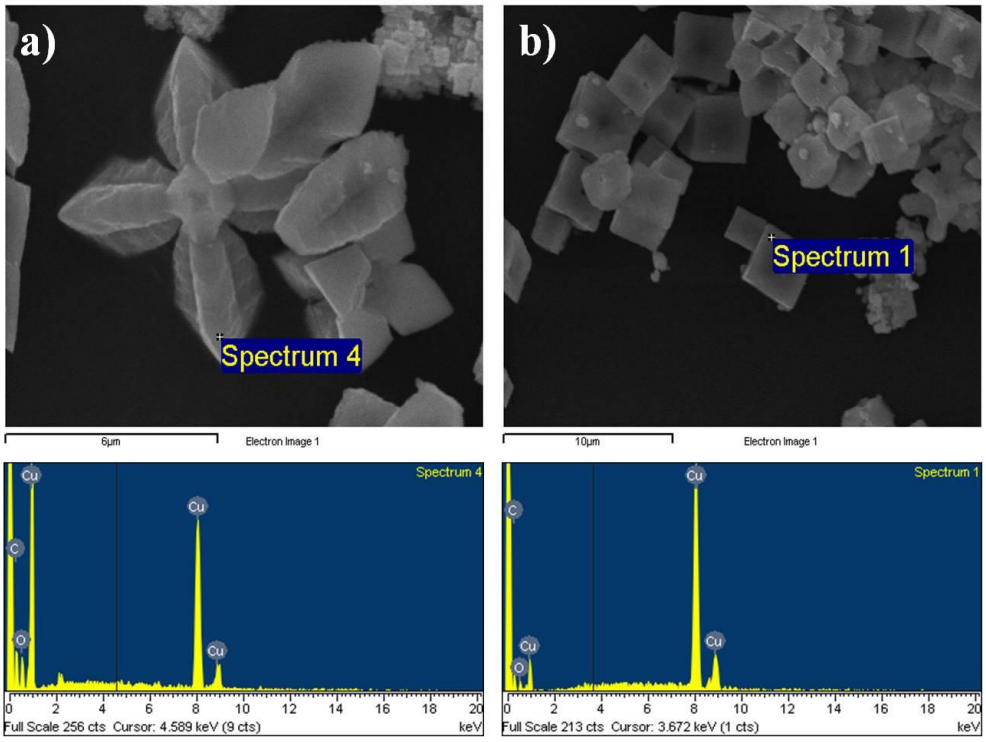

Figure 4.13. SEM images taken from a) the 1.5 h sample and b) the 13 h sample with the corresponding EDX patterns displayed beneath revealing peaks which corresponded to Cu, O and C.

Over time, the nanocrystallites of Cu_2O grow larger, join together and move towards the energetically favourable cubic morphology according to the drive to minimise surface free energy. The organic PVP component of the particles must, therefore, move out of the

structure over time as more precursor material recrystallises to Cu_2O. EDX analysis was performed on the 1.5 h and 13 h samples in an attempt to support this and to observe whether any organic matter was still present in the structures at the later, cubic, stage of the growth process (Figure 4.13). Cu and O peaks were observed for both samples as expected as well as a peak corresponding to C. The weight % observed for C in the samples did decrease over time from 22.89 % in the 1.5 h sample to 11.23 % in the 13 h sample, which may indicate a decrease in the amount of organic in the structure. However, carbon peaks in EDX are not very reliable as they can be affected by several factors. For example, the samples had to be mounted onto a carbon tab before being inserted into the SEM for EDX analysis and so it is difficult to distinguish how much the carbon tab may have contributed to the C signal. Therefore, further analysis was required to support the hypothesis that the amount of PVP in the Cu_2O structures must decrease over time.

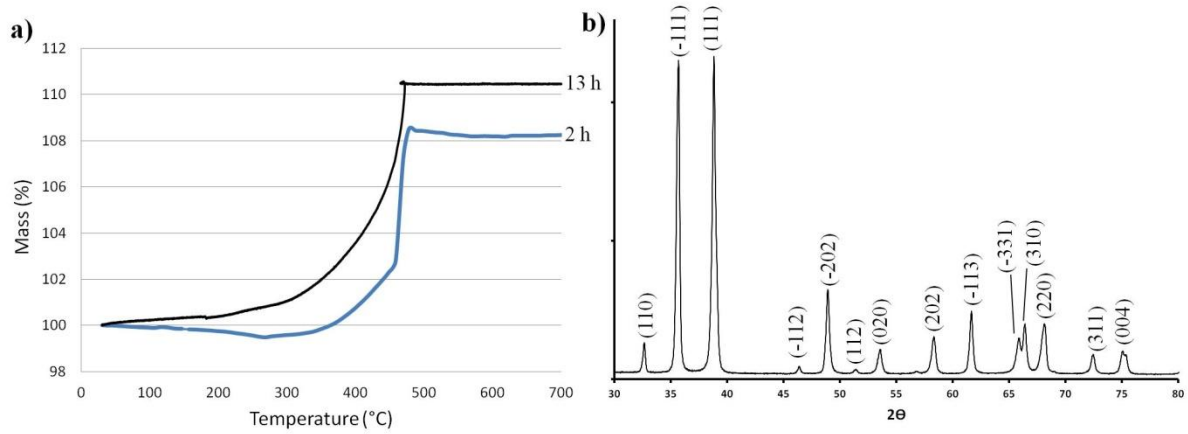

Figure 4.14. a) TGA results showing % change in mass as a function of increasing temperature. The lower line represents the 2 h sample and the upper line represents the 13 h sample. b) PXRD pattern of the 13 h sample after calcination at 600 °C for 2 h, showing a phase transition has occurred during the TGA experiment from Cu_2O to CuO. All peaks are indexed to monoclinic CuO.

TGA analysis was then performed on the 2 h and 13 h samples and a distinct increase in mass was observed for both samples (Figure 4.14a). This was expected to be due to a phase change from Cu_2O to the more stable CuO as the samples were heated in air. To confirm that this was indeed the phase transition taking place, a 13 h sample was calcined at 600 °C (i.e. to above the temperature at which the mass increase occurred) for 2 h and was

then analysed via PXRD. As can be seen from Figure 4.14b, the PXRD peaks could all be indexed to monoclinic CuO, confirming the predicted phase transition.

If the only transition occurring during the TGA experiment was the phase transition of the sample from Cu_2O to CuO a mass increase of 11.2 % would be expected. However, in both the 2 h and the 13 h samples, the % mass increase was actually less than this. This decrease of mass relative to the calculated value is due to the organic (PVP) in the samples being removed as the material is heated. The actual mass increase for the 2 h and 13 h samples was 8.3 % and 10.5 % respectively, i.e. there was a larger mass decrease relative to the calculated value for the 2 h sample than there was for the 13 h sample. This leads to the conclusion that there was more organic removed from the earlier stage Cu_2O particles, fitting with the theory that the PVP moves out of the structure over time as the Cu_2O nanocrystallites grow larger and join together.

It is well known that the favourable final morphology of a crystal is the equilibrium shape that results from minimizing the surface free energy, as first suggested by Curie and Wulff over a century ago (35). For Cu_2O, the favourable final shape is a cubic morphology, reflecting the cubic unit cell. Therefore, as the Cu_2O nanocrystallites within the organic, PVP, matrix grow larger and join together, they arrange themselves in a way that minimizes the surface free energy, and so they transition towards a cubic shape. As discussed, there must also be a movement of PVP out of the structure over time as more Cu_2O crystallizes (since the Cu^+ ions are obtained for the crystals from the Cu/PVP matrix), i.e. the ratio of PVP to Cu free in solution must increase as the Cu^+ are absorbed into the growing crystals. Xu *et al.* (20) studied the growth of different Cu_2O morphologies using ethylenediaminetetraacetic acid tetrasodium salt dihydrate (EDTA salt) as both the chelating reagent and reductant and they observed that the ratio of EDTA to Cu^{2+} in the solution affected the direction of growth in a similar way to the present work. They state that when the EDTA:Cu^{2+} ratio was 1 the prominent growth direction was along the <111> directions but when the EDTA:Cu^{2+} ratio was 2, the <100> directions became the prominent growth routes and so a cubic morphology was observed. The authors attribute this solely to the ability of the EDTA to stabilise the {100} surfaces, hence the cubic morphology, but this fails to explain why the branching along the <111> directions happens so rapidly during the initial stage and it also only works on the assumption that the branches are single crystalline at all growth stages which has been proven not to be the case by the HRTEM results obtained during this project (Figure 4.5c and 4.5d).

Taking into account the observations from the present work and those from the literature it is now much more clear that the Cu/organic matrix plays a key role in the rapid branch growth along the <111> directions in conjunction with the unique electronic structure of the terminating {111} planes. Over time, as the ratio of organic to Cu ions increases, the amount of $[Cu(PVP]^{2+}$ clusters in the solution will decrease and so the role of the organic as a stabiliser for the {100} starts to become more prominent than its role as an agent for Cu^{2+} aggregation (and, therefore, Cu_2O crystal growth) along the <111> directions. This explains the initial rapid growth along <111> followed by a slowing of growth in these directions and, instead, a transition from an 8-branched to a cubic morphology.

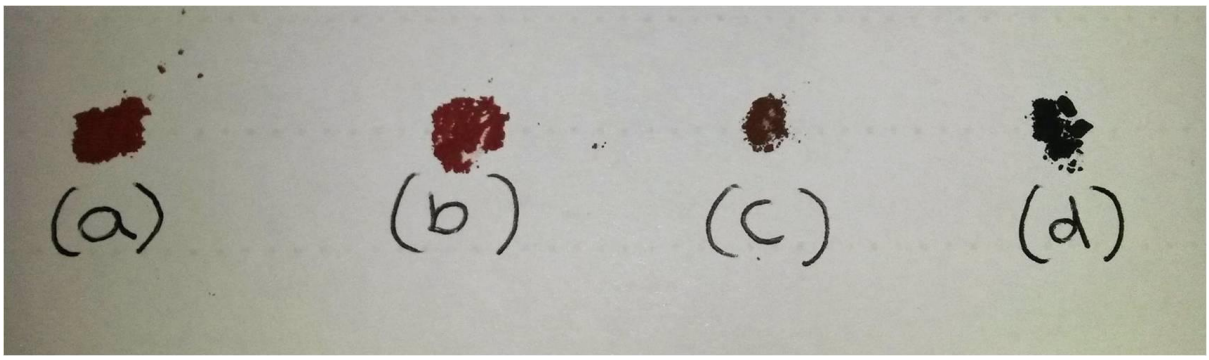

Figure 4.15. Photograph displaying the clear colour change from bright red to black in precipitates collected from growth times of a) 2 h, b) 4 h, c) 48 h and d) 20 days

The next stage of this project was to observe what happened when the reaction was allowed to continue for a much longer period of 20 days. The precipitate collected from this experiment was visibly different to the others as it was black, in contrast to those from the early stages that had been the characteristic red colour associated with Cu_2O (Figure 4.15). Initial SEM (Figure 4.3f) and PXRD (Figure 4.4e) studies of the late stage sample revealed no regular morphology and that the Cu_2O crystals had undergone a phase transition and been reduced to copper metal. EDX analysis revealed elements of Cu, C and O were present after 20 days of growth but that the relative intensity of the O signal was now so low (less than 7 %) it was almost impossible to see as a peak in the spectrum. To study this change in more detail, the late stage sample was analysed via HRTEM (Figure 4.16).

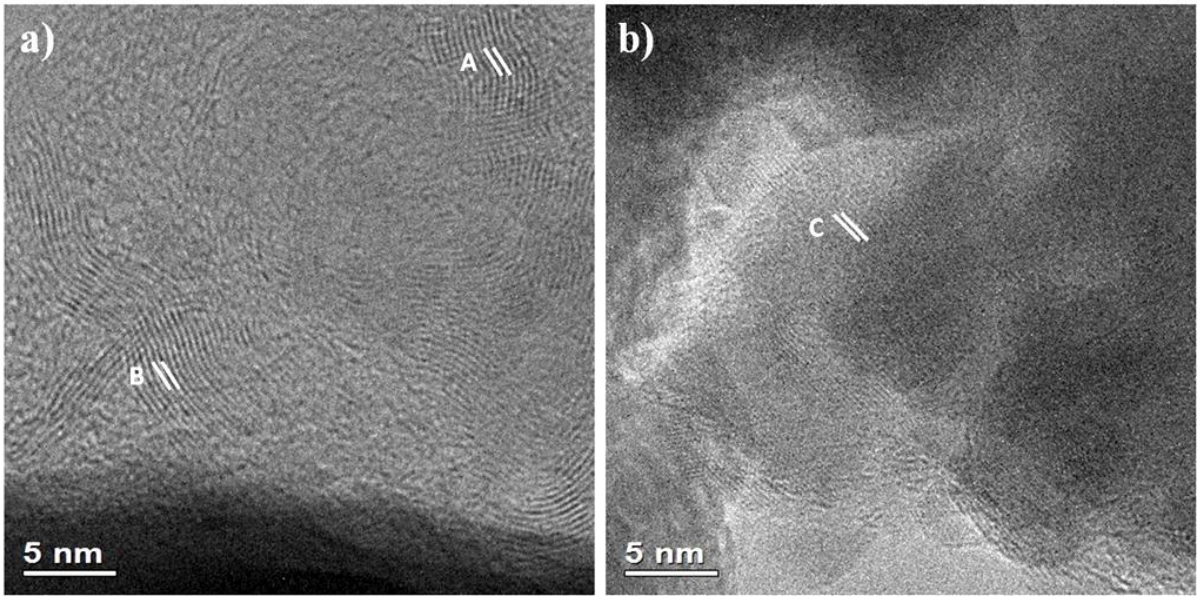

Figure 4.16. HRTEM images taken from the 20 day sample. a) Micrograph showing the graphite layers coating the Cu particles. The d-spacings marked A and B measure 3.68 Å and 4.08 Å, respectively and both could be indexed to the hexagonal graphite phase. A corresponds to the (102) plane and B to the (101) plane. b) Micrograph showing a region that could be indexed to cubic Cu. The d-spacing labelled C measured 1.29 Å, which corresponds to the (220) Cu plane.

It was observed that the 20 day sample was composed of copper metal nanoparticles which were encased in layers of graphite or graphite oxide. The d-spacings labelled A and B in Figure 4.16a could not be indexed to Cu but were actually found to correspond to the (102) and (101) planes of hexagonal graphite, respectively, which has P63/mmc space group symmetry and unit cell parameters a = 2.464 Å and c = 6.711 Å. The d-spacing marked A measured 3.68 Å and the d-spacing marked B measured 4.08 Å. However, the interlayer spacing for graphite (and, therefore, the most common d-spacing) is known to be 3.35 Å, corresponding to the (002) plane (36), which was not observed in the HRTEM analysis of the 20 day sample. This means that the layers coating the Cu particles are more likely to be graphite oxide, in which the aromatic lattice of graphite is interrupted by groups such as alcohols or ketones (37). Despite the exact structure of graphite oxide being difficult to determine, it is known that the interruptions in the aromatic lattice cause an increase in the interlayer spacing from 3.35 Å upwards to 6.25 Å (38). This may explain the larger d-spacings observed in the present case.

The d-spacing labelled C in Figure 4.16b measured 1.29 Å, which corresponds to the (220) plane of cubic Cu. Unfortunately, the presence of the graphitic layers covering the Cu nanoparticles made it difficult to attain a higher quality HRTEM image of the Cu lattice fringes. The pH of the reactive solution was measured over time and, although it started as neutral, it was found to have an acidic value of pH 5 after 20 days of reaction. This is in accordance with the discovery of graphite or graphite oxide having formed since these materials typically exhibit an acidic pH of 3 to 5 in aqueous media (39).

The transition from Cu_2O to Cu metal is simply the result of a further reduction from the Cu^{2+} ions in the initial reactive solution to Cu^{+} and then to Cu. Feng *et al.* (40) reported the synthesis of Cu_2O octahedral crystals and observed weak diffraction peaks of the Cu (111) and (211) planes alongside the expected Cu_2O diffraction peaks in their PXRD analysis. The reason was that the hydrazine used in their experiments as the reducing agent was twice the amount of the stoichiometric ratio required to reduce the Cu^{2+} to Cu^{+}, and so some Cu^{2+} was further reduced to Cu. The same is the case in the present work since (as explained earlier in this discussion) glucose has been used as the reducing agent, which exists in two non-cyclic and one linear (aldehydic) form. Therefore, as more of the aldehydic form of glucose was oxidised, more was produced from the non-cyclic forms in the solution according to Le Chatelier's principle. This means that the glucose was able to continue to reduce the ions from Cu^{2+} to Cu^{+} and, eventually, to Cu.

After this, the graphitic layers produced are likely to be due to the degradation of the glucose molecules. Although heavily involved in the initial crystal growth stages, PVP is unlikely to have played a role here as it has a thermal degradation temperature of approximately 392 °C, which is much higher than the 100 °C reaction temperature used in the present work and so it is improbable that the PVP molecules could have undergone pyrolysis to form graphite oxide. Glucose, on the other hand, has been used as the sole reagent to form graphite oxide at much closer temperatures to that used in the present work. Tang *et al.* (41) published a study in 2012 that presented the synthesis of graphene oxide nanosheets via a facile hydrothermal method in which glucose was simply dissolved in distilled water and heated at 160 °C for just 70 min. Although the temperature used by Tang *et al.* was slightly higher than that used in the present work, their growth period was much shorter (70 min compared to 20 days) and so it is possible that the same degradation occurs in the present work but simply at a much slower rate due to the lower temperature employed.

Further studies should be conducted into the properties and potential applications of these graphite or graphite oxide coated Cu particles as there have been many reports that copper-graphite composites possess both the desirable properties of copper (such as exceptional thermal and electrical conductivities) and those of graphite (such as a small thermal expansion coefficient) (42). This has led to Cu-alloy/graphite composites being highly desirable as brushes and sliding bearing materials for many applications (43). Various complicated methods have been utilised to produce these Cu/graphite composites such as hot isostatic pressing, sintering, cold pressing and infiltration (44) but the present work appears to be the first case in which graphite-coated copper particles could be generated via a facile, hydrothermal route.

Summary of the growth mechanism of 8-branched Cu_2O

With the studies and analysis discussed so far it is clear that the 8-branched Cu_2O structures do not follow the classical crystal growth theory as the branches are not single crystals at the early growth stages and the branched morphology, with such a high surface area, cannot be the result of a drive to minimise the surface free energy. A new mechanism for their growth can now be proposed.

In the initial stage, during the synthesis, Cu^{2+} ions coordinate with the lone electron pairs on N and O atoms of the long, linear PVP molecules added to the solution, forming many clusters of a positively charged $[Cu/PVP]^{2+}$ precursor matrix. Potassium carbonate, K_2CO_3, and monosodium citrate, $NaC_6H_7O_7$, were then added which caused supersaturation of the free Cu^{2+} ions in solution and, therefore, the formation of nuclei of the intermediate phase of cupric hydroxide, $Cu(OH)_2$.

The next step is the reduction of the octahedral $Cu(OH)_2$ nuclei when heated with the reducing sugar, glucose, to form Cu_2O seed crystals. These seed crystals are likely to remain octahedral as this is one of the most typical forms of Cu_2O and would provide eight exposed {111} facets on which the eight branches can develop. The typical morphologies of Cu2O crystals are cubic (formed by 6 {100} facets), rhombic dodecahedral (composed of 12 {110} facets) and octahedral (consisting of 8 {111} facets) (45). The positively charged $[Cu/PVP]^{2+}$ precursor clusters are attracted to the negative hydroxyl groups which exist on the {111} Cu_2O terminating facets (Figure 4.17b). This results in rapid aggregation of linear

[Cu/PVP]$^{2+}$ chains in the <111> directions, giving rise to the 8-branched structures observed from the short growth time of 1.5 h (Figure 4.17c). Upon reduction, the Cu^{+} ions within the branches are able to gather closely together and undergo recrystallization to form many nanocrystallites of Cu_2O.

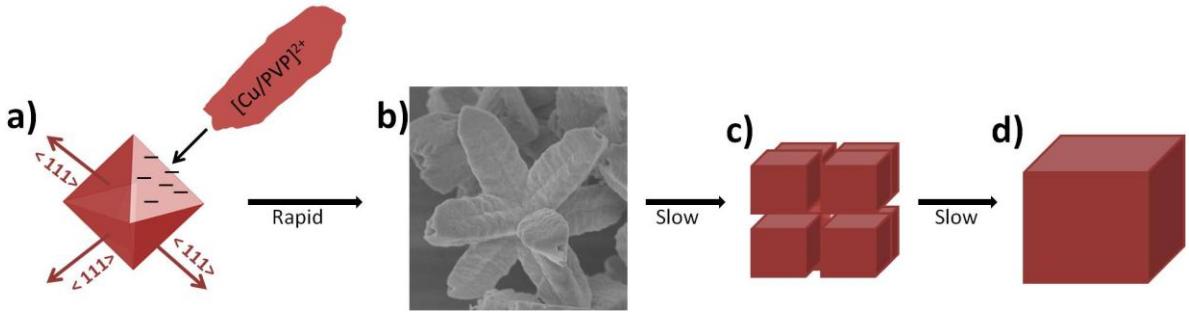

Figure 4.17. A schematic displaying the growth of 8-branched Cu_2O structures followed by the transition to a cubic morphology. a) The clusters of positively charged [Cu/PVP]$^{2+}$ precursor material are attracted to the negatively charged terminating hydroxyl groups on the Cu_2O seed crystal {111} surfaces resulting in rapid aggregation along the <111> directions. b) The earliest appearance of the 8-branched structure where disordered branches grow out from a central seed crystal. c) According to the drive to minimise surface energy, the branches move towards a cubic shape as the Cu_2O nanocrystallites within them grow larger and join together. d) Finally the branches grow large enough to join together forming a perfect cubic morphology.

As the reaction time is increased, the Cu_2O nanocrystallites embedded in the branches, which were directly observed via HRTEM analysis as shown in Figure 4.5, grow larger and larger, joining together and forcing the organic out of the structure. According to the drive to minimize the surface free energy of the crystals, they move towards a cubic shape as the reaction proceeds, reflecting the cubic unit cell of Cu_2O (Figure 4.17c). This means that, after the initial rapid growth along the <111> directions, there is then predominant growth on the {100} facets. Eventually, the branches grow large enough that they are able to join together, forming the perfect cubic morphology that is observed after a reaction time of 13 h (Figure 4.17d).

The final step in the process is the further reduction of the Cu^{+} to Cu metal nanoparticles and the degradation of the glucose to form layers of graphite or graphite oxide. This causes a further change in morphology: the cubic appearance is lost as the oxygen ions

diffuse out of the structure and the final result is Cu nanoparticles with no distinguishable morphology coated in graphite or graphite oxide.

4.4 Conclusions

The results of this project provide further evidence that the classical crystal growth theory is often not applicable to metal oxide crystals, complementing the conclusions drawn from the previous chapter on the non-classical growth of zinc oxide structures.

Whilst there have been many reports of the range of morphologies Cu_2O crystals can adopt, there have still been many questions left unanswered in the discussions about how and why these interesting morphologies have originated. Some have reported that the formation of 8-branched Cu_2O structures followed by a transition to a cubic morphology is simply a result of faster growth along the <111> directions (18). Others have suggested preferential growth on different terminating facets is due to the pH of the initial solution (21, 40) or of the presence of organic materials which may stabilize certain faces (20). All of these studies, however, make the assumption that the branches are single crystalline at all growth stages and so, after the initial nucleation and formation of a central seed crystal, the branches still grow via the classic "bottom-up" route in which atoms are deposited on the growing crystal surface layer-by-layer.

Through HRTEM and TGA analysis, however, it has been possible to prove that this cannot be the case in the present work due to the polycrystalline nature of the branches and to the existence of organic in the structure from which nanocrystallites of Cu_2O are formed. This work, therefore, challenges conventional knowledge and the classical theories and instead shows that the formation of a Cu/PVP matrix in the solution competes with the classical crystal growth process, leading to a process of aggregation of PVP and Cu ions followed by recrystallization to Cu_2O within the organic matrix. Studies of the electronic structure of the main terminating facets of Cu_2O have also resulted in the discovery of differently charged hydroxyl groups on the different terminating facets which also play a key role in the branch formation. This mechanism, whereby charged surface hydroxyl groups attract precursor material, has also been found to be the case for snowflake-like hematite crystals, with six-fold symmetry, which display rapid branch growth along the $<11\bar{2}0>$ directions (46). This will be discussed in more detail in Chapter 5. The drive to minimize

surface energy then takes over as the branched structures move towards their final, cubic morphology and the PVP moves out of the structure.

It is vital to fully understand the mechanism by which crystals such as these form as a true understanding of their growth process allows us to stop the process at desired points and alter the morphology if required. These Cu_2O cubes are worthy of such in depth analysis as, if their morphology can be more finely controlled, their desirable properties can be maximised for their many potential applications in a range of fields from constructing solar energy conversion devices (5) to studying the spontaneous Bose coherence of excitons and polaritons (6, 18).

Whilst the results gathered thus far go a long way in explaining the rapid formation of the 8-branched Cu_2O structure, more work must be done in order to fully explain the transition to a cubic shape. More specifically, it is still unknown how the overall cubic shape can have appeared before the branches are connected. This implies that the disordered nanocrystallites within the branched structure must become ordered, or self-orientated before they are connected in the cubic structure.

Further work may also be needed to determine the full mechanism of the formation of graphite oxide around the final copper particles. Graphite/copper composites are promising materials as brushes and sliding bearing materials for many applications (43) but there are no previous reports of such materials being synthesized via such a simple, hydrothermal route.

References

1. (a) Grozdanov, I. *Mater. Lett.*, **1994**, *19*, 281. (b) Shen, M. Y.; Yokouchi, T.; Koyama, S.; Goto, T. *Phys. Rev. B*, **1997**, *56*, 13066. (c) Shi, W.; Lin, K.; Lin, X. *J. Appl. Phys.*, **1997**, *81*, 2822.
2. (a) Xiong, L.; Huang, S.; Yang, X.; Qiu, M. Q.; Chen, Z. G.; Yu, Y. *Electrochim. Acta*, **2011**, *56*, 2735. (b) Ma, L.; Lin, Y.; Wang, Y.; Li, J.; Wang, E.; Qiu, M. Yu, Y. *J. Phys. Chem. C*, **2008**, *112*, 18916. (c) Rakhshani, A. E. *Solid State Electron.*, **1986**, *29*, 7.
3. (a) Ramírez-Ortiz, J.; Ogura, T.; Medina-Valtierra, J.; Acosta-Ortiz, S. E.; Bosch, P.; de los Reyes, J. A.; Lara, V. H. *Appl. Surf. Sci.*, **2001**, *174*, 177. (b) Yang, H.;

Ouyang, J.; Tang, A.; Xiao, Y.; Li, X. W.; Dong, X. D.; Yu, Y. M. *Mater. Res. Bull.*, **2006**, *41*, 1310.

4. Shishiyanu, S. T.; Shishiyanu, T. S.; Lupan, O. I. *Sens. Actuators B*, **2006**, *113*, 468.
5. (a) Mittiga, A.; Salza, E.; Sarto, F.; Tucci, M.; Vasanthi, R. *Appl. Phys. Lett.*, **2006**, *88*, 163502. (b) Briskman, R. N.; *Sol. Energy Mater. Sol. Cells*, **1992**, *27*, 361. (c) Olsen, L. C.; Addis, F. W.; Miller, W. *Sol. Cells*, **1982**, *7*, 247.
6. Snoke, D. *Science*, **2002**, *298*, 1368.
7. Chen, K.; Song, S.; Xue, D. *J. Appl. Crystallogr.*, **2013**, *46*, 1603.
8. Zang, Z.; Nakamura, A.; Temmyo, J. *Opt. Express*, **2013**, *21*, 11448.
9. Shahmiri, M.; Ibrahim, N. A.; Shayesteh, F.; Asim, N.; Motallebi, N. *J. Mater. Res.*, **2013**, *28*, 3109.
10. Chen, Y.-S.; Liao, C.-H.; Chueh, Y.-L.; Lai, C.-C.; Chen, L.-Y.; Chu, A.-K.; Kuo, C.-T.; Wang, H.-C. *Opt. Mater. Express*, **2014**, *4*, 1473.
11. Guo, H.; Liu, L. X.; Li, T. T.; Chen, W. W.; Liu, J. J.; Guo, Y. Y.; Guo, Y. C. *Nanoscale*, **2014**, *6*, 5491.
12. (a) Khan, R.; Vaseem, M.; Jang, L.-W.; Yun, J.-H.; Hahn, Y.-B.; Lee, I.-H. *J. Alloy. Compd.*, **2014**, *609*, 211. (b) Gou, L.; Murphy, C. J. *Nano. Lett.*, **2003**, *3*, 231.
13. (a) Feng, L. L.; Zhang, C. L.; Gao, G.; Cui, D. X. *Nanoscale Res. Lett.*, **2012**, *7*, 276. (b) Lu, C.; Qi, L.; Yang, J.; Wang, X.; Zhang, D.; Xie, J.; Ma, J. *Adv. Mater.*, **2005**, *17*, 2562.
14. Chen, K.; Sun, C.; Song, S.; Xue, D. *Cryst. Eng. Comm.*, **2014**, *16*, 5257.
15. (a) Siegfried, M. J.; Choi, K. S. *Adv. Mater.*, **2004,** *16*, 1743. (b) Siegfried, M. J.; Choi, K. S. *Angew. Chem. Int. Ed.*, **2005**, *44*, 3218. (c) Siegfried, M. J.; Choi K. S. *J. Am. Chem. Soc.*, **2006**, *128*, 10356. (d) Yao, W.-T.; Yu, S.-H.; Zhou, Y.; Jiang, J.; Wu, Q.-S.; Zhang, L.; Jiang, J. *J. Phys. Chem. B*, **2005**, *109*, 14011.
16. Taneja, P.; Chandra, R.; Banerjee, R.; Ayyub, P. *Scr. Mater.*, **2001**, *44*, 1915.
17. Kumar, R. V.; Mastai, Y.; Diamant, Y.; Gedanken, A. *J. Mater. Chem.*, **2001**, *11*, 1209.
18. Wang, D.; Mo, M.; Yu, D.; Xu, L.; Li, F.; Qian, Y. *Cryst. Growth Des.*, **2003**, *3*, 717.
19. Ram, S.; Mitra, C. *Mater. Sci. Eng. A*, **2001**, *304*, 805.
20. Xu, J.; Xue, D. *Acta Mater.*, **2007**, *55*, 2397.
21. Wang, L.-C.; Jia, H.; Shi, L.-Y.; Liao, N.; Yu, X.-J.; Jin, D.-L. *Inorg. Mater.*, **2010**, *46*, 847.
22. Daltin, A.-L.; Addad, A.; Baudart, P.; Chopart, J.-P. *CrystEngComm.*, **2011**, *13*, 3373.

23. Wu, R.; Ma, Z.; Gu, Z.; Yang, Y. *J. Alloys Compd.*, **2010**, *504*, 45.
24. Soltani, N.; Saion, E.; Erfani, M.; Rezaee, K.; Bahmanrokh, G.; Drummen, G. P.; Bahrami, A.; Hussein, M. Z. *Int. J. Mol. Sci.*, **2012**, *13*, 12412.
25. Harada, T.; Fujiwara, H. *J. Phys. Conf. Ser.*, **2007**, *61*, 394.
26. Oskam, G. *J. Sol-Gel Sci. Technol.*, **2006**, *37*, 161.
27. Zhang, Q. B.; Zhang, K. L.; Xu, D. X.; Yang, G. C.; Huang, H.; Nie, F. D.; Liu, C. M.; Yang, S. H. *Prog. Mater. Sci.*, **2014**, *60*, 208.
28. Rodriguez-Clemente, R.; Serna, C. J.; Ocana, M.; Matijevic, E. *J. Cryst. Growth*, **1994**, *143*, 277.
29. Le Chatelier, H.; Boudouard, O. *Bull. Soc. Chim. Fr.*, **1898**, *19*, 483.
30. Petrucci, R. H. *General Chemistry, 4th ed.*, Macmillan Publishing Company, New York, **1985**; p 848.
31. MacKay, K. M.; MacKay, R. A.; Henderson, W. *Introduction to Modern Inorganic Chemistry, 6th Edition*, Nelson Thornes Ltd., Cheltenham, **2002**; p 347.
32. Cornell, R. M.; Schwertman, U. *The Iron Oxides: Stucture, Properties, Reaction, Occurences and Use Second Edition*, Wiley VCH GmbH&Co., **2003**.
33. Rochester, C. H.; Topham, S. A. *J. Chem. Soc., Faraday Trans. 1*, **1979**, *75*, 1073.
34. Barron, V.; Torrent, J. *J. Colloid Interface Sci*., **1996**, *177*, 407.
35. (a) Curie, P. *Bull. Soc. Fr. Mineral Cristallogr*, **1885**, *8*, 145. (b) Wulff, G. Z. *Kristallogr*, **1901**, *34*, 449.
36. Marcano, D. C.; Kosynkin, D. V.; Berlin, J. M.; Sinitskii, A.; Sun, Z. Z.; Slesarev, A.; Alemany, L. B.; Lu, W.; Tour, J. M. *ACS Nano*, **2010**, *4*, 4806.
37. (a) He, H.; Klinowski, J.; Forster, M. A. *Chem. Phys. Lett.*, **1998**, *287*, 53. (b) Uhl, F.; Wilkie, C. *Polym. Degrad. Stab.*, **2004**, *84*, 215. (c) Stankovich, S.; Piner, R.; Chen, X.; Wu, N.; Nguyen, S.; Ruoff, R. *J. Mater. Chem.*, **2006**, *16*, 155.
38. Hontoria-Lucas, C.; López-Peinado, A. J.; López-González, J. de D.; Rojas-Cervantes, M. L.; Martín-Aranda, R. M. *Carbon*, **1995**, *33*, 1585.
39. Yeh, C. N.; Raidongia, K.; Shao, J. J.; Yang, Q. H.; Huang, J. X. *Nat. Chem.*, **2015**, *7*, 166.
40. Feng, L. L.; Zhang, C. L.; Gao, G.; Cui, D. X. *Nanoscale Res. Lett.*, **2012**, *7*, 276.
41. Tang, L. B.; Li, X. M.; Ji, R. B.; Teng, K. S.; Tai, G.; Ye, J.; Wei, C. S.; Lau, S. P. *J. Mater. Chem.*, **2012**, *22*, 5676.
42. Moustafa, S. F.; El-Badry, S. A.; Sanad, A. M.; Kieback, B. *Wear*, **2002**, *253*, 699.
43. Rohatgi, P. K.; Ray, S.; Liu, Y. *Int. Mater. Rev.*, **1992**, *37*, 129.

44. (a) Kováčik, J.; Emmer, Š.; Bielek, J.; Keleši, L. *Wear*, **2008**, *265*, 417. (b) Emmer, Š.; Havalda, A.; Bielek, J. *J. Phys. IV*, **1993**, *3*, 1799. (c) Whitehouse, A. F.; Warwick, C. M.; Clyne, T. W. *J. Mater. Sci.*, **1991**, *26*, 6176. (d) Kúdela, S.; Schweighofer, A.; Kunkela, J. *Compos. Manuf.*, **1992**, *1*, 43. (e) Prakasan, K.; Seshan, S. *J. Mater. Sci.*, **1999**, *34*, 5045.
45. Qin, B.; Zhao, Y. B.; Li, H.; Qiu, L.; Fan, Z. *Chinese J. Catal.*, **2015**, *36*, 1321.
46. Liu, Z.; Chiang, C.-Y.; Li, W.; Zhou, W. Z. *Chem. Commun.*, **2015**, *51*, 9350.

Chapter 5. Non-Classical Crystal Growth of Rhombohedral Calcite, RHO-type ZIF and Snowflake-like Hematite

This chapter covers the microstructural characterisation of a range of materials with interesting properties that are highly desirable in industry. By uncovering their true, non-classical growth mechanisms, this work provides further evidence that the classical growth theories are often not applicable for a range of synthetic systems and allows the possibility of manipulating the materials' properties to enhance their functionality in industry.

5.1 Rhombohedral Calcite, $CaCO_3$

5.1.1 Introduction

Calcium carbonate, $CaCO_3$, is an interesting material which is highly abundant in nature, making up approximately 4% of the Earth's crust (1) and can be found as different polymorphs with calcite, aragonite and vaterite being the most common (2). $CaCO_3$ also has many industrial applications ranging from paper, plastics and rubbers to adhesives and even medicines (3). As a result of its wide use in both nature and industry, there have been many investigations into the crystal growth of $CaCO_3$, particularly in the presence of organic molecules such as amino acids (4) and biopolymers (5), as control of the growth of $CaCO_3$ crystals may allow more careful control of their final morphology and, therefore, their properties.

This research investigates the growth of rhombohedral calcite crystals over time, using chitosan as an organic structure-directing agent. Chitosan was selected since it has a large number of negatively charged functional groups under working conditions due to its isoelectric point of 6.8-7.4 (6). Since this property is similar to that of the extensively studied extracellular polymeric substances (EPS), which play an important role in biomineralisation, it is expected that the chitosan may enhance aggregation of precursor molecules and calcium cations in the early stages of crystal growth.

This work uncovers a new example of the reversed crystal growth mechanism whereby polycrystalline $CaCO_3$ first aggregates into irregular particles and then the surface of these aggregates undergoes re-crystallization to form a single crystalline shell. Finally, the crystallization extends from the surface to the core, forming true single crystals.

5.1.2 Synthesis

This synthesis was carried out by a third year mini-project group: Angus Ritchie, Michael Watson, Robin Turnbull, Zhengzhong Lu, Michael Telfer, and Jerome Gano. My role in this part of the research is mainly in the microscopic characterization and analysis of the results.

15 ml of distilled water was heated to 60 °C and stirred constantly as 1.00 g high molecular weight (HMW) chitosan (Aldrich) was added. A gel formed after 10 min at which point 23.6 g (0.1 mol) hydrated $Ca(NO_3)_2$ (99%, Alfa Aesar) and 12.0 g (0.2 mol) urea (Alfa Aesar) were added. The solutions were stirred until homogenous and then were sealed in PTFE bottles and heated in an oven to 100 °C. In order to analyse the growth of the particles over time, samples were removed from the oven after different incubation times of 45, 60, 120 and 240 min as well as three samples which were left for longer increments of 1, 2 and 9 days. Once removed from the oven the solutions were centrifuged at 4000 rpm using a Fischer Scientific AccuspinTM 3 to separate the $CaCO_3$ crystals from any chitosan that had not dissolved. The samples were finally dried at 60 °C overnight.

5.1.3 Results and Discussion

In order to determine the growth mechanism of $CaCO_3$ crystals in the presence of an organic, structure-directing agent (chitosan), specimens were synthesized over a range of crystal growth times. It was found that after 45 min of incubation, some very large irregular particles with smooth surfaces had formed (Figure 5.1.1a). EDX analysis of the particles at this stage demonstrated that they contain principle elements of calcium, carbon, nitrogen and oxygen (Figure 5.1.1b). These particles have a very low crystallinity (as can be observed from the XRD pattern shown in Figure 5.1.3a) and are most likely composed of chitosan, calcite and precursor $Ca(NO_3)(H_2O)_3$ molecules.

As the growth time was increased, calcite crystals displaying their typical rhombohedral morphology were found to grow directly on the surface of these chitosan/precursor particles (Figure 5.1.1c) with the amount of $CaCO_3$ crystals on the surface increasing with the reaction time. This confirms that the chitosan plays a part in enhancing the aggregation. This is likely to be due to the polar –OH and $–NH_2$ functional groups of the polymer which may attract the (001) surface of calcite. There is a strong dipole moment normal to the (001) surface in the calcite structure due to the considerable gap that exists between the Ca^{2+} and CO_3^{2-} layers along the c-axis (due to large size of the CO_3^{2-} groups). Although calcite has an overall neutral charge, simulations have been performed which have demonstrated that oligomers of polystyrene sulfonate will preferentially bind to the polar (001) surface rather than the non-polar (104) surface and so a similar effect is likely to be taking place here (7).

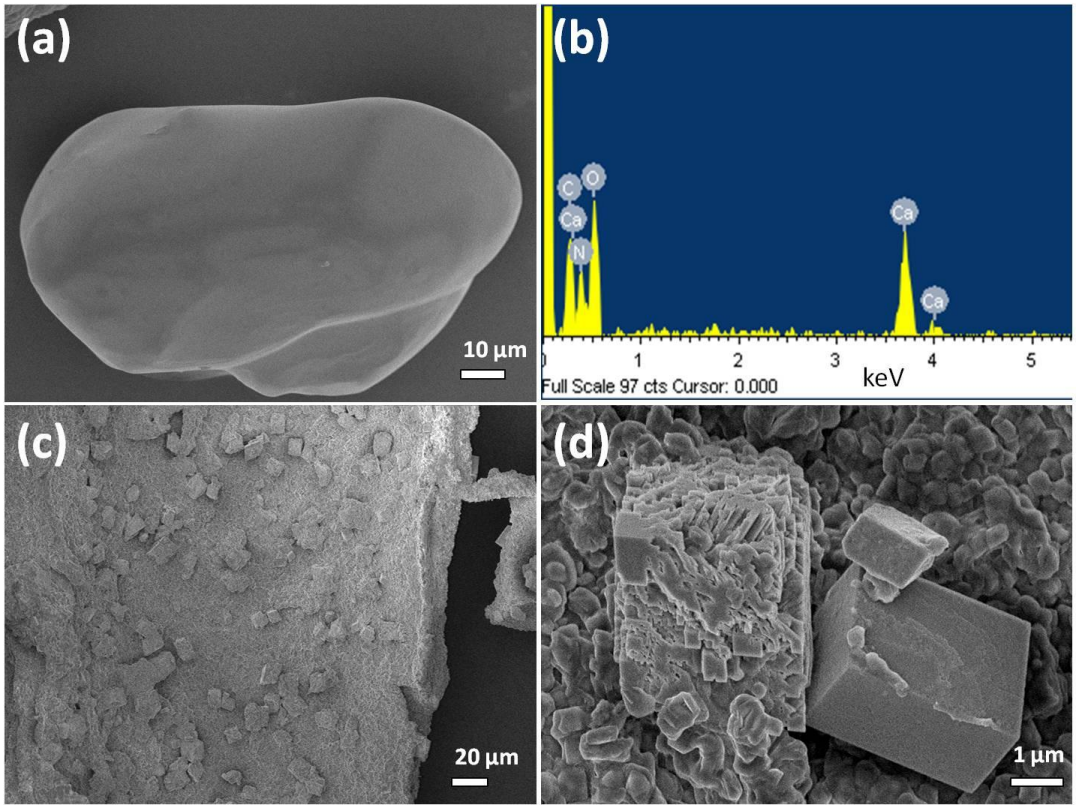

Figure 5.1.1. (a) SEM image showing large aggregates formed after 45 min incubation with (b) displaying the corresponding EDX pattern. (c) SEM image showing the growth of calcite crystals on large organic chitosan particles after a growth time of 4 h. Image (d) shows a higher magnification image of the $CaCO_3$ crystals from the 4 h synthesis shown in (c).

Figure 5.1.2 displays SEM images of the typical morphologies of calcite crystals obtained as the growth time was extended. After a short reaction time of just 1 h, small, quasi-spherical $CaCO_3$ aggregates formed with a typical diameter of about 8-10 μm (Figure 5.1.2a). When the incubation period was increased to 2 h (Figure 5.1.2b and 5.1.2c), the small aggregates start to form a rhombohedral morphology although the surfaces remain rough. After 4 h (Figure 5.1.2d), the faces of the rhombohedra have started to undergo surface recrystallization, forming smooth single crystal faces although the edges and corners remained disordered until the growth time was extended to 24 h (Figure 5.1.2e) which is the first point at which the particles appear to be single crystal like with completely smooth outer surfaces. Despite the single crystal like appearance, it could be the case that the particles at this stage actually have a core-shell structure, i.e. only the surface has undergone recrystallization and the core remains disordered. When the crystals were allowed to grow over a much longer period of 9 days the edges of the crystals appear truncated but the surfaces are still smooth and so the crystals still appear to be single crystalline (Figure 5.1.2f). The fact that the final morphology displays truncated edges implies that the crystals are unhydrated calcite where a residual $\{10\bar{1}1\}$ face is present which would be expected to disappear upon hydration (8).

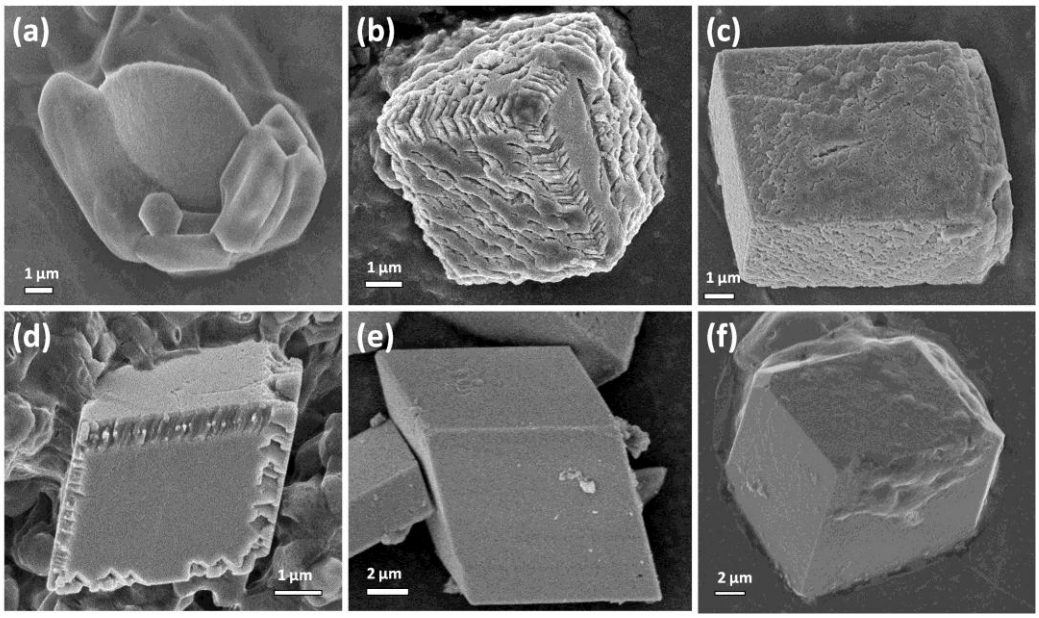

Figure 5.1.2. SEM images displaying the typical morphologies of the $CaCO_3$ crystals after growth times of (a) 1 h, (b, c) 2 h, (d) 4 h, (e) 24 h and (f) 9 days.

PXRD analysis was also performed on the $CaCO_3$ samples to provide additional information on their growth. The resulting PXRD patterns (Figure 5.1.3) of the $CaCO_3$/chitosan samples show that a highly crystalline rhombohedral calcite phase was present in all samples with growth times between 2 h and 9 days. The peaks in Figure 5.1.3 marked C have been indexed to the rhombohedral calcite phase with space group symmetry R-3c and unit cell parameters a = 4.99 Å and c = 17.06 Å. The three peaks that have been marked A could not be indexed to the calcite phase but actually correspond to the (121), (022) and (040) faces of the orthorhombic aragonite phase, which has space group symmetry Pmcn and unit cell parameters a = 4.962 Å, b = 7.968 Å and c = 5.744 Å. Figure 5.1.4 shows SEM images of the orthorhombic aragonite rods which were observed at all incubation times from 2 h onwards to have grown alongside the rhombohedral calcite crystals.

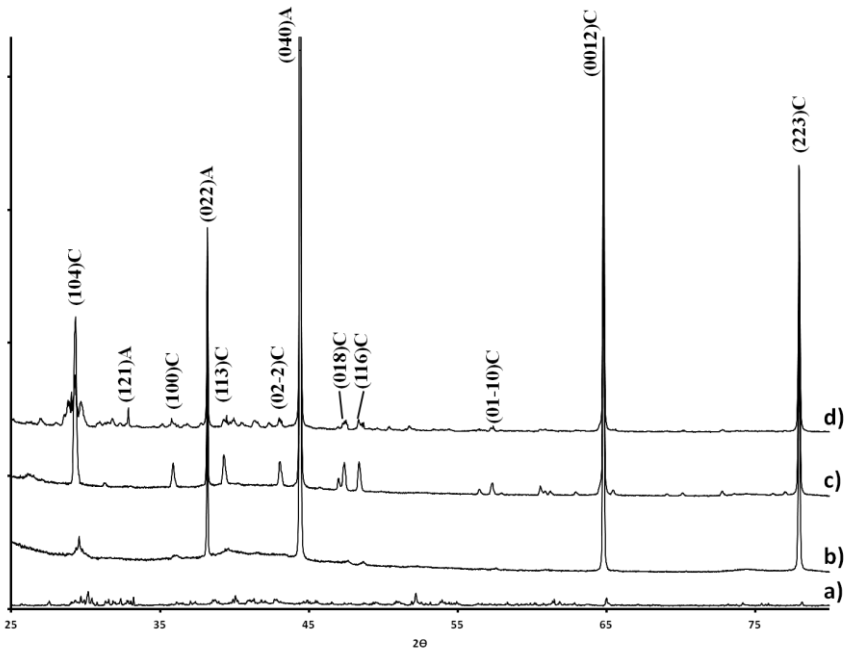

Figure 5.1.3. PXRD patterns of the $CaCO_3$/chitosan samples at growth times of a) 1 h, b) 2 h, c) 24 h and d) 9 days. Peaks have been assigned to the rhombohedral calcite phase (marked C) and orthorhombic aragonite phase (marked A).

The perfect morphology of the $CaCO_3$ rhombohedra from a growth time of 24 h onwards could easily lead to the assumption that they grow via the 'bottom-up' crystal growth mechanism as this classic, well-established, theory can explain this morphology without difficulty. The BFDH Law (9) and Hartman-Perdok theory (10) describe how a

single crystal grows due to kinetic factors, with different growth rates along different orientations resulting in a final morphology with faces which correspond to those with the slowest growth rates (as the faster ones will grow out). As a result of this, the most stable morphology of a calcite crystal would indeed be a rhombohedra with six {104} faces. This growth mechanism, however, assumes that the crystallization starts at the core of the particles and extends outwards and also that the particles are always single crystalline at any growth stage. It is clear that this is not the case in the present work where polycrystalline aggregates are observed to be the first stage in the growth process and where the crystallization occurs after a rough rhombohedral morphology is already observed.

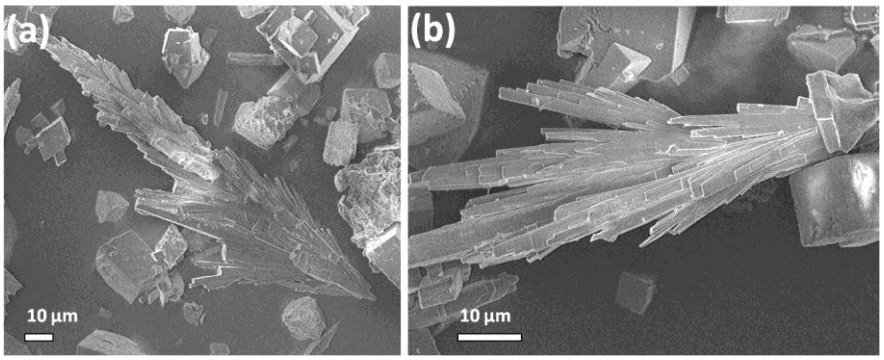

Figure 5.1.4. SEM images showing aragonite rods present in the samples alongside the calcite crystals. These images are from the 24 h sample.

Instead, an alternative growth mechanism must be considered. The classic crystal growth theory only takes kinetic factors into account when explaining the crystallization process. If thermodynamic factors are also considered, however, the equilibrium shape of a free crystal can be said to be the shape which minimizes its surface free energy, regardless of the growth rates of the different faces. This approach was first established by Curie and Wulff, also over a century ago (11). The rough, non crystalline, nature of the calcite particles at early growth stages in the present work shows that the rhombohedra formed before any surface crystallisation was apparent. This is completely opposed to the kinetically-driven classic theory (whereby each atomic layer is deposited sequentially) but could be driven by a reduction in the overall surface free energy as described by Curie and Wulff.

Figure 5.1.5a shows a high resolution SEM image of the rhombohedral calcite particle shown in Figure 5.1.2c which has been grown over 2 h. At this magnification it can be seen

that the ‘rough’ look of the surface is actually due to a number of different crystalline regions, or ‘islands’, which have not fully joined together. This effect is still apparent after 4 h although the crystalline regions are larger and more ordered (Figure 5.15b). By 24 h the many crystalline regions have joined together to form a smooth surface (Figure 5.15c).

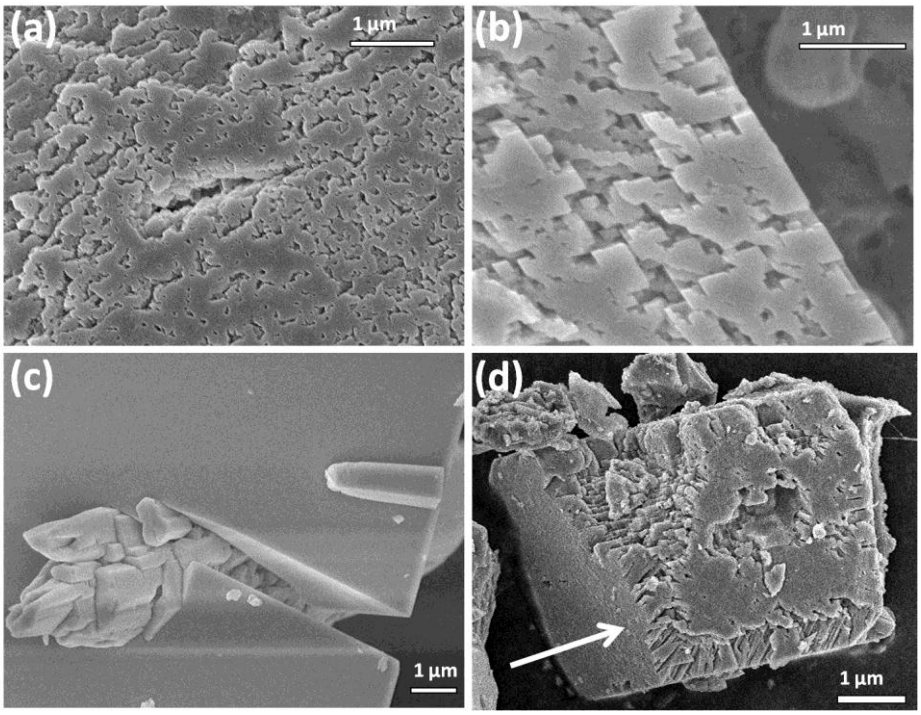

Figure 5.1.5. High magnification SEM images showing the change in the crystal surface from 2 h (a) to 4 h (b) to 24 h (c). Image (d) shows a crushed open particle after a 24 h growth period revealing a disordered core encased in a thin layer of single crystal. The arrow in (d) indicates the thin, single crystal, outer layer.

The image shown in Figure 5.1.5c shows a small gap in the otherwise flawlessly smooth surface of the particle, revealing that at least some of the core material cannot be single crystalline. To further investigate this, the 24 h sample was crushed and additional SEM images were taken (Figure 5.1.5d). It was observed that the inner material of the rhombohedra was actually still disordered polycrystalline which was encased in a very thin layer of single crystal. The arrow in Figure 5.1.5d points to the thin, smooth, outer layer of single crystal which encases the disordered core. These images show that the calcite particles definitely do not follow the classical ‘bottom-up’ growth route as their surfaces have undergone crystallization first while their cores remain disordered.

This so-called ‘core-shell structure’ has been observed in other materials where ‘reversed crystal growth’ was found to be their true growth mechanism (12-16). In order for the calcite crystals to follow the complete reversed crystal growth route, the crystallization should now continue from the surface to the core of the particles, until complete single crystals are formed. To establish whether this was the case in the present work, the crystals were allowed to grow for a much longer period of 9 days and were then crushed open to reveal their inner microstructure. Figure 5.1.6 shows the results of this, where it can be seen that the particles now have an entirely single crystalline cross-section.

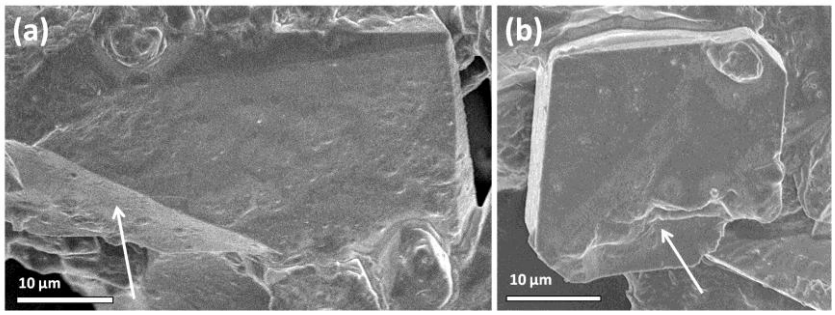

Figure 5.1.6. SEM images of crushed open 9 day samples with arrows indicating the single crystal cross-section.

Summary of the Growth Mechanism

Upon investigation of the crystal structure and morphology of $CaCO_3$ crystals grown in the presence of chitosan over a range of growth times, it can be clearly seen that they do not grow via a classical route (with single nucleation). Instead, a new growth mechanism can now be proposed based on the data collected thus far. This new mechanism is illustrated in the schematic below (Figure 5.1.7).

First, small particles of $CaCO_3$ aggregate directly on the surface of larger clusters, which are a composite of the organic polymer chitosan and the inorganic precursor molecules/ions (Figure 5.1.7a). These aggregates are quasi-spherical and are roughly 8-10 µm in diameter. As the growth time is extended to 2 h, the aggregates start to form the rhombohedral structure typical of calcite crystals although their surface and core remain rough and disordered (Figure 5.1.7b). Small crystalline regions or islands start to form on the surface of the aggregates (Figure 5.1.7c), gradually joining together to completely cover the

faces of the particles and then the edges and corners until eventually the whole outer surface is smooth single crystal (after a growth time of 24 h). At this point the core is still disordered (Figure 5.1.7d) but as the growth time is increased even further the crystallization extends from the surface inwards to the core until eventually the whole particle is a single crystal (Figure 5.1.7e).

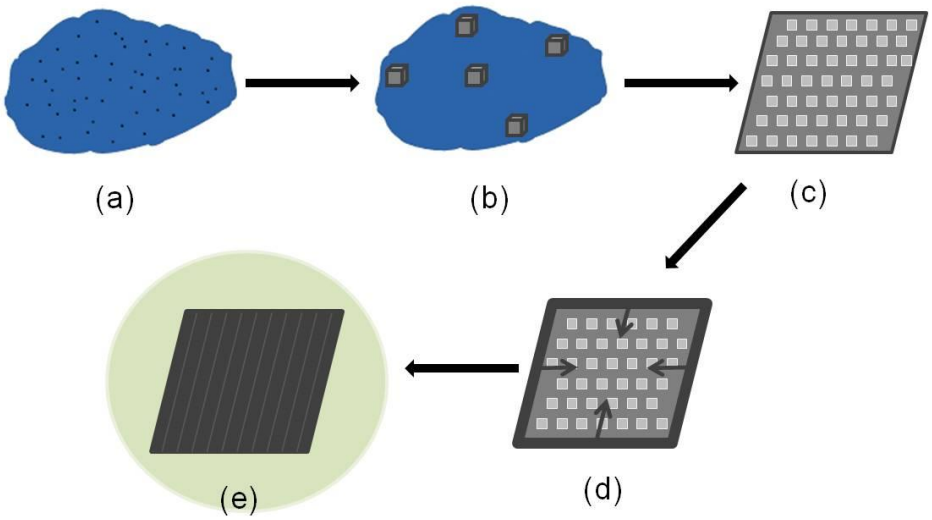

Figure 5.1.7. Illustration of the growth mechanism of rhombohedral calcite crystals. This mechanism follows that of the 'reversed crystal growth' route. a) Small $CaCO_3$ particles aggregate on the surface of polymer/inorganic clusters. b) The $CaCO_3$ particles grow larger over time and take on a cubic morphology. c) The cross section of one of the grey particles from b), showing the true, core-shell nature of the particles after surface recrystallization. d) The crystallization then extends from the surface to the core over time, until e) eventually complete single crystals are formed.

5.1.4 Conclusions

In conclusion, when aggregation dominates in the early stages of crystal growth in a solution, the environment for free crystal growth is disturbed, preventing growth via the classic (single nucleation) route. In reversed crystal growth, it is often the presence of large organic polymers or agents that cause the disruption to the growth environment.

In the case of the rhombohedral calcite particles, it was the presence of chitosan that caused this effect as the polar –OH and $–NH_2$ terminating groups on the organic molecules attracted the Ca^{2+}-terminated {001} surfaces of the early stage nanoparticles, hence

preventing their growth from following a classic route. Instead, the surface of the aggregates became their most active crystallization site, leading to the formation of a 'core-shell' structure consisting of a thin layer of single crystal that encased a disordered core. This investigation of biomimetic crystal growth of $CaCO_3$ crystals, with chitosan as the organic structure directing agent, has revealed a new example of the reversed crystal growth mechanism.

5.2 Zeolite Imidazolate Framework, RHO-ZIF

5.2.1 Introduction

Metal-organic frameworks (MOFs) are highly porous solids generally obtained through solvothermal synthesis (17). They consist of metal-containing inorganic clusters joined by organic linkers and have been of high interest recently due to their large range of potential applications in areas such as gas storage (18), catalysis (19), chemosensing (20) and drug delivery (21). The catalytic activity of MOFs can be even further improved by the addition of catalytically active metals such as Pt, Ag, Au, Cu, Ru and Pd into the MOF cavities (22).

Zeolitic imidazolate frameworks (ZIFs) are a sub-class of MOFs that have exceptionally high thermal and chemical stabilities and high surface areas and so are extremely promising for absorption applications (23). ZIFs are composed of metal cations tetrahedrally-coordinated by imidazolate linkers and have distinct topologies dependant on the linkers used. In the present work, a relatively new ZIF, developed at the University of St Andrews in 2012 (24), is synthesized that has both purinate (*pur*) and 2-nitroimidazolate (*nim*) acting as the linkers between zinc cation centres and has the chemical formula $Zn_{1.33}(O.OH)_{0.33}(nim)_{1.167}(pur)$. Mixed linker ZIFs (i.e. those with more than one ligand) are able to form structures that would not be possible with a single linker, where the kinetic stability of the final structure is a direct result of the linker combinations (25). The *pur* ligand is usually responsible for forming the LTA topology (26) but the inclusion of the second, *nim*, ligand interrupts the link-to-link interactions and instead causes the formation of the GME or RHO topologies depending on the zinc source (24). In the present case, zinc nitrate is used as the metal source and so this ZIF adopts a RHO-type topology, similar to that of the well-studied, single linker, ZIF-11 ($Zn(bzim)_2$), and so will be referred to during this work as

'RHO-ZIF'. In this type of structure, each supercage is connected to six others through eight-membered rings (Figure 5.2.1). The central supercage is not connected to any of its nearest-neighbour supercages, which are located by its diagonal six-membered rings, but instead to six others further away via the eight-membered rings (shown in blue in Figure 5.2.1a). This means that there are two interpenetrating (but not connected) arrays of supercages throughout the structure.

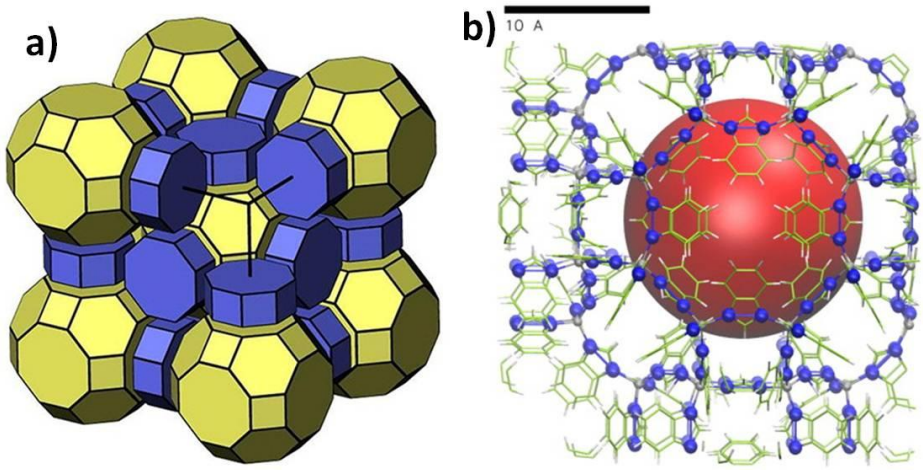

Figure 5.2.1. (a) The RHO-type topology. Adapted from Ref. 27 with permission from the American Chemical Society. (b) Structural model of ZIF-11 viewed through one of the connecting eight-membered rings. Reproduced from Ref. 28 with permission from Elsevier Ltd.

Reversed Crystal Growth of MOF-5

Many MOF and ZIF crystals appear to be single crystals due to their perfect outer appearance and highly symmetric polyhedral morphology. Their growth, therefore, has often been assumed to follow the classical, 'bottom-up', route and so goes unstudied. This classical crystal growth theory, which was established over a century ago and is described by the Bravais-Friedel-Donnay-Harker (BFDH) law (9), Ostwald ripening (29) and Hartman-Perdok theory (10), describes the growth of free crystals from a single nucleus via layer by layer deposition of the building units. This has been proven to not always be the true growth route, however, as in the case of MOF-5 which was shown to follow a reversed crystal growth mechanism instead by the Zhou group in 2013 (30).

MOF-5 consists of $[Zn_4O]^{6+}$ clusters arranged in octahedral sub-units that are connected through 1,4-benzenedicarboxylate (1,4-BDC) linkers. Despite being of particularly high interest due to its ability to store hydrogen at low temperatures and moderate pressures (31), knowledge of the crystal growth of MOF-5 was very limited until the 2013 study and so the crystals were assumed to grow via the classical route since their seemingly perfect cubic morphology was a direct reflection of the cubic structure. Through a step by step study of the crystal growth over time, however, the Zhou group disproved this assumption and revealed the true, non-classical mechanism (Figure 5.2.2).

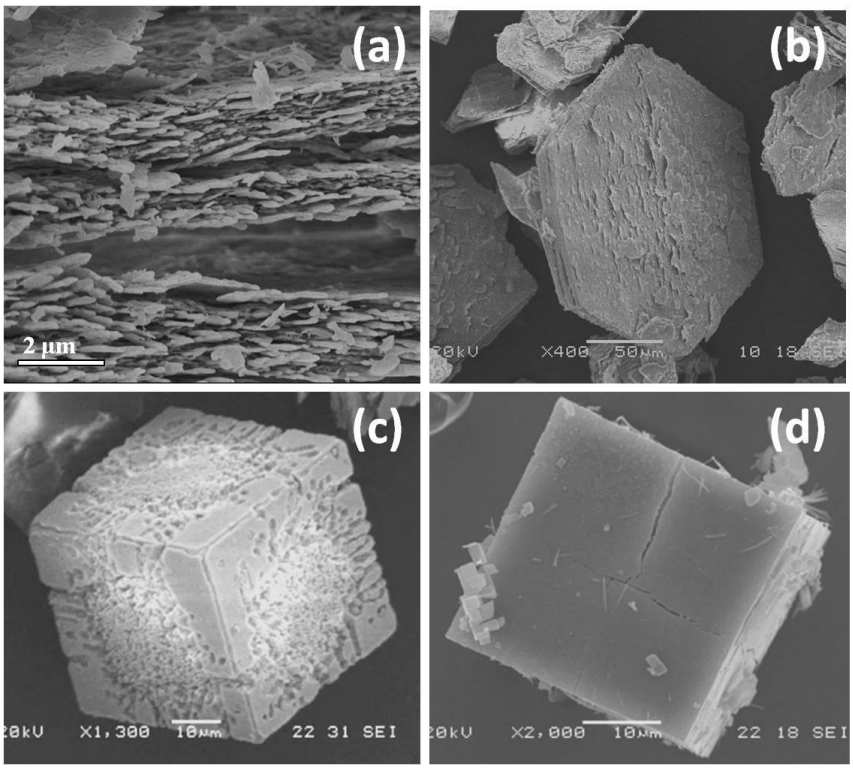

Figure 5.2.2. SEM images showing some of the different stages in the crystal growth of MOF-5 after incubation periods of (a) and (b) 6 h, (c) 8 h and (d) 22 h. Adapted from Ref. 30 with permission from The Royal Society of Chemistry.

It was discovered that the first step in the growth process was actually the formation of microplates of monoclinic $Zn_5(OH)_8(NO_3)_2.2H_2O$ that were around 5 to 10 nm in diameter and which aggregated with surface adsorbed organic molecules to form layered inorganic-organic composites after 6 h (Figure 5.2.2a and b). Nucleation of MOF-5 nanocrystallites then took place within these composites via a phase transformation of $Zn_5(OH)_8(NO_3)_2.2H_2O$

and intercalation of the 1,4-BDC linker molecules. As the growth time was increased, the nanocrystallites aggregated into cubic polycrystalline particles which then underwent surface re-crystallization so that a thin layer of single crystal formed at the corners and edges of the cube around 8 h (Figure 5.2.2c). The recrystallization then extended across the faces of the cube until, eventually, the entire particle had a single crystalline surface encasing the polycrystalline core by 22 h (Figure 5.2.2d). Finally, after a much longer growth period of 96 h, the crystallisation had extended from the surface to the core resulting in true, cubic, single crystals.

This reversed crystal growth mechanism, first reported in 2007 for the zeolite analcime (12), has been found to be the true growth process of many materials which had previously been believed to follow the classical route. Examples include metals and metal oxides (16, 32), perovskites (33), organic crystals (6) and many others (13-15). Through these studies it has become apparent that the aggregation of precursor molecules/ions at an early stage is the key step for reversed crystal growth. Synthetic solutions for MOFs always contain a combination of inorganic and organic precursors, which generally have strong interactions between them. This would enhance fast aggregation before individual free crystals are developed and so leads to reversed crystal growth.

The wealth of potential applications of such a material makes it essential to be aware of the mechanism by which RHO-ZIF crystals grow as only by truly understanding their growth can we tailor their morphology to maximise the desirable properties. Herein, the growth of highly symmetric crystals of the Zn-based RHO-ZIF is studied over time, uncovering a new example of a material which follows a non-classical crystal growth mechanism and giving a deeper understanding of the ZIFs properties.

5.2.2 Synthesis

The synthetic procedure used in this work was adapted by that previously reported by Kahr *et al.* (24). 219.5 mg zinc nitrate hexahydrate (98% Fisher Scientific), 119 mg 2-nitroimidazole (98%, Fluorochem) and 120.1 mg purine (Endotherm) were dissolved, by stirring, in 15 mL dimethylformamide, DMF (99%, Acros Organics). 0.5 mL methanol was added to the solution which was then sealed in a 50 mL Teflon-lined autoclave and incubated at 100 °C for a range of growth times between 1 h and 6 weeks. The resulting precipitate was

collected via centrifugation and washed several times with methanol. Finally, the powder was dried in an oven at 60 °C overnight.

5.2.3 Results and Discussion

The growth of RHO-ZIF crystals was initially studied over time using SEM analysis. It was found that at the earliest growth time of 1 h, particles with an average diameter of approximately 500 nm appeared, forming some loose clusters (Figure 5.2.3a) which start to aggregate into larger particles, some even displaying a pseudo rhombic dodecahedral shape by 3 h (Figure 5.2.3b). This is not the first time the existence of polycrystalline particles with a highly symmetric polyhedral morphology has been observed, which cannot be explained by the classical theories of polyhedral formation in crystal growth. This occurrence can probably be attributed to an interaction between the nanocrystallites. However, more experiments and theoretical studies must be done before the mechanism can be fully understood.

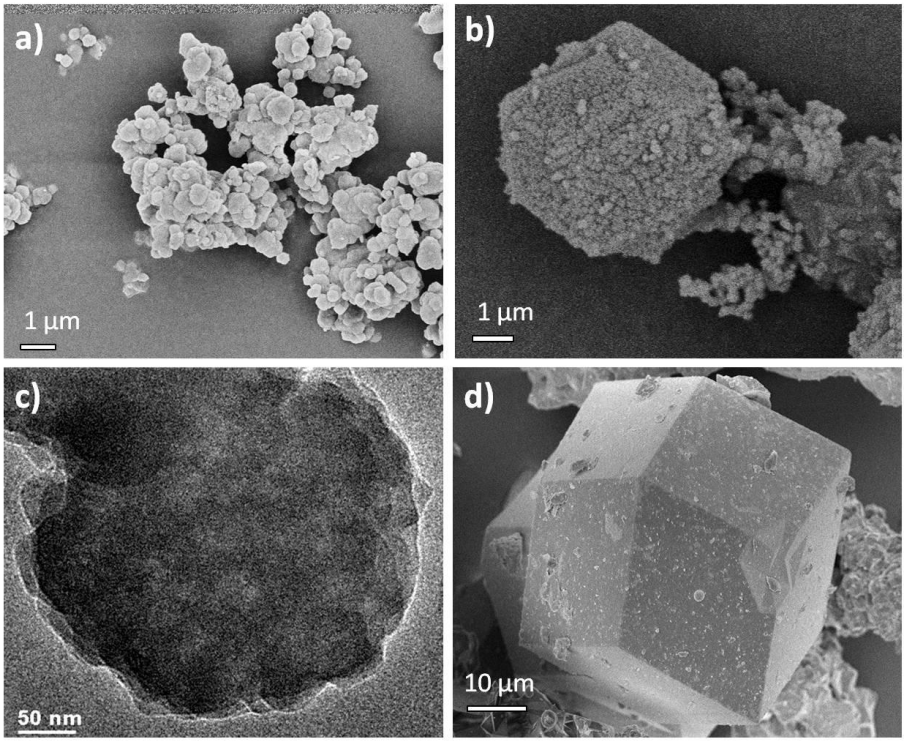

Figure 5.2.3. TEM and SEM images of the specimens during the growth of RHO-ZIF crystals with different incubation times of a) 1 h, b,c) 3 h and d) 3 weeks. The SEM image in a) was recorded by Michael Telfer.

PXRD analysis (Figure 5.2.4) revealed that these aggregates already display phases of low crystallinity that can be indexed to the cubic phase $Zn_{1.33}(O.OH)_{0.33}(nim)_{1.167}(pur)$ (i.e. RHO-ZIF), which has the space group $Im\bar{3}m$ and unit cell parameter a = 29.044 Å.

It is known that crystal nucleation in ZIFs can be caused via the addition of a nonsolvent (i.e. a substance that is incapable of dissolving the ZIF), creating an environment in which the reactants are unstable (25). In this case, methanol was added into the solution, reducing the stability of the reactants (34) and causing the precipitation of products at very short reaction times, hence why RHO-ZIF particles can be produced in as little as 3 h.

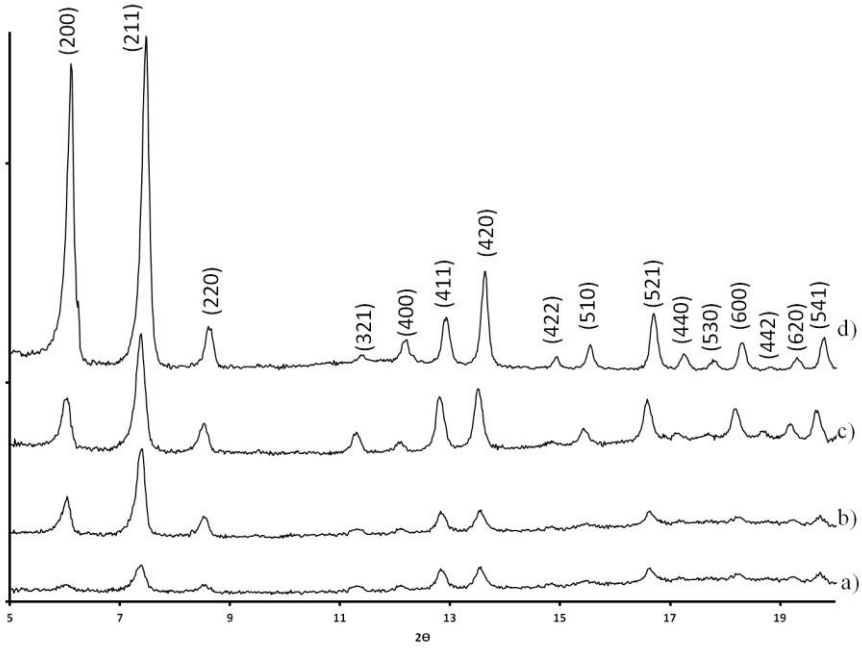

Figure 5.2.4. PXRD patterns of RHO-ZIF samples grown over a) 3 h, b) 24 h, c) 3 weeks and d) 6 weeks. The reflections in (d) are indexed to the cubic $Zn_{1.33}(O.OH)_{0.33}(nim)_{1.167}(pur)$ phase.

It was revealed that the individual spherical particles, 500 nm in size, as shown in Figure 5.2.3a, were not single crystals. The TEM image displayed in Figure 5.2.3c shows a typical spherical particle from the 3 h sample, showing the nature of aggregation of smaller particles. It can be seen that the density of the aggregate is not uniform by the varying contrast in the image (the darker the region, the greater the mass-thickness). Unfortunately,

due to the presence of organic components within the RHO-ZIF structure (causing it to break down under the high intensity electron beam) it was extremely difficult to attain any high resolution TEM (HRTEM) images or selected area electron diffraction (SAED) patterns to confirm the crystallinity of these nanoparticles and to demonstrate whether or not they were disordered. Using the Scherrer equation (35), however, the average size of crystallites in the 3 h sample was determined from the corresponding XRD pattern to be approximately 35 - 40 nm (calculated from the (211), (411) and (420) peaks), which appears to match with the TEM images taken. This result indicates that the first step in the formation of RHO-ZIF crystals is disordered aggregation of precursor molecules. Multiple nucleation and early stage crystal growth then took place inside these amorphous soft matter aggregates instead of developing free crystals in the synthetic solution.

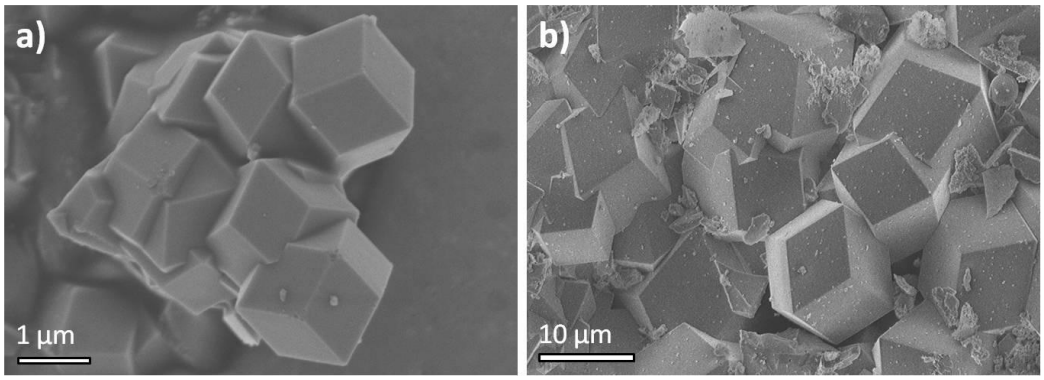

Figure 5.2.5. SEM images displaying intergrowth of ZIF structures grown over a) 2 days and b) 6 weeks.

Finally, after an incubation period of 3 weeks (Figure 5.2.3d) the crystals appeared to have a perfect polyhedral appearance, resembling that of a single crystal, displaying their final, rhombic dodecahedral morphology with a size range from 15 µm to 50 µm. This morphology, with 12 exposed {110} facets, is typical for ZIFs with the RHO topology. The intensity of the (110) peak for the RHO-ZIF, however, is too low to be observed which is not the case for other ZIFs with the same topology. This is due to the presence of the two different linkers in the RHO-ZIF structure. In the RHO framework type, there are two individual linker sites, which exist in a 1:1 ratio, connecting the supercages. In single-linker ZIFs, such as ZIF-11, both sites are occupied by the same linker whereas in the RHO-ZIF the *nim* ligands occupy one site and the *pur* ligands occupy the other, increasing the symmetry of

the framework topology from primitive, P, to body centered, I, which decreases the intensity of the (110) peak and causes the intensity of the (220) to increase instead (24).

The intensity of the peaks in the PXRD patterns increased with growth time (Figure 5.2.4), indicating an increase in the crystallinity of the RHO-ZIF particles. A shoulder can be observed in the (200) peak at the longest growth time (Figure 5.2.4d) which is likely to be a result of two peaks overlapping due to a lattice distortion caused by the intergrowth, or interpenetration, of frameworks within the ZIF structure, evidence of which was observed in the current work across a range of growth times (Figure 5.2.5). This interpenetration is allowed for many high symmetry topologies and is frequently observed in MOFs and ZIFs when long linkers (such as those used in the current work) are employed (36).

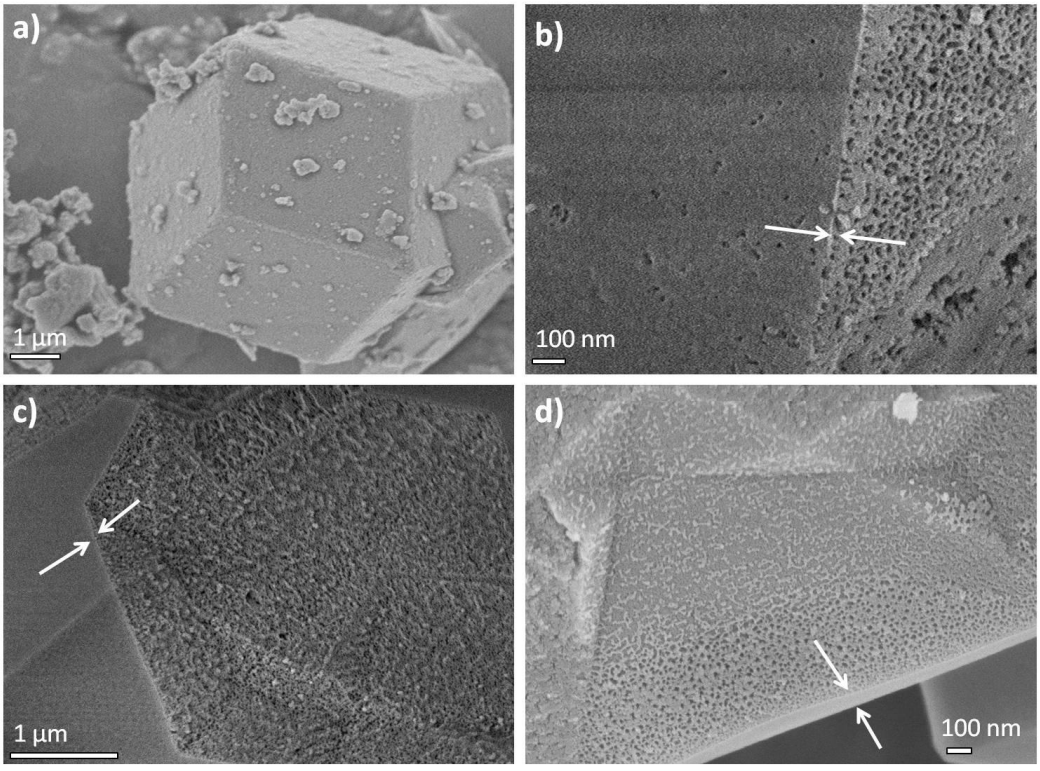

Figure 5.2.6. (a) SEM image of a typical RHO-ZIF particle at 24 h. SEM images also shown of crushed particles grown over b) 24 h, c) 4 days and d) 7 days. The arrows in b), c) and d) indicate the thickness of the outer shell.

When the particles with the seemingly single crystal outer appearance were crushed and studied again, more closely, however, it could be seen that they were not single crystals

at all but actually consisted of a “core-shell” structure where a disordered core is encased in a thin layer of single crystal (Figure 5.2.6). At a growth time of 24 h, the particles already appear single crystal like (Figure 5.2.6a). When these particles are crushed, however, the porous, disordered core can be seen clearly via SEM (Figure 5.2.6b). Moreover, when the outer surface of the particles is more closely examined it becomes clear that even the outer layer is not quite single crystal but is actually still porous (although it appears much denser than the core). This was also observed in cubic, ‘pomegranate-like’, MOF-5 particles where the core and shell were shown to have different tiers of porosity (37). Therefore, the particles are mainly polycrystalline. The average size of crystallites within the 24 h particles has been determined to be around 47 nm from the corresponding XRD peaks (calculated from the (200), (211) and (420) reflections).

The porosity of the 24 h sample was determined via N_2 adsorption at 77 K (Figure 5.2.7). The N_2 adsorption-desorption isotherm displays a Type H_4 hysteresis loop indicating a mesoporous material with narrow, slit-like pores. The material was determined to have a BET surface area of 241 $m^2\ g^{-1}$ with a maximum N_2 uptake of 5.95 mmol g^{-1} and pore volume of 0.094 $cm^3\ g^{-1}$. These values are smaller than those previously reported for $Zn_{1.33}(O,OH)_{0.33}(nim)_{1.167}(pur)$ with the RHO topology, which is likely to be due to the incomplete crystallization process. Kahr *et al*. reported a maximum N_2 uptake of 6.5 mmol g^{-1} (24) which is higher than the 24 h sample in the present work but is still lower than the 10 mmol g^{-1} value that their GCMC (grand canonical Monte Carlo) simulation predicted to be possible. It may be the case, therefore, that the RHO-ZIF crystals they analysed, which were grown over 7 days, were also not fully single crystalline.

When a crystal grown over 4 days was crushed open (Figure 5.2.6c), the distinction between surface and core became more evident. The very thin surface layer (indicated by the white arrows in Figure 5.2.6c) has increased in crystallinity to the point that it now appears single crystalline while the core is still highly disordered. As the growth time was increased further to 7 days (Figure 5.2.6d), the core-shell structure was still apparent but the thickness of the crystalline outer shell had increased as the crystallization is extending from the surface to the core. This is further confirmed by the (200) peak intensity in the PXRD patterns (Figure 5.2.4), which increases significantly over time relative to the other peaks, implying growth along the <200> zone axes. As the outer morphology and size of the crystals did not change significantly over time, this growth (increase in crystallinity) must be occurring chiefly along the inner surface of the single crystal shell where the vertices are the sites which

present the lowest energy. The thickness of the shell, therefore, increases the fastest along the <100> directions but since the (100) peak is a systematic absence for this structure, the intensity of the (200) peak greatly increases over time.

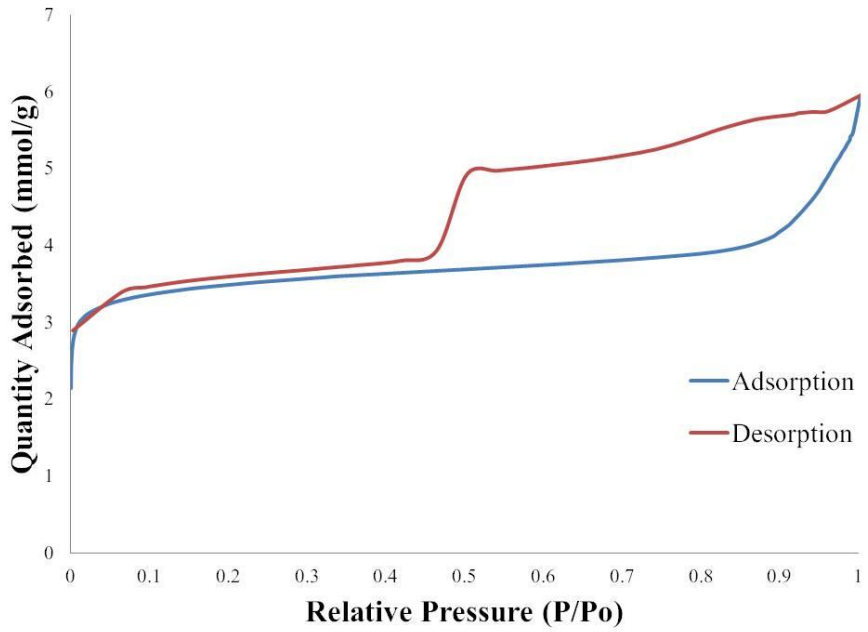

Figure 5.2.7. N_2 absorption-desorption isotherm (77 K) of RHO-ZIF sample grown over 24 h.

Further evidence of the disordered core was observed via TEM analysis. Figure 5.2.8 displays a TEM image of a fragment of a particle from the 48 h sample. The top-right edge (indicated by the arrow) is flat and has a darker contrast, implying that this edge is the shell of the particle. It is evident from the variations in contrast within the lower part of the fragment that it is porous, polycrystalline with a low density. It is noticed that there is no clear line between the shell and the inner particles. Unfortunately, the crystal structure of RHO-ZIF was very sensitive to the electron beam and decomposed almost immediately when the particles were exposed to it. Therefore, it was not possible to obtain SAED patterns or HRTEM images of this structure. This was unsurprising as most MOF and ZIF structures are known to be unstable under electron beam irradiation (38) and generally collapse either partially or completely even when a very low level of electron irradiation is applied.

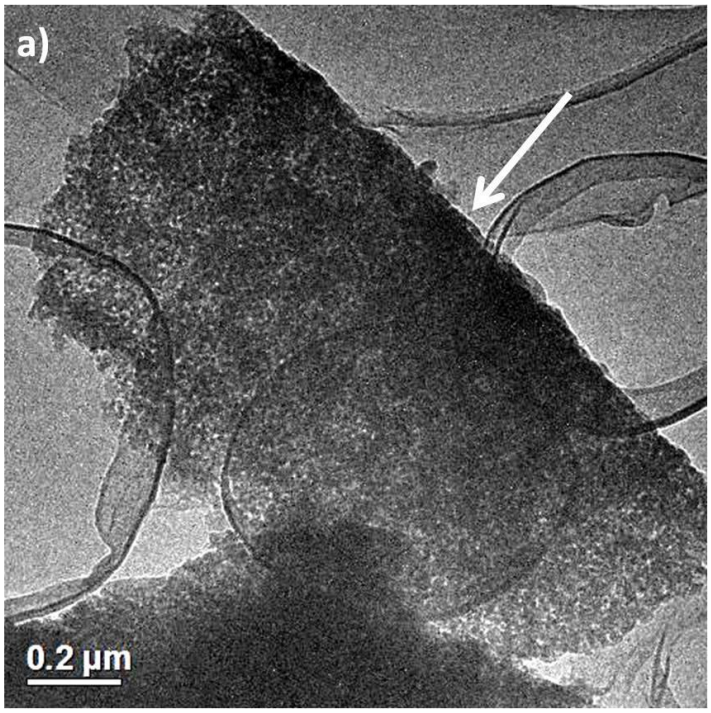

Figure 5.2.8. TEM image of a surface fragment of particle in the 48 h sample displaying the disordered core underneath the dark contrast shell at the top-right edge (indicated by the arrow).

The results presented thus far provide clear evidence that the growth of RHO-ZIF crystals does not follow the classical mechanism, where growth occurs via layer-by-layer deposition on a single nucleus. If that were the case, the crystals would have a single crystal cross-section at all stages in the growth process. In the present work, however, the growth of RHO-ZIF appears to follow the reversed crystal growth mechanism, where the first stage is the formation of disordered aggregates, which then undergo surface recrystallization followed by an extension of the crystallization towards the core, until a true single crystal is eventually formed. The reason this formation of aggregates is favoured is believed to be due to the strong interactions between the precursor molecules/ions. At a very early stage in the development of crystals, two processes are in competition: a process of nucleation followed by growth of free crystals in the solution and a process of aggregation of precursor molecules/ions. When the interaction between precursor molecules/ions is strong, aggregation dominates and the growth of free crystals in solution is suppressed. In the present work, although no long chain structure directing agent was added, the interaction between Zn^{2+} cations with the organic precursors (2-nitroimidazole and purine) is so strong that they join together quickly to form disordered spherical particles before forming crystals (39). The

ratios of the components may not be the same as that of RHO-ZIF, however, and so these nano-spheres undergo further assembly into large aggregates. It is unlikely that nucleation of RHO-ZIF takes place in the solution since the concentrations of the precursors in the solution are significantly reduced. The nucleation of the ZIF can, therefore, only occur within the disordered aggregates. The formation of a single crystal shell arises because the surface of the aggregates offers a large number of active sites for crystallisation.

The extension of crystallisation from the surface to the core is via an Ostwald ripening process and is very slow. Two reasons for this are that the movement of organic molecules within the soft matter cores of the particles is difficult, and also that the construction of the ZIF structure is based on highly selective connections of Zn^{2+} ions with the organic linkers.

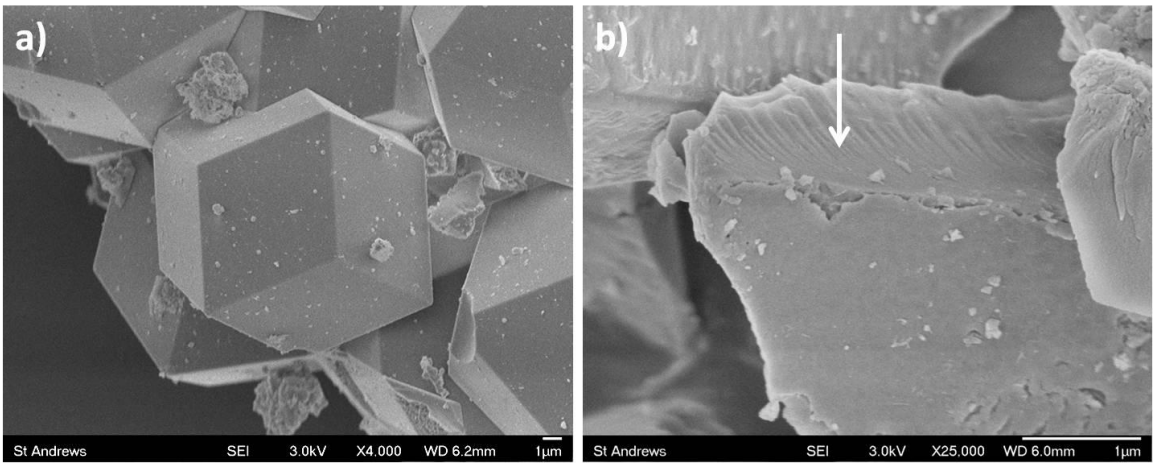

Figure 5.2.9. SEM images of RHO-ZIF crystals in the 6 week sample, (a) showing more regular rhombic dodecahedra, (b) displaying crushed RHO-ZIF particles. The white arrow indicates the single crystal cross-section.

The final stage of reversed crystal growth is the formation of true single crystals and so, in order to determine conclusively that this is the true mechanism for the RHO-ZIF crystals, it is important to find evidence of complete single crystals as the final growth stage. The synthesis was repeated, therefore, with an even longer incubation period of 6 weeks whereupon the PXRD pattern showed crystalline peaks with much higher intensities (Figure 5.2.4). SEM images revealed more regular rhombic dodecahedral particles (Figure 5.2.9a). The particle size did not increase significantly in such a long growth time. When the crystals were crushed and analysed via SEM (Figure 5.2.9b) there were no longer any particles with a

'core-shell' structure observed. Instead, the SEM images showed a single crystal cross-section (as indicated by the white arrow in Figure 5.2.9b).

The porosity of the 6 week sample was determined via N_2 adsorption at 77 K (Figure 5.2.10). The sorption isotherm displays a Type H_4 hysteresis similar to that of the 24 h sample (Figure 5.2.7) although the BET surface area had almost doubled to 417 m^2 g^{-1}, with a pore volume of 0.129 cm^3 g^{-1} and an improved maximum N_2 uptake of 8.45 mmol g^{-1}. This uptake value is now higher than the previously reported literature value and much closer to the 10 mmol g^{-1} value which was predicted to be possible by the GCMC simulation run by Kahr *et al.* (24). This is due to the fact that over the increased growth time, as the particles undergo the transition to become single crystals, they get closer to the simulated structure (Figure 5.2.1a) and become more ordered, increasing the pore volume and N_2 uptake. It is also likely that when the core was more disordered (at the earlier growth stages), there were fewer clear channels through the crystals, prohibiting N_2 diffusion through the structure.

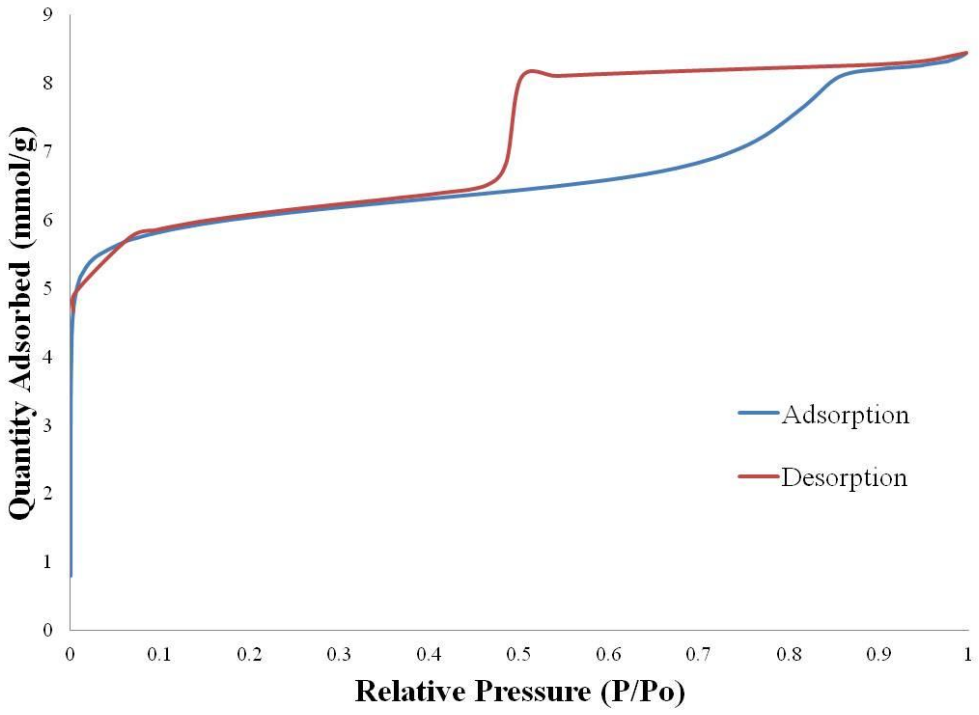

Figure 5.2.10. N_2 isotherm (77 K) of RHO-ZIF sample grown over 6 weeks.

Summary of Growth Mechanism

Using the evidence gathered thus far, it is now possible to propose a new growth mechanism for the RHO-ZIF crystals. Initially, in step 1, precursor molecules/ions form disordered spherical aggregates (Figure 5.2.11a) which then join together, in step 2, to give rise to porous particles with a pseudo-rhombic dodecahedral shape, made up of many embedded nanocrystallites of RHO-ZIF (Figure 5.2.11b). In step 3 (Figure 5.2.11c), the surface of the disordered particles recrystallises into a single crystal shell with a perfect rhombic dodecahedral morphology, while the core remains disordered. In step 4, the recrystallization extends from the surface towards the core (Figure 5.2.11d), and finally a real single crystal state is achieved.

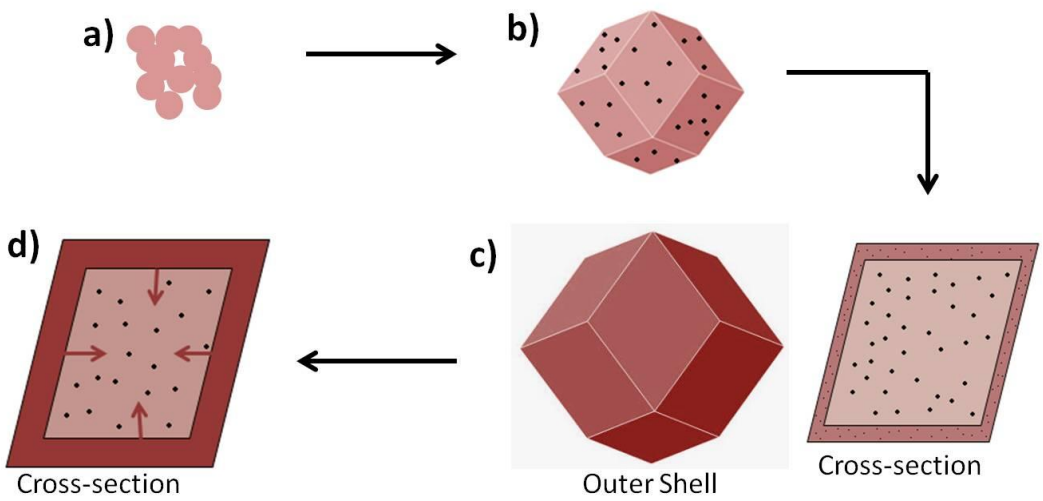

Figure 5.2.11 Schematic of proposed growth mechanism for rhombic dodecahedral RHO-ZIF crystals. a) Disordered precursor materials form spherical aggregates. b) Aggregates join together to form porous pseudo rhombic dodecahedral particles. c) Surface recrystallization occurs, giving rise to a single crystal outer shell encasing a porous core. d) Finally, the crystallization extends from the surface to the core until true single crystals are formed.

5.2.4 Conclusions

The results of this work clearly demonstrate that the classical, "bottom-up" route of crystal growth which was established over 100 years ago, is not always the appropriate explanation for the growth of highly symmetric polyhedral crystals. In the present work, RHO-ZIF has been shown to form rhombic dodecahedral crystals by following a reversed

crystal growth mechanism in which the key step is the aggregation of precursor molecules/ions at an early stage followed by surface recrystallization to form a single crystal shell. It was reported by Curie and Wulff a long time ago that the equilibrium shape of a free crystal is that which minimizes its surface free energy (11). According to this theory, the formation of the rhombic dodecahedral shell can be explained (even though the cores of the particles are still disordered) because a polyhedral morphology minimizes the surface free energy. However, the rhombic dodecahedral morphology of the particles appears before the formation of the single crystal shell. This is not the first example of perfect polyhedral shape of polycrystalline particles and the reason has not yet been fully understood.

Discovering the true, reversed crystal growth, mechanism of RHO-ZIF gives us the opportunity to fine tune the microstructure and produce different morphologies at different growth times. For example, it is possible to fabricate polycrystalline particles with nanocrystallites embedded in an organic matrix, particles with a hierarchical pore system and hollow crystals after removing the disordered core materials etc.

5.3 Snowflake-like Iron Oxide, α-Fe_2O_3

5.3.1 Introduction

Hematite, α-Fe_2O_3, is the most stable form of iron (III) oxide, Fe_2O_3, under ambient conditions, occurring naturally in igneous, sedimentary and metamorphic rocks and is generally mined as the main ore of iron metal (40). It also has a huge range of potential applications in many fields such as environmental protection (41), biomedical devices (42), rechargeable lithium ion batteries (43) and magnetic devices (44). It has become increasingly apparent in recent years that the suitability of hematite for these applications is highly dependent on the morphologies and microstructures of the α-Fe_2O_3 crystals (45). For example, hollow nanospheres of hematite have been synthesized that are shown to be only weakly ferromagnetic (46) whereas hematite crystals presenting dodecahedral and octahedral morphologies were shown to have much stronger magnetism due to the concentration of exposed Fe^{3+} cations on the terminating crystal planes (47).

Highly dendritic, snowflake-like α-Fe_2O_3 crystals have been reported with huge surface areas and unique hierarchical structures (48) but the mechanism by which these

intricate morphologies grow is still poorly understood. It is clear that they do not grow via any of the well-defined classical methods such as BFDH law (9) or the Hartman-Perdok theory (10) as these theories are based on the drive to minimise the bonding and surface energy of crystals whereas a branched snowflake structure with high surface energy is not thermodynamically favourable.

Hematite exists in the corundum (Al_2O_3) structure with a hexagonal close packed array of oxygen atoms and Fe^{3+} ions occupying two thirds of the octahedral sites between O atoms (49). It is commonly reported that α-Fe_2O_3 can be formed through the hydrolysis of $[Fe(CN)_6]^{3-}$ ions which dissociate in aqueous solution to produce Fe^{3+} (50). These metal ions then hydrolyse to form intermediate species such as FeOOH or $Fe(OH)_3$ before finally decomposing to Fe_2O_3 (Equation 5.1).

$$[Fe(CN)_6]^{3-} \rightarrow Fe^{3+} \rightarrow \text{ FeOOH / } Fe(OH)_3 \rightarrow \alpha\text{-}Fe_2O_3 \qquad (5.1)$$

The details of this process, however, are not well studied and the dissociation constant of $[Fe(CN)_6]^{3-}$ in water is actually relatively low (K_d = 1.0 x 10^{-42}), which provides an obstacle towards the free growth of α-Fe_2O_3 crystals in solution. This would support the theory of a deviation from classical growth in which the initial step would generally be the nucleation of seed crystals in solution, followed by layer by layer deposition of atoms on the crystal surfaces.

Herein, the growth of highly dendritic, snowflake-like α-Fe_2O_3 crystals is reported via a hydrolysis process of $[Fe(CN)_6]^{3-}$ where seed crystals of hematite are actually formed within or on the surface of amorphous aggregates of precursor material rather than freely in the aqueous solution. Further growth then occurs rapidly, principally along the <11$\bar{2}$0> zone axes. The growth is first studied over a range of growth times and then further studies are conducted into how the morphology of the hematite crystals changes with pH and with the concentration of $K_3Fe(CN)_6$. Finally, a new mechanism for the non-classical growth route of these snowflake-like crystals is proposed, complementing work recently published by other members of the Zhou research group (51).

5.3.2 Synthesis

This synthesis was mainly carried out by a third year mini-project group: Ashleigh Waller, Ben Walden, Jonathan Marshall, Aron Ruszin, James Webster and Ziyin Niu. Although I was also involved with some of the synthetic work, my role in this part of the research was mainly in the microscopic characterization and analysis of the results.

In a typical synthesis, 13.2 mg (2.0 mM) potassium hexacyanoferrate, $K_3Fe(CN)_6$ (95%, Acros Organics), was dissolved by stirring in 20 ml distilled water, sealed in a 30 mL Teflon-lined autoclave and then heated at 180 °C for a range of growth times between 2 h and 72 h. The resulting red precipitate was then collected via centrifugation and washed with distilled water and ethanol before being dried at 60 °C for 4 h.

Variations on this synthesis were also performed. 48 h samples were repeated using an increased $K_3Fe(CN)_6$ concentration of 10 mM and the 6 h experiment was also repeated several times but with the drop wise addition of octylamine to increase the pH of the solution.

5.3.3 Results and Discussion

Development of morphology over time

The growth of snowflake-like α-Fe_2O_3 crystals at a $K_3Fe(CN)_6$ concentration of 2.0 mM was initially studied over time using SEM analysis (Figure 5.3.1). It was found that, at the earliest growth time of 2 h, seemingly amorphous particles with no discernible morphology were present, aggregated into loose clusters anywhere between 50 – 500 nm in size (Figure 5.3.1a). When the growth time was increased to 3 h there was a distinct change in morphology as all crystals now displayed the branched, snowflake-like structure with six-fold symmetry (Figure 5.3.1b). There was no further obvious change in morphology after this when the growth time was extended to 6 h (Figure 5.3.1c) and even to 72 h (Figure 5.3.1d). The snowflakes maintained an average branch length of around 4 μm.

Through PXRD analysis, it was revealed that the particles could be indexed to trigonal α-Fe_2O_3 at all growth times (Figure 5.3.2) with space group $R\bar{3}c$ and unit cell parameters a = 5.038 Å and c = 13.772 Å. This led to the conclusion that even before the snowflake morphology was evident (i.e. in the 2 h sample) there must have been crystallites of α-Fe_2O_3 present.

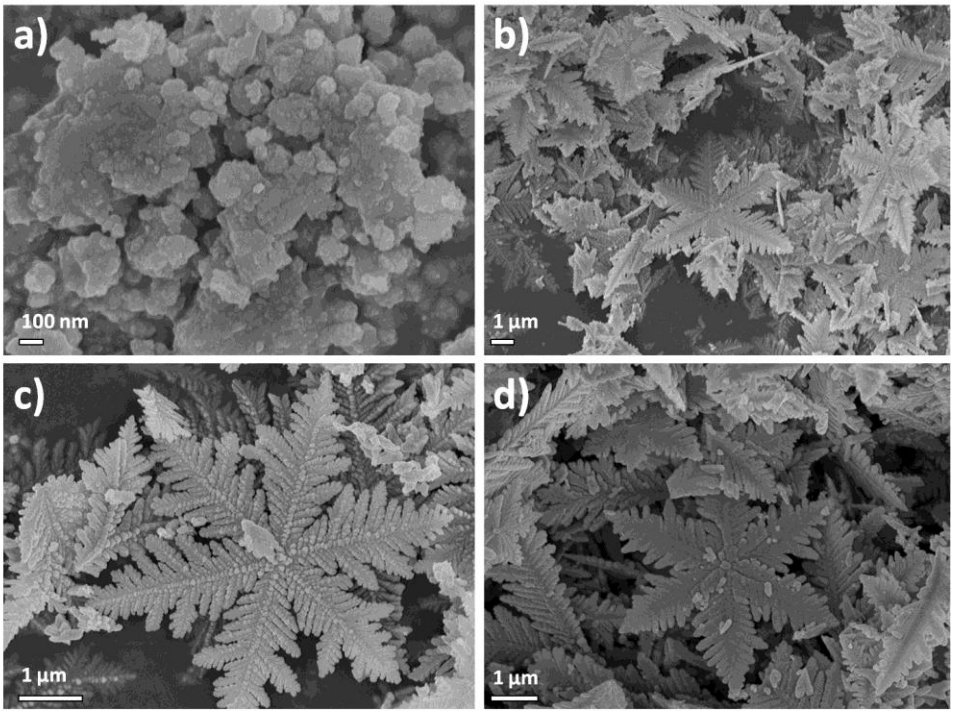

Figure 5.3.1. SEM images showing the typical morphologies of α-Fe_2O_3 particles after different growth times of a) 2 h, b) 3 h, c) 6 h and d) 72 h.

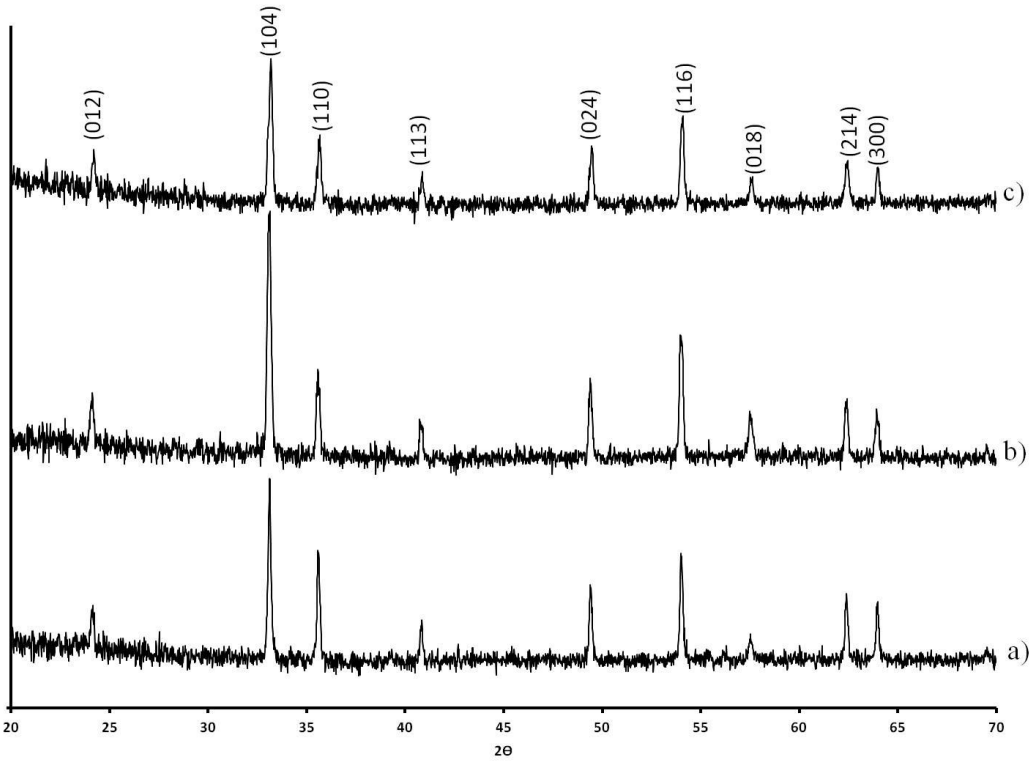

Figure 5.3.2. PXRD patterns indexed to α-Fe_2O_3 phase of samples taken from a range of growth times a) 2 h, b) 3 h and c) 72 h

To determine whether this was indeed the case and to try to discern more about the change in morphology during the earliest growth periods, the 2 h and 3 h samples were studied more closely via TEM and EDX analysis (Figure 5.3.3). HRTEM images of the earliest stage, 2 h, sample show that the aggregates are mostly amorphous with many very small crystallites (approximately 2 - 5 nm in diameter) embedded within them. These nanocrystallites could be indexed to α-Fe_2O_3. The d-spacing labelled A in Figure 5.3.3a measured 1.59 Å, which corresponds to the (122) hematite plane. The development of these nanocrystallites in the amorphous material suggests that the nucleation of α-Fe_2O_3 must take place inside or on the surface of the amorphous aggregates rather than in the aqueous solution. This hypothesis is further supported by the very low dissociation constant of $[Fe(CN)_6]^{3-}$ in water (K_d = 1.0 x 10^{-42}), which would result in there being almost no Fe^{3+} free cations in the solution.

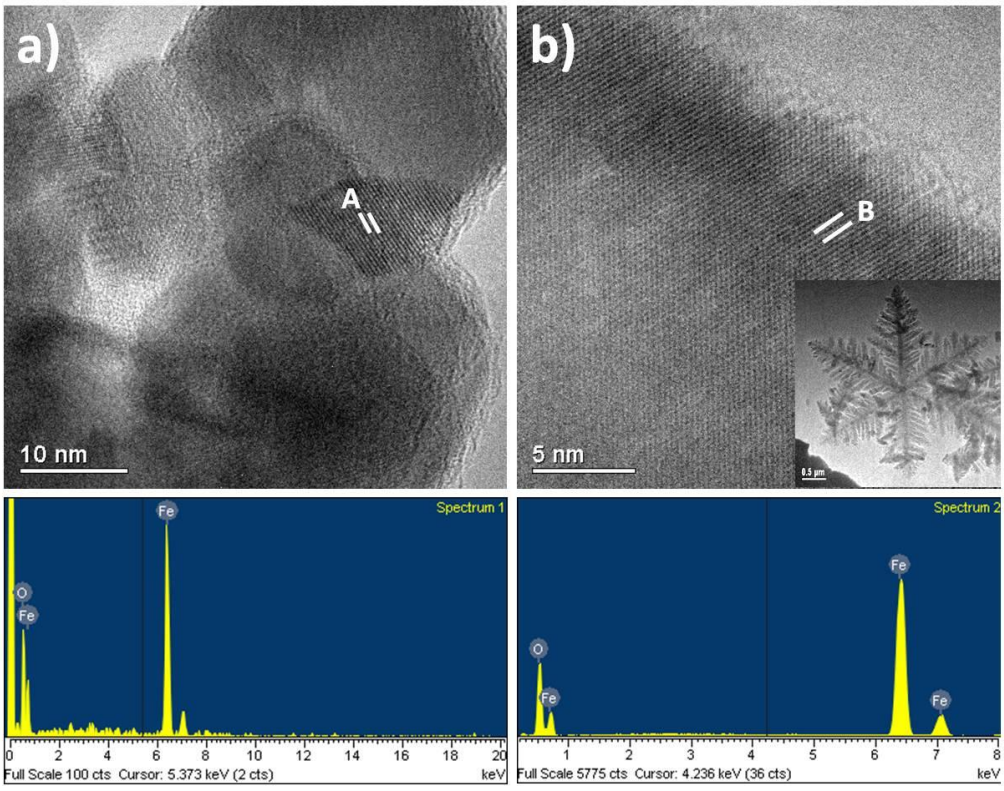

Figure 5.3.3. HRTEM images of samples grown over a) 2 h and b) 3 h. The respective EDX patterns are displayed beneath each micrograph and the inset in b) shows the corresponding low resolution TEM image of the snowflake-like crystal. The d-spacings marked A and B measure 1.59 Å and 2.52 Å respectively. A corresponds to the (122) plane and B to the (110) plane of trigonal α-Fe_2O_3. The HRTEM images were recorded by Chang-Yang Chiang.

Due to the simplicity of the synthetic solution, which only contains distilled water with K^+ and $[Fe(CN)_6]^{3-}$ ions, it can be assumed that the amorphous content at the 2 h growth stage must be polymerised $[Fe(CN)_6]^{3-}$ after partial hydrolysis. For example, the polymerised ions could exist in the form of dimers, $[Fe(CN)_5]^{2-}$–O–$[Fe(CN)_5]^{2-}$, or polymers, {–O–$[Fe(CN)_4]^{2-}$}$_n$. However, as the EDX analysis of this sample only revealed the presence of Fe and O, further analysis, such as TGA, would have to be conducted to fully characterise the amorphous material.

HRTEM analysis of the 3 h sample revealed that the snowflake branches were single crystalline with EDX again showing the presence of Fe and O. The d-spacing labelled B in Figure 5.3.3b measures 2.52 Å and corresponds to the (110) plane of α-Fe_2O_3. The growth direction has been shown to occur along the <11$\bar{2}$0> zone axes (51).

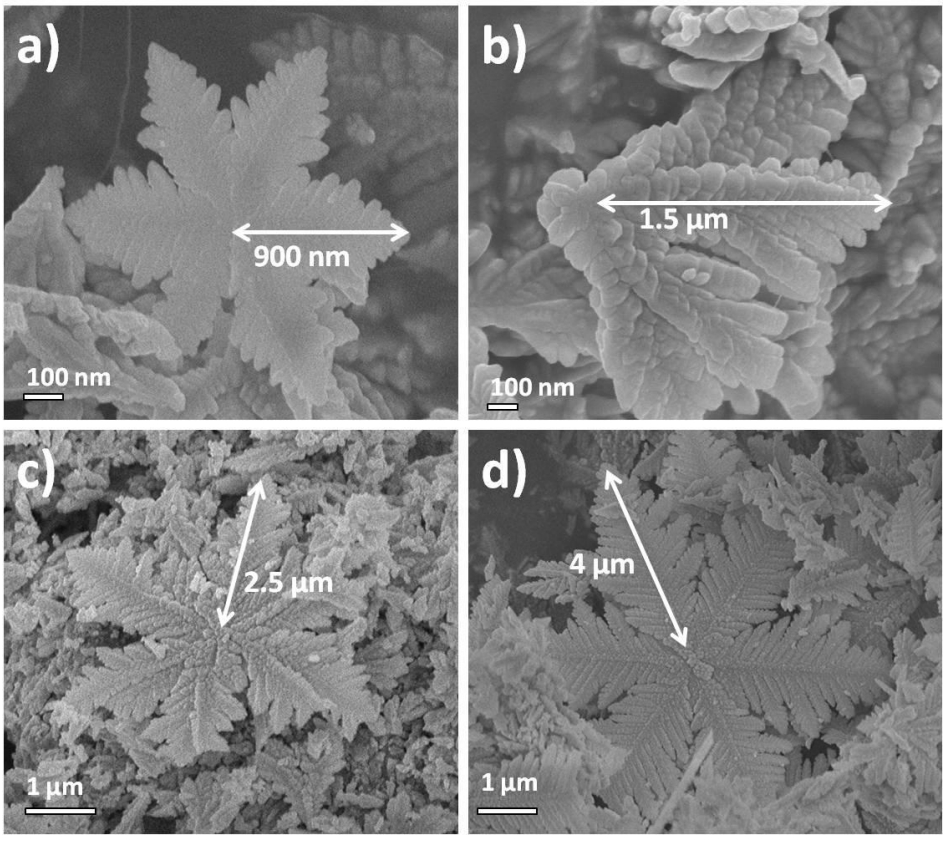

Figure 5.3.4. SEM images showing the typical morphologies and approximate branch lengths of the snowflake-like particles observed at growth times of a) 2 h 10 min, b) 2 h 20 min, c) 2 h 30 min and d) 2 h 40 min.

To further investigate the transition to the snowflake morphology, more samples were synthesised within the 2 h to 3 h time range. SEM analysis revealed a very fast increase in branch length, outwards from the snowflake centre, from approximately 900 nm to an average of 4 μm within just 30 min (Figure 5.3.4). At 2 h 10 min it was possible to find some crystals displaying the snowflake morphology but there remained many of the amorphous aggregates as well. The ratio of snowflakes to aggregates increased over time until the 3 h sample where only snowflake-like particles could be observed (Figure 5.3.1b).

The rapidity of the growth along the six-fold axes implies a highly favoured deposition of precursor ions on the $\{11\bar{2}0\}$ faces of the central seed crystals (i.e. the nanocrystallites embedded in amorphous material in the 2 h sample as displayed in the HRTEM image in Figure 5.3.3a). Since the principal precursor ions in the aqueous solution are $[Fe(CN)_6]^{3-}$, i.e. ferricyanide anions, which contain six lone pairs of electrons from the N atoms on their outer surfaces, they are able to bond with a crystal plane if it has some exposed positive charge or Lewis acid sites. This leads to the interesting possibility that the $\{11\bar{2}0\}$ crystal surfaces may have some such positive charge, which is counter-intuitive given that, under hydrothermal synthetic conditions, metal oxide crystal surfaces would normally be terminated with negatively charged hydroxyl (OH^-) groups.

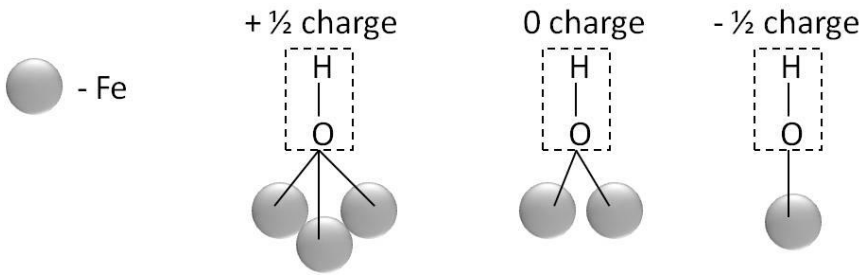

Figure 5.3.5. Illustration showing the charges of hydroxyl groups when they are triply, doubly or singly coordinated with Fe ions from the α-Fe_2O_3 crystal surface.

As discussed in the case of cuprous oxide in Chapter 4, previous reports have already shown in depth analyses of the terminal facets along the principal axes of hematite (i.e. the $\{10\bar{1}0\}$, $\{0001\}$, and $\{11\bar{2}0\}$ planes) as well as calculations of their electronic structures (52-54), revealing that the charge on the terminating OH^- groups is dependent on the specific electronic structure of the related crystal plane, i.e. the number of Fe ions that the OH^- group

is coordinated to. Each Fe ion donates a charge of +½ to the OH^- group so if, for example, a hydroxyl group is doubly coordinated (connected to two Fe ions) then the overall charge is neutral, or OH^0. If a hydroxyl group was singly coordinated, however, the overall charge would become negative ($OH^{0.5-}$) and, conversely, if the hydroxyl group was triply coordinated then the overall charge would become positive ($OH^{0.5+}$). This is illustrated in Figure 5.3.5.

The {0001} surfaces of α-Fe_2O_3 crystals have been found to consist only of neutral, doubly coordinated, terminating hydroxyl groups and the $\{10\bar{1}0\}$ surfaces have a mixture of both singly and doubly coordinated hydroxyl groups, resulting in an overall negative charge (51). Since the $[Fe(CN)_6]^{3-}$ ions are only able to bond with positive sites, it is clear that neither the neutral {0001} or the negative $\{10\bar{1}0\}$ surfaces would be suitable. The $\{11\bar{2}0\}$ surfaces, however, contain all three kinds of hydroxyl groups (singly, doubly and triply coordinated) in equal ratio to each other. This means that, although the overall charge of the surface is neutral, the positively charged, triply coordinated $OH^{0.5+}$ groups can act as Lewis acid sites, providing an opportunity for the lone electron pairs on the $[Fe(CN)_6]^{3-}$ precursor ions to bond.

Change of morphology with pH and $K_3Fe(CN)_6$ concentration

The effect of altering the pH of the synthetic solution on the morphology of the hematite crystals was then briefly studied. Octylamine was added to the solutions before they were incubated and the pH was recorded (the pH of solution before amine addition was 7). The incubation period was kept constant at 6 h for each of the different pH values.

It is evident from the SEM images displayed in Figure 5.3.6 that altering the pH had a notable affect on the morphology of the final products. At pH 9 (Figure 5.3.6a), no distinct branches could be observed on the crystals although they typically displayed a hexagonal shape with a starfish-like morphology. As the pH was increased to 12 (Figure 5.3.6b), the branches became more distinct although the crystals were still much smaller than those observed at a neutral pH since the average branch length was now approximately just 400 nm compared to the 4 μm branches typically observed at pH 7 (Figure 5.3.1 and 5.3.4d). The morphology became particularly interesting when the pH was increased to 13 (Figure 5.3.6c)

as the branches could now be seen to grow in multiple directions, making the crystals more three dimensional.

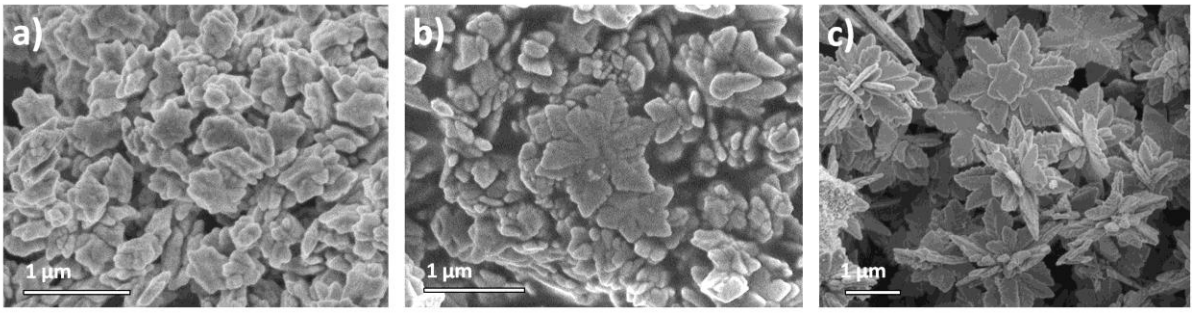

Figure 5.3.6. SEM images displaying the typical morphologies observed when octylamine was added to the synthetic solution to produce different pH values of a) pH 9, b) pH 12 and c) pH 13.

The change in morphology could be due to the increased concentration of OH^- ions in the solution at higher pH values and the formation of a Stern layer (55), which would reduce the electrostatic specificity of the different faces, decreasing the preferential adsorption to the $\{11\bar{2}0\}$ faces. It has been observed in the literature that a Stern layer can form from hydroxyl and CN^- anions over α-Fe_2O_3 surfaces in aqueous solution (53, 54). This would explain why the branches were much smaller and less distinct at higher pH values as the Stern layer could slow the preferential deposition of $[Fe(CN)_6]^{3-}$ ions on the $\{11\bar{2}0\}$ faces, suppressing growth in this direction. Another possibility is that since octylamine is a much stronger alkaline compound when compared to ferricyanide ions (pK_b = 3.35 compared to pK_b = 4.86 respectively) (56), it can bond directly with the $OH^{0.5+}$ groups that are present on the $\{11\bar{2}0\}$ α-Fe_2O_3 surfaces, effectively blocking rapid deposition of $[Fe(CN)_6]^{3-}$ anions on these surfaces.

The increase in the thickness of branches at alkaline pH values and the transition to a three dimensional structure at the highest pH tested also implies an increased growth rate along the $<10\bar{1}0>$ and <0001> zone axes. It is known that the conversion of $[Fe(CN)_6]^{3-}$ to Fe_2O_3 does not happen in one step (see Equation 5.1) but must be achieved via the formation of intermediate ions. At very high pH values, the positive $OH^{0.5+}$ groups may become saturated with hydroxyl groups from the solution and so the $OH^{0.5-}$ sites instead become an

active site for growth by attracting positively charged intermediate cations (e.g. $[Fe(H_2O)_5(CN)]^{2+}$). As a result, the Fe-containing cations would bond with the singly coordinated $OH^{0.5-}$ groups on the <10$\bar{1}$0> and <11$\bar{2}$0> zone axes but, since the {11$\bar{2}$0} surfaces are blocked by octylamine, growth now occurs along the <10$\bar{1}$0> directions, resulting in thicker branches. At pH 13, when the growth occurs along all three of the principal zone axes, it is likely that the effects of the amine have outweighed the standard roles of the charged hydroxyl groups, suppressing favourable growth along any particular direction, resulting in three dimensional crystals.

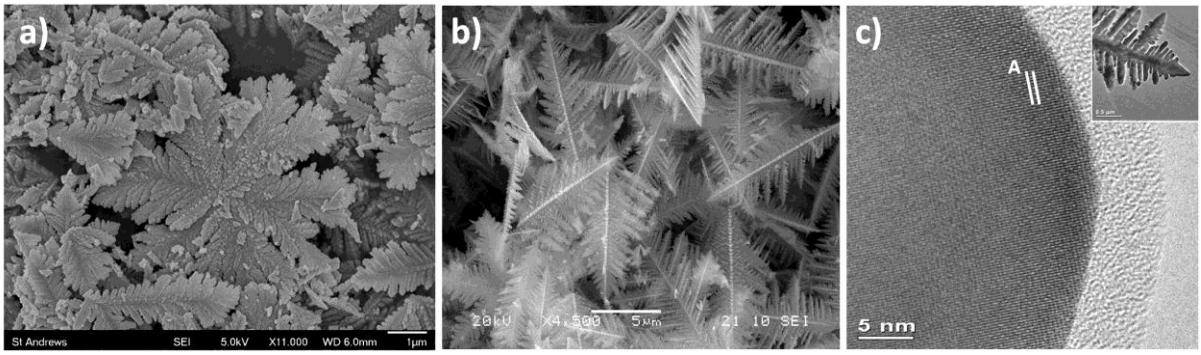

Figure 5.3.7. Images showing the change in morphology in samples grown over 48 h with a $K_3Fe(CN)_6$ concentration of a) 2.0 mM and b) 10 mM. c) HRTEM image of the tip of a branch from the 10 mM sample, with the corresponding low magnification image inset. The d-spacing labelled A measures 2.53 Å and corresponds to the (110) plane of α-Fe_2O_3. The HRTEM image was recorded by Chang-Yang Chiang.

Finally, the change in morphology upon increasing $K_3Fe(CN)_6$ concentration was also briefly analysed. The 48 h synthesis was repeated with an increased $K_3Fe(CN)_6$ concentration of 10 mM (in contrast to 2.0 mM in the original synthesis). SEM analysis revealed a slight change in the appearance of the α-Fe_2O_3 crystals (Figure 5.3.7). At the increased concentration, the branches were thinner and longer, resulting in a feather-like morphology (Figure 5.3.7b). The average branch length was doubled to approximately 8 μm rather than 4 μm when the $K_3Fe(CN)_6$ concentration was 2.0 mM. It is likely that the higher concentration simply causes a faster rate of branch growth as the availability of $[Fe(CN)_6]^{3-}$ ions in the solution will have increased. HRTEM analysis confirmed that the feather-like crystals were single crystalline hematite, with the d-spacing labelled A in Figure 5.3.7c measuring 2.53 Å, which corresponds to the (110) α-Fe_2O_3 plane.

The changes in the morphologies of snowflake-like hematite crystals at a range of $K_3Fe(CN)_6$ concentrations are currently under investigation by other members of the Zhou research group.

Suggested Growth Mechanism

Upon investigation of the crystal structure and morphology of snowflake-like α-Fe_2O_3 crystals over a range of growth times, it is evident that they do not grow via a classical route, nor do they follow the reversed crystal growth mechanism observed for the calcite and RHO-ZIF crystals discussed earlier in this chapter. There is more work to be done into this interesting morphology, but a new growth mechanism can now be proposed based on the data collected thus far (Figure 5.3.8).

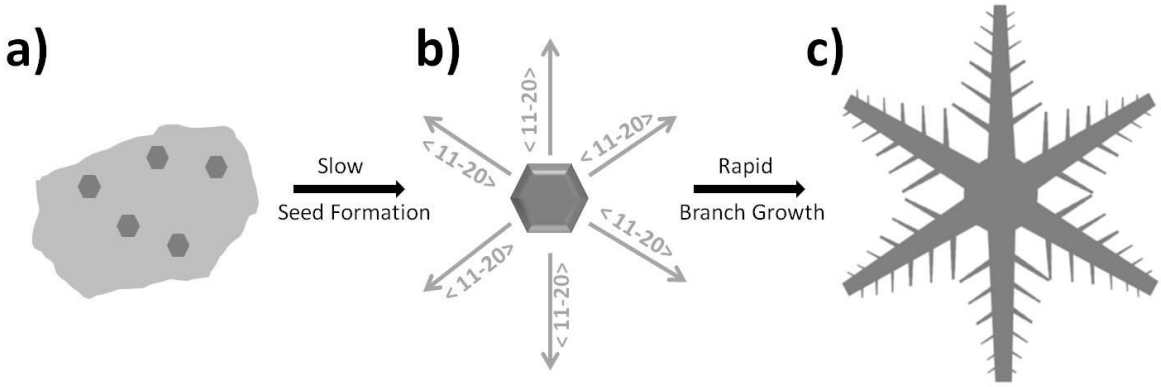

Figure 5.3.8. Schematic showing proposed growth mechanism of α-Fe_2O_3 snowflake-like crystals. a) nanocrystallites of α-Fe_2O_3 (dark grey) grow inside or on the surface of larger amorphous aggregates (light grey) of precursor materials, b) α-Fe_2O_3 seed crystals form from the nanocrystallites followed by c) rapid growth of branches as $[Fe(CN)_6]^{3-}$ ions bond to the exposed $(OH)^{0.5+}$ groups on the $\{11\bar{2}0\}$ surfaces of the α-Fe_2O_3 seed crystals.

In the first stage of growth (up to 2 h), small crystallites of α-Fe_2O_3 form either inside or on the surface of larger amorphous aggregates (between 50 – 500 nm in diameter), which are composed of polymerised precursor ions. As the growth time is increased beyond 2 h, there is rapid deposition of $[Fe(CN)_6]^{3-}$ ions on the $\{11\bar{2}0\}$ surfaces of the α-Fe_2O_3 crystals due to the presence of positively charged hydroxyl groups, $OH^{0.5+}$, on these planes. This

resulted in a fast growth of branches along the <11$\bar{2}$0> zone axes, which quickly increased in length from just 400 nm at 2 h 10 min (Figure 5.3.4a) to 4 μm by 2 h 40 min (Figure 5.3.4d).

In the initial reaction conditions there was no further growth of the branches evident after this although when the concentration of $K_3Fe(CN)_6$ was increased to 10 mM, the branches had doubled in length to 8 μm after 48 h of incubation (Figure 5.3.7b). Therefore, in the initial reaction conditions, when the $K_3Fe(CN)_6$ concentration used was only 2.0 mM it is likely that no further grow occurred after the branches reached 4 μm simply because there were no longer sufficient $[Fe(CN)_6]^{3-}$ ions available.

When octylamine was added to increase the pH of the reaction solution, this rapid growth mechanism was disturbed as the amine negated the effects of the differently charged hydroxyl groups on the different α-Fe_2O_3 surfaces. This resulted in a change from the preferential growth direction being solely along the <11$\bar{2}$0> zone axes to a suppressed growth in these directions. Eventually, when the pH was increased to 13, growth occurred along all of the α-Fe_2O_3 principal planes (i.e. the {10$\bar{1}$0}, {0001}, and {11$\bar{2}$0} planes), giving rise to three dimensional structures.

5.3.4 Conclusions

The results of this work provide further evidence that the classical, "bottom-up", theory of crystal growth which was established more than a century ago, is often not applicable to materials with complex, highly dendritic morphologies and that there is still a lot of work to be done into crystal growth theory as other, non-classical mechanisms such as reversed crystal growth are also not applicable in this case. Even the theories put forward by Curie and Wulff (11) that can help to explain the formation of polyhedral crystal shells (for example, in the case of the RHO-ZIF) cannot be applied to highly symmetrical, highly branched structures such as these snowflake-like crystals. Their theory explained that the equilibrium shape of a free crystal is that which minimizes its surface free energy and so the snowflakes, with their huge surface areas, clearly do not follow this rule.

While the work completed thus far has vastly improved knowledge of the mechanism by which these crystals grow, further research is still being carried out into the formation of snowflake-like α-Fe_2O_3 particles as only by truly understanding their growth will it be

possible to manipulate their morphologies and, therefore, enhance their desirable properties for their many varied applications in industry. This further evidence that charged hydroxyl groups may play a crucial role in the rapid growth of branches in dendritic crystals complements the results of the studies performed into the growth of branched Cu_2O structures as discussed in Chapter 4.

References

1. Xiang, L.; Xiang, Y.; Wen, Y.; Wei, F. *Mater. Lett.*, **2004**, *58*, 959.
2. Manoli, F.; Dalas, E.; *J. Cryst. Growth*, **2000**, *217*, 416.
3. (a) Combes, C.; Tadier, S.; Galliard, H.; Girod-Fullana, S.; Charvillat, C.; Rey, C.; Auzely-Velty, R.; El Kissi, N. *Acta Biomater.*, **2010**, *6*, 920. (b) Vucak, M.; Pons, M. N.; Peric, J.; Vivier, H. *Powder Technol.*, **1998**, *97*, 1. (c) Jada, A.; Pefferkorn, E. J. *Mater. Sci. Lett.*, **2000**, 19, 2077.
4. Xie, A.-J.; Shen, Y.-H.; Zhang, C.-Y.; Yuan, Z.-W.; Zhu, X.-M.; Yang, Y.-M. *J. Cryst. Growth*, **2005**, *285*, 436.
5. Kırboga, S.; Öner, M. *Colloids Surf. B*, **2012**, *91*, 18.
6. Sander, J. R. G.; Bučar D.-K.; Baltrusaitis, J.; MacGillivray, L.R. *J. Am. Chem. Soc.*, **2012**, *134*, 6900.
7. Shen, J.-W.; Li, C. L.; van der Vegt, N. F. A.; Peter, C. *J. Phys. Chem. C*, **2013**, *117*, 6904.
8. De Leeuw, N. H.; Parker, S. C. *J. Phys. Chem. B*, **1998**, *102*, 2914.
9. (a) Bravais, A. *Études Crystallographiques. Paris: Gauthier-Villars*, **1866**. (b) Friedel, M. G. *Bull. Soc. Fr. Mineral Cristallogr.*, **1907**, *30*, 326. (c) Donnay, J. D. H.; Harker, D. *Am. Mineral*, **1937**, *22*, 446.
10. Hartman, P.; Perdok, W. G. *Acta Cryst.*, **1955**, *8*, 521.
11. (a) Curie, P. *Bull. Soc. Fr. Mineral Cristallogr*, **1885**, *8*, 145. (b) Wulff, G. Z. *Kristallogr*, **1901**, *34*, 449.
12. Chen, X. Y.; Qiao, M. H.; Xie, S. H.; Fan, K. N.; Zhou, W. Z; He, H. Y. *J. Am. Chem. Soc.*, **2007**, *129*, 13305.
13. Zhou, W. Z. *Adv. Mater.*, **2010**, *22*, 3086.
14. Greer, H.; Wheatley, P. S.; Ashbrook, S. E.; Morris, R. E.; Zhou, W. Z. *J. Am. Chem. Soc.*, **2009**, *131*, 17986.

15. Yao, J. F.; Li, D.; Zhang, X. Y.; Kong, C. H.; Yue, W. B.; Zhou, W. Z.; Wang, H. T. *Angew. Chem. Int. Ed*., **2008**, *47*, 8397.
16. Self, K.; Zhou, H.; Greer, H. F.; Tian, Z. R.; Zhou, W. Z. *Chem. Commun.*, **2013**, *49*, 5411.
17. Yaghi, O. M.; O'Keeffe, M.; Ockwig, N. W.; Chae, H. K.; Eddaoudi, M.; Kim, J. *Nature*, **2003**, *423*, 705. (b) Kitagawa, S.; Kitaura, R.; Noro, S. *Angew. Chem., Int. Ed.*, **2004**, *43*, 2334. (c) Ferey, G. *Chem. Soc. Rev.*, **2008**, *37*, 191. (d) Aakeroy, C. B.; Champness, N. R.; Janiak, C. *CrystEngComm*, **2010**, *12*, 22.
18. Eddaoudi, M.; Kim, J.; Rosi, N.; Vodak, D.; Wachter, J.; O'Keeffe, M.; Yaghi, O. M. *Science*, **2002**, *295*, 469.
19. Farrusseng, D.; Aguado, S.; Pinel, C. *Angew. Chem., Int. Ed.*, **2009**, *48*, 7502.
20. Takashima, Y.; Martinez, V. M.; Furukawa, S.; Kondo, M.; Shimomura, S.; Uehara, H.; Nakahama, M.; Sugimoto, K.; Kitagawa, S. *Nat. Commun.*, **2011**, *2*, 168.
21. Horcejada, P.; Serre, C.; Maurin, G.; Ramsahye, N. A.; Balas, F.; Vallet-Regi, M.; Sebban, M.; Taulelle, F.; Ferey, G. *J. Am. Chem. Soc.*, **2008**, *130*, 6774.
22. (a) Turner, S.; Lebedev, O. I.; Schroder, F.; Esken, D. E.; Fischer, R. A.; Tendeloo, G. V. *Chem. Mater.*, **2008**, *20*, 5622. (b) Houk, R. J. T.; Jacobs, B. W.; Gabaly, F. E.; Chang, N. N.; Talin, A. A.; Graham, D. D.; House, S. D.; Robertson, I. M.; Allendorf, M. D. *Nano. Lett.*, **2009**, *9*, 3413. (c) Müller, M.; Lebedev, O. I.; Fischer, R. A. *J. Mater. Chem.*, **2008**, *18*, 5274. (d) Proch, S.; Herrmannsdorfer, J.; Kempe, R.; Kern, C.; Jess, A.; Seyfarth, L.; Senker, J. *Chem. Eur. J*, **2008**, *14*, 8204. (e) Jiang, H.; Liu, B.; Akita, T.; Haruta, M.; Sakurai, H.; Xu, Q. *J. Am. Chem. Soc.*, **2009**, *131*, 11302.
23. Huang, X. C.; Lin, Y. Y.; Zhang, J. P.; Chen, X. M.; *Angew. Chem., Int. Ed.*, **2006**, *45*, 1557. (b) Park, K. S.; Ni, Z.; Côté, A. P.; Choi, J. Y.; Huang, R.; Uribe-Romo, F. J.; Chae, H. K.; O'Keeffe, M.; Yaghi, O. M. *Proc. Natl. Acad. Sci. U. S. A.*, **2006**, *103*, 10186. (c) Zhang, J. P.; Zhang, Y. B.; Lin, J. B.; Chen X. M. *Chem. Rev.*, **2012**, *112*, 1001.
24. Kahr, J.; Mowat, J. P. S.; Slawin, A. M. Z.; Morris, R. E.; Fairen-Jimenez, D.; Wright, P. A. *Chem. Commun.*, **2012**, *48*, 6690.
25. Pimentel, B. R.; Parulkar, A.; Zhou, E. K.; Brunelli, N. A.; Lively, R. P. *ChemSusChem*, **2014**, *7*, 3202.
26. Hayashi, A.; Côté, A. P.; Furukawa, H.; O'Keeffe, M.; Yaghi, O. M. *Nat. Mater.*, **2007**, *6*, 501.
27. Blatov, V. A.; Ilyushin, G. D.; Proserpio, D. M. *Chem. Mater.*, **2013**, *25*, 412.

28. Schierz, P.; Fritzsche, S.; Janke, W.; Hannongbua, S.; Saengsawang, O.; Chmelik, C.; Kärger, J. *Micropor. Mesopor. Mat.*, **2015**, *203*, 132.
29. Ostwald, W. *Lehrbruck der Allgemeinen Chemie*, **1896**, *2*. (b) Boistelle, R.; Astier, J. P. *J. Cryst. Growth*, **1988**, *90*, 14.
30. Zheng, C. M.; Greer, H. F.; Chiang, C. Y.; Zhou, W. Z. *CrystEngComm*, **2014**, *16*, 1064.
31. Kaye, S. S.; Dailly, A.; Yaghi, O. M.; Long, J. R. *J. Am. Chem. Soc.*, **2007**, *129*, 14176.
32. Greer, H. F.; Yu, F. J.; Zhou, W. Z. *Sci. China Chem.*, **2011**, *54*, 1867.
33. (a) Yang, X. F.; Fu, J. X.; Jin, C. J.; Chen, J. A.; Liang, C. L.; Wu, M. M.; Zhou, W. Z. *J. Am. Chem. Soc*., **2010**, *132*, 14279. (b) Zhan, H. Q.; Yang, X. F.; Wang, C. M.; Chen, J.; Wen, Y. P.; Liang, C. L.; Greer, H. F.; Wu, M. M.; Zhou, W. Z. *Cryst. Growth Des.*, **2012**, *12*, 1247. (c) Moreira, M. L.; Andrés, J.; Mastelaro, V. R.; Varela, J. A.; Longo, E. *CrystEngComm*, **2011**,*13*, 5818.
34. (a) Venna, S. R.; Jasinski, J. B.; Carreon, M. A. *J. Am. Chem. Soc.*, **2010**, *132*, 18030. (b) Cravillon, J.; Münzer, S.; Lohmeier, S.-J.; Feldhoff, A.; Huber, K.; Wiebcke, M. *Chem. Mater.*, **2009**, *21*, 1410.
35. Scherrer, P. *Göttinger Nachrichten Gesell.*, **1918**, *2*, 98.
36. Rowsell, J. L. C.; Yaghi, O. M. *Angew. Chem. Int. Ed.*, **2005**, *44*, 4670.
37. Choi, K. M.; Jeon, H. J.; Kang, J. K.; Yaghi, O. M. *J. Am. Chem. Soc.*, **2011**, *133*, 11920.
38. Greer, H. F.; Zhou, W. Z. *Crystallogr. Rev.*, **2011**, *17*, 163.
39. Murray, L. J.; Dincă, M.; Long, J. R.; *Chem. Soc. Rev.*, **2009**, *38*, 1294.
40. Tarbuck, E. J.; Lutgens, F. K.; Tasa, D. *Earth Science Thirteenth Edition*, Prentice Hall, **2010**.
41. (a) Poulton, S. W.; Krom, M. D.; Rijn, J. V.; Raiswell, R. *Water Res.*, **2002**, *36*, 825. (b) Zhong, L. S.; Hu, J. S.; Liang, H. P.; Cao, A. M.; Song, W. G.; Wan, L. J. *Adv. Mater.*, **2006**, *18*, 2426.
42. Couto, D.; Freitas, M.; Carvalho, F.; Fernandes, E. *Curr. Med. Chem.*, **2015**, *22*, 1808.
43. Jia, F.; Harrison, A.; Jumas, J. C.; Chadiwck, A. V.; Kockelmann, W.; Bruce, P. G. *J. Am. Chem. Soc*. **2006**, *128*, 5468.
44. Zeng, H.; Li, J.; Liu, J. P.; Wang, Z. L.; Sun, S. H. *Nature*, **2002**, *420*, 395.

45. Cao, H.; Wang, G.; Zhang, L.; Liang, Y.; Zhang S.; Zhang, X. *ChemPhysChem*, **2006**, *7*, 1897.
46. Bang, J. H.; Suslick, K. S. *J. Am. Chem. Soc.*, **2007**, *129*, 2242.
47. Lv, B. L.; Liu, Z. Y.; Tian, H.; Xu, Y.; Wu, D.; Sun, Y. H. *Adv. Funct. Mater*., **2010**, *20*, 3987.
48. (a) Cao, M. H.; Liu, T. F.; Gao, S.; Sun, G. B.; Wu, X. L.; Hu, C. W.; Wang, Z. L. *Angew. Chem., Int. Ed.*, **2005**, *44*, 4197. (b) Zhang, X. L.; Sui, C. H.; Gong, J.; Su, Z. M.; Qu, L. Y. *J. Phys. Chem. C*, **2007**, *111*, 9049.
49. Blake, R. L.; Hessevick, R. E.; Zoltai, T.; Finger, L. W. *American Mineralogist*, **1966**, *51*, 123.
50. Liu, Z.; Lv, B. L.; Wu, D.; Zhu, Y.; Sun, Y. H. *CrystEngComm*, **2012**, *14*, 4074.
51. Liu, Z.; Chiang, C.-Y.; Li, W.; Zhou, W. Z. *Chem. Commun.*, **2015**, *51*, 9350.
52. Cornell, R. M.; Schwertman, U. *The Iron Oxides: Stucture, Properties, Reaction, Occurences and Use Second Edition*, Wiley VCH GmbH&Co., **2003**.
53. Rochester, C. H.; Topham, S. A. *J. Chem. Soc., Faraday Trans. 1*, **1979**, *75*, 1073.
54. Barron, V.; Torrent, J. *J. Colloid Interface Sci*., **1996**, *177*, 407.
55. Stern, O. *Z. Electrochem*., **1924**, *30*, 508.
56. Wan, Z.; Luan, W. L.; Tu, S. T. *J. Phys. Chem. C*, **2011**, *115*, 1569.

Chapter 6. General Conclusions and Future Work

6.1 General Conclusions

In conclusion, this research has revealed several non-classical growth mechanisms for materials which are highly desirable for their many industrial applications but which, in many cases, have been assumed to follow the classical "bottom-up" crystal growth route established over a century ago and so have gone unstudied. New growth mechanisms have been proposed for each material after extensive time-based studies of the crystals, using SEM and TEM as the main characterisation techniques. Uncovering the true nature of how these highly useful materials form is important as only by truly understanding their growth can we exhibit fine control over their morphology and properties and, therefore, maximise their effectiveness for their many applications.

In some instances, it was the presence of an organic agent within the reactive solution that disturbed the environment for classical nucleation and free growth. Instead, the aggregation of precursor ions was enhanced, leading to the formation of disordered particles, typically consisting of many nanocrystallites embedded in an organic matrix. These particles would then undergo a recrystallization process, eventually leading to single crystals. In the case of the decorated ZnO microstadiums, a hydrothermal method was reported where many nanocones of ZnO could be grown on the inner and outer columnar surfaces of ZnO microstadium walls. It had previously been unclear why the additional growth occurred in this way as it would be more energetically favourable to simply extend the existing crystal structure (through classical growth) rather than to form the cones or branches on the surface. Through studying the nanocone growth after just 10 min of hydrothermal treatment time it was revealed that the organic component used in the synthetic solution, 1,3-propanediamine, had enhanced the aggregation of precursor ions on the microstadium surfaces as they were attracted by the lone electron pairs on the O and N atoms on the amine molecules. These aggregates then recrystallised to form many well aligned, sharp-tipped ZnO nanorods.

In the case of the rhombohedral calcite particles it was also found that the organic polymer, chitosan, used in the synthesis played a key role in causing the $CaCO_3$ crystals to grow via a non-classical route. The polar $–NH_2$ and –OH groups on the chitosan molecules

attracted the polar precursor ions leading to aggregation within larger organic clusters. These aggregates then underwent surface recrystallization, forming small islands of single crystal on the aggregate surface that grew larger over time, eventually joining together so that the entire surface was covered in a thin layer of single crystal. When the growth period was extended to a longer time of 9 days, the crystallisation had extended inwards, towards the core, leaving true single crystals. The calcite crystals were, therefore, found to be a new example of a material growing via the reversed crystal growth route.

Further new evidence of this non-classical growth mechanism was discovered upon studying the formation of RHO-ZIF crystals, which have a rhombic dodecahedral morphology with 12 exposed {110} facets. Again, in this case it was the aggregation of precursor material that dominated in the earliest growth stage and so caused a deviation from classical growth. The aggregates underwent surface recrystallization and then the crystallisation was observed to grow thicker, inwards, to the core until true single crystals were formed after 6 weeks. As a result of this work, a much clearer understanding has been achieved of how and why the RHO-ZIF crystals form and so it was possible to obtain N_2 adsorption data that was much closer to the theoretically possible maximum N_2 uptake value of 10 mmol g^{-1}, which previous research groups had been unable to achieve.

The research performed into the snowflake-like hematite, α-Fe_2O_3, crystals with six-fold symmetry has complemented the results from the Cu_2O experiments in that it has demonstrated a very different cause for the deviation from classical growth as there was no organic present in the synthesis to enhance the aggregation of precursor ions. In these cases, it was actually the electronic configuration of the different principal terminating facets of the metal oxide seed crystals that played a crucial role in the rapid growth of branches. In the case of Cu_2O, the terminating {111} surfaces were the only ones that were covered with singly coordinated OH groups. The charge of an OH group on a metal oxide surface is highly dependent on the number of metal cations it is coordinated to. In the Cu_2O case, the OH groups on the {111} surfaces were the only ones to be negatively charged, making these surfaces the only ones able to attract the positively charged $[Cu/PVP]^{2+}$ precursor material, resulting in the rapid growth of eight branches along the <111> zone axes. After this initial rapid growth, the more classical drive to minimise the surface free energy became the prominent growth process as the Cu_2O nanocrystallites within the disordered branches grew larger, joined together and moved towards a cubic shape, reflecting the cubic unit cell. In the α-Fe_2O_3 case, the branches formed along the $<11\bar{2}0>$ zone axes as the $\{11\bar{2}0\}$ surfaces were

the only ones to be covered with positively charged OH groups coordinated to three metal cations. This resulted in a strong attraction between the $\{11\bar{2}0\}$ facets and the negatively charged $[Fe(CN)_6]^{3-}$ ions in the solution, causing the rapid growth of branches on these surfaces.

This surface absorption enhanced growth is an entirely new concept within crystal growth theories and, through further research, may prove to be the true mechanism for the growth of many highly dendritic crystals that are poorly understood and have often gone unstudied.

6.2 Future Work

There are several aspects of the work presented in this thesis that could be further investigated. For example, it would be particularly interesting to study the properties of the ZnO decorated microstadiums and to test their photocatalytic capabilities. ZnO is a material of particular interest in photocatalysis and so these decorated microstadiums, with their huge surface areas and maximised spatial organisation may be particularly interesting in this area.

Future work could also examine the properties of the copper nanoparticles coated with graphite or graphite oxide which were observed after a 20 day growth period when using the synthetic method to grow 8-branched Cu_2O. Copper/graphite composites have been synthesized in the literature via a wealth of very complicated techniques, but the facile hydrothermal route presented in Chapter 4 may provide an opportunity to produce these interesting materials in a much simpler, less expensive way.

A particular unsolved problem in crystal growth research is determining why many particles can exhibit their final, polyhedral morphology despite being composed of many disordered nanocrystallites. This was observed a few times within the research presented in this thesis. For example, further studies would be needed to fully elucidate the mechanism by which the Cu_2O crystals transition towards their cubic morphology and how the separate, disorganised branches can start to form the corners and edges of the future cubic morphology before they are connected. This is not the first time the existence of polycrystalline particles within a highly symmetric polyhedral morphology has been observed, which cannot be explained by the classical theories of polyhedral formation during crystal growth and is quite

typical to be the case for materials that have been found to grow via a reversed crystal growth process. It was, therefore, also observed in the present work during the reversed crystal growth of rhombohedral calcite and rhombic dodecahedral RHO-ZIF particles before the outer surfaces had become fully crystalline. It may be possible to attribute this phenomenon to an interaction between the nanocrystallites but more experiments and theoretical studies are needed before the nature of this interaction and the complete formation mechanism can be fully understood.

The new evidence demonstrated through this research that shows surface absorption enhanced crystal growth can be the true mechanism for different branched metal oxide structures may be of particular interest for future research into crystal growth. There are many materials with branched or dendritic morphologies that have a huge range of applications due to their high surface areas. If their growth could be truly understood, it may be possible to tailor their morphologies and further enhance their effectiveness for their different applications.